SLAC-R-869
May 2007

Measurement of Branching Fractions and CP-Violating Asymmetries in B0 to K0K0bar and B+ to K0barK+ Decays at the BaBar Experiment

Jedrzej Biesiada

SLAC-R-869

Prepared for the Department of Energy
under contract number DE-AC02-76SF00515

Printed in the United States of America. Available from the National Technical Information Service, U.S. Department of Commerce, 5285 Port Royal Road, Springfield, VA 22161.

Measurement of Branching Fractions and CP-Violating Asymmetries in $B^0 \to K^0\overline{K}^0$ and $B^+ \to \overline{K}^0 K^+$ Decays at the *BABAR* Experiment

Jedrzej Biesiada

A DISSERTATION PRESENTED TO THE FACULTY
OF PRINCETON UNIVERSITY
IN CANDIDACY FOR THE DEGREE
OF DOCTOR OF PHILOSOPHY

RECOMMENDED FOR ACCEPTANCE
BY THE DEPARTMENT OF PHYSICS

September 2007

Abstract

Over the last few years, the B factories have established the Cabbibo-Kobayashi-Maskawa mechanism of CP violation in the Standard Model through the study of the decays of B mesons. The focus of Belle and *BABAR* has now expanded to the search for signatures of new physics beyond the Standard Model, particularly through examination of flavor-changing neutral-current transitions, which proceed through diagrams involving virtual loops. These decays are suppressed in the Standard Model, increasing sensitivity to new-physics effects but decreasing branching fractions. Exploiting large and growing datasets, *BABAR* and Belle have made many measurements in loop decays where a b quark transitions to an s quark, observing hints of possible deviations from Standard Model expectations in CP-violating measurements.

This dissertation describes the first observation at *BABAR* of the $B^0 \to K^0\overline{K}^0$ and $B^+ \to \overline{K}^0 K^+$ decays using about 350 million $\Upsilon(4S) \to B\overline{B}$ events. These processes are dominated by the gluonic $b \to d$ virtual-loop transition, which is further suppressed in the Standard Model and could have different effects from new physical contributions. The observed branching fractions are $\mathcal{B}(B^0 \to K^0\overline{K}^0) = (1.08 \pm 0.28 \pm 0.11) \times 10^{-6}$ and $\mathcal{B}(B^+ \to \overline{K}^0 K^+) = (1.61 \pm 0.44 \pm 0.09) \times 10^{-6}$. The first measurement of time-dependent CP asymmetries in $B^0 \to K^0\overline{K}^0$ is also presented, obtaining $S = -1.28^{+0.80+0.11}_{-0.73-0.16}$ and $C = -0.40 \pm 0.41 \pm 0.06$, while for $B^+ \to \overline{K}^0 K^+$ the measured direct CP asymmetry is $\mathcal{A}(\overline{K}^0 K^+) = 0.10 \pm 0.26 \pm 0.03$. These measurements open a new sector of inquiry for the B factories. The dissertation also describes the related

measurements of the branching fraction $\mathcal{B}(B^+ \to K^0\pi^+) = (23.9 \pm 1.1 \pm 1.0) \times 10^{-6}$ and direct CP asymmetry $\mathcal{A}(K^0\pi^+) = -0.029 \pm 0.039 \pm 0.010$.

Contents

List of Tables

List of Figures

Acknowledgments

This dissertation is the culmination of a long process of education and research that was shaped by many people to whom I owe thanks. My gratitude must begin with my advisor, Professor James Olsen. He has been a primary force guiding me in the process of becoming a professional physicist, particularly in the areas of data analysis and the interpretation and presentation of scientific results. The sentiment likewise extends to Professor A.J. Stewart Smith, who has essentially served the role of a second advisor, especially in hardware production, operations, and management. Jim and Stew have provided me with indispensable opportunities for personal and professional growth and exerted enormous influence on my understanding of the entire chain of the scientific process in experimental particle physics, from basic physical insights to the political, diplomatic, and financial dimensions of scientific collaboration. In simple terms, they taught me how to get things done in the field with accuracy, effectiveness, and awareness of the difference between idea and practical reality. Not surprisingly, their lessons extend to other areas of life.

I am indebted to Changguo Lu, who has taught me most of what I know about detector science and whose patience, knowledge, and expertise could always be trusted. I also thank past and present engineers and technicians at Princeton and EP Labs, William Sands, Richard Fernholz, Alan Nelson, and Stan Chydzik. Their companionship, professional dedication, and opinionated declamations will be missed. I am grateful to Elaine Bridges and Kim Dawidowski of the Princeton HEP group for their enormous help and assistance. I must also thank Professor Yury Kolomensky at UC Berkeley, who was my first mentor in the field and who offered strong motivation and the first in-depth introduction to the methods and practice of the profession. I extend my gratitude as well to previous teachers in my academic life, who are too numerous to name here.

I am cheerfully thankful to the junior members of the *BABAR* group at Princeton,

Nick Danielson, Ben Lau, and Sasha Telnov. Their friendship and help made life and work considerably easier, more fun, and more funny. I feel a similar sentiment for my fellow graduate students in my class: Lewis Hyatt, Glen Nixon, Eric Egleston, Judy Lau, Mike Niemack, Eric Dahl, Robert Wagner, Justin Kinney, Amin Nasr, Janice Hester, and many others. They were an integral part of my academic and social life in the first two years at Princeton.

I also thank all the members of the *BABAR* collaboration who provided insight and professional support and collegiality. In particular, I extend my appreciation to Luca Cavoto, Gigi Cibinetto, and the other Italian members who showed incredible hospitality and help during my stay in Italy for the LST project and later at SLAC.

I could not have achieved this milestone without the support and companionship of my friends and loved ones outside the field. Thank you for your kind fellowship. Most centrally, I thank my parents, whose love and heartfelt support have been too obviously fundamental and all-important in my life to be described here in detail.

Chapter 1

Introduction

The violation of charge-parity (CP) symmetry in the weak interaction has been well established in the Standard Model, the currently most experimentally verified theory explaining the fundamental particles and interactions occurring in Nature. CP is a discrete transformation involving the reversal of spatial coordinates and particle quantum-numbers that transforms a particle into its antimatter partner. In a CP-symmetric universe the laws of physics are invariant under the CP transformation and physical interactions treat matter and antimatter equally. Although violation of the parity symmetry alone was observed in the weak interactions in the 1950's [1], most physicists assumed that the combined CP symmetry was not violated. However, CP violation was observed in the kaon system in 1964 by Cronin *et al.* [2], who detected the decay of the CP-odd K_L^0 meson into the CP-even $\pi^+\pi^-$ final state at the level of 10^{-3}. Subsequently, Andrei Sakharov showed in 1967 that CP violation was one of the three conditions necessary for the emergence of a matter-antimatter asymmetry in the universe from a symmetric initial state created from the Big Bang [3]. More than three decades later, the *BABAR* and Belle experiments discovered CP violation in the decays of B mesons [4].

Although the degree of CP violation currently observed in experiment is consistent with the Standard Model, it is not enough to account for the baryon-antibaryon

asymmetry determined from astronomical observations. Thus, mechanisms other than Standard Model *CP* violation must be responsible for the dominance of matter over antimatter in today's universe. As the *BABAR* experiment has observed *CP* violation in B decays, its experimental program has expanded to the search for physics beyond the Standard Model, particularly in processes that might contain new *CP*-violating transitions. A promising class of these are Flavor Changing Neutral Current (FCNC) processes, which are mediated by amplitudes involving virtual loops that might include contributions from unobserved particles and interactions. These processes include $b \to s$ penguin amplitudes, occurring in decays such as $B^0 \to \phi K^0_S$, which have been observed and studied for signatures of *CP* violation [5]. Although several hints of deviations from Standard Model predictions have been seen in these rare modes, no definitive inconsistencies have been established.

Another class of FCNC processes are the even rarer $b \to d$ penguin-dominated processes, which are further suppressed in the Standard Model. Analyzing hundreds of millions of B decays, the B factories have so far observed the electroweak penguin decay $B \to \rho\gamma$ [6] and detected evidence for the $b \to d\bar{s}sg$ dominated decays $B^+ \to \overline{K}^0 K^+$ and $B^0 \to K^0\overline{K}^0$ [7, 8]. This dissertation describes the first observation of the latter two modes at the *BABAR* experiment, which is also the first observation of modes dominated by the gluonic $b \to d$ penguin transition. The analysis also includes the first measurement of *CP*-violating asymmetries in $B^0 \to K^0\overline{K}^0$. The branching fractions and *CP* asymmetries in this mode provide a sensitive test of the Standard Model description of *CP* violation in a class of decays that only recently became accessible through the growing datasets of the B factories.

In Chapter 2, I describe the electroweak sector of the Standard Model and its description of *CP* violation, as well as the theoretical background on $b \to d$ penguin amplitudes. In Chapter 3, I present an overview of the PEP-II accelerator and the *BABAR* detector, which collected the data on which this work is based. The analyses of $B^0 \to K^0\overline{K}^0$ and $B^+ \to \overline{K}^0 K^+$ decays are presented in Chapters 4 and 5, respectively.

I present my conclusions and outlook on future measurements in Chapter 6.

Chapter 2

CP violation in the Standard Model

2.1 The Electroweak Interaction

The Standard Model (SM) is a theory of fundamental particles and the electromagnetic, weak, and strong interactions that act upon them. Together with the theory of general relativity that describes gravity, the Standard Model provides a description of nature that so far accounts for almost all observed phenomena in fundamental particle physics. The interactions of the Standard Model are described by the $SU(3) \times SU(2) \times U(1)$ Lie symmetry, where the $SU(3)$ subgroup characterizes the strong interaction and $SU(2) \times U(1)$ describe the mixed electromagnetic and weak interactions as formulated in the Glashow-Weinberg-Salam (GWS) model [9].

The $SU(2)$ component in the GWS model is composed of a triplet of vector bosons,

$$\mathbf{W}^{\mu} = \begin{pmatrix} W^{\mu 1} \\ W^{\mu 2} \\ W^{\mu 2} \end{pmatrix}, \tag{2.1}$$

coupling to a set of quantum numbers called weak isospin, while the $U(1)$ component contributes a single B^μ boson coupling to weak hypercharge. The corresponding vertices in the Lagrangian are:

$$-i\left[g_W\overline{\chi}\gamma_\mu(1-\gamma^5)\chi\mathbf{t}\cdot\mathbf{W}^\mu+\frac{g'}{2}\bar{q}_{u,d}\gamma_\mu q_{u,d}B^\mu\right]+\text{ hermitian conjugate,} \tag{2.2}$$

where g_W and g' are the $SU(2)$ and $U(1)$ charges, respectively, γ's are the appropriate gamma matrices, $\mathbf{t}$ is the vector of Pauli spin matrices, and $q_{u,d}$ correspond to the up and down fermion components of the $SU(2)$ flavor doublets χ. The doublets include three generations of quarks

$$\begin{pmatrix} u \\ d \end{pmatrix}\quad\begin{pmatrix} c \\ s \end{pmatrix}\quad\begin{pmatrix} t \\ b \end{pmatrix} \tag{2.3}$$

and three generations of leptons, consisting of a massive lepton and its corresponding neutrino

$$\begin{pmatrix} \nu_e \\ e \end{pmatrix}\quad\begin{pmatrix} \nu_\mu \\ \mu \end{pmatrix}\quad\begin{pmatrix} \nu_\tau \\ \tau \end{pmatrix}. \tag{2.4}$$

The up and down components of each doublet differ by unit electric charge.

As in the $SU(2)$ symmetry of spin-$\frac{1}{2}$ Dirac particles, the first two components of the W-triplet can be rotated and expressed in a more physically transparent basis to produce "raising" and "lowering" operators, corresponding to the charged vector bosons W^+ and W^-. Every fermion doublet is invariant under the $W^\pm$ transformations, which rotate the two components into each other. This charged-current transformation is a vector-minus-axial-vector ($V-A$) interaction, with the Lagrangian becoming

$$\mathcal{L}=g_W\left[\overline{q_u}\gamma^\mu(1-\gamma^5)W^+_\mu q_d+\overline{q_d}\gamma^\mu(1-\gamma^5)W^-_\mu q_u\right]. \tag{2.5}$$

The $1-\gamma^5$ operator acts as a chiral projection operator on the doublets, projecting out

the left-handed component. After some algebra, the vertex reduces to the following

$$\mathcal{L} = g_W \left[\overline{q_u^L} \gamma^\mu W_\mu^+ q_d^L + \overline{q_d^L} \gamma^\mu W_\mu^- q_u^L \right], \tag{2.6}$$

where $q_{u,d}^L$ is the left-handed component of each quark or lepton operator. Thus, the charged-current reduces to a pure vector-like transformation acting exclusively on left-handed spinors (and right-handed anti-spinors, as in this formulation q_d^L annihilates a left-handed spinor or creates a right-handed anti-spinor).

In the GSW theory, the $SU(2) \times U(1)$ symmetry is broken, since the third component of the W triplet and the B boson of the $U(1)$ symmetry mix through the weak mixing angle θ_W into two linear combinations that correspond to the neutral Z^0 boson and the photon, the carriers of the neutral weak current and the electromagnetic interactions, respectively:

$$\begin{aligned} B^\mu &= A^\mu \cos\theta_W - Z^\mu \sin\theta_W \\ W^{3\mu} &= A^\mu \sin\theta_W + Z^\mu \cos\theta_W. \end{aligned} \tag{2.7}$$

The resulting Lagrangian vertices are of the form

$$Q_q \bar{q}^{L,R} \gamma_\mu q^{L,R} A^\mu \tag{2.8}$$

for the electromagnetic interaction, where Q_q is the charge of fermion q; and

$$\left(T^3 - 2\sin^2(\theta_W) Q\right) \bar{q}^{L,R} \gamma_\mu q^{L,R} Z^\mu \tag{2.9}$$

for the neutral current, where T^3 is the third eigenvalue of weak isospin of the $q^{L,R}$ fermion.

The origin of the $SU(2) \times U(1)$ symmetry breaking is the Higgs mechanism [10], which is responsible for the mass of the fermions and the $W^\pm$ and Z^0 bosons in

the Standard Model. (The photon remains massless.) Its description is beyond the scope of this thesis. The search for the still unobserved Higgs boson, which is also postulated by the Higgs mechanism, is one of the main goals of the Large Hadron Collider experiments [11], which will begin operation in 2007.

2.2 The CKM Mechanism of Changing Flavor

The charged-current Lagrangian described in the previous section appears to conserve generation, as the $W^{\pm}$ transformations operate only within a flavor doublet and do not transform one generation into another. However, generation-changing charged-current processes occur in Nature and have been known since the first weak processes were observed. For instance, in the quark sector, s quarks can decay to u quarks, as evidenced by the decay of the lightest strange particles, the K mesons, into pions, which contain only up and down quarks. Similarly, neutrino oscillations result in neutrinos of one flavor transforming into neutrinos of a different flavor. Flavor mixing in the quark sector is described in the Standard Model through the Cabbibo-Kobayashi-Maskawa (CKM) mechanism [12]. Neutrino oscillations proceed through a theoretically analogous mechanism and will not be described here.

The essence of the CKM mechanism is that the weak flavor eigenstates of the Standard Model do not correspond exactly to the mass eigenstates of the Hamiltonian, which governs how physical particles propagate through space. In other words, the physical particles that we regard as "up" or "down" quarks, for instance, are admixtures of different flavors. The mass and flavor eigenstates are related by the CKM matrix:

$$\begin{pmatrix} d' \\ s' \\ b' \end{pmatrix}_{\text{mass}} = \begin{pmatrix} V_{ud} & V_{us} & V_{ub} \\ V_{cd} & V_{cs} & V_{cb} \\ V_{td} & V_{ts} & V_{tb} \end{pmatrix} \begin{pmatrix} d \\ s \\ b \end{pmatrix}. \tag{2.10}$$

In terms of the mass eigenstates, the charged-current Lagrangian becomes:

$$\mathcal{L} = g_W \left[\overline{u_i^L} \gamma^\mu W_\mu^+ V_{ij} d_i^L + \overline{d_i^L} \gamma^\mu W_\mu^- V_{ij}^* u_i^L \right]. \tag{2.11}$$

Thus, flavor-changing charged currents are governed by the magnitudes and phases of the off-diagonal elements of the CKM matrix. The origin of the CKM mechanism is in the Higgs mechanism, and the matrix itself is a product of matrices that diagonalize the mass matrices determined from the couplings of fundamental particles to the Higgs field.

2.3 Discrete Symmetries

In addition to the continuous Lorentz and translation transformations, there are three fundamental discrete transformations in any field theory describing elementary particles: charge conjugation (C), parity reversal (P), and time reversal T. C negates the internal quantum numbers of a wave function, interchanging a particle with its anti-particle. P reverses the spatial coordinates of a vector, $(t, \mathbf{x}) \rightarrow (t, -\mathbf{x})$, which is equivalent to a mirror-inversion followed by a 180° rotation about the axis perpendicular to the plane of the mirror. T reverses the temporal coordinates of a vector, $(t, \mathbf{x}) \rightarrow (-t, \mathbf{x})$.

Any local gauge quantum field theory that is Lorentz-invariant obeys the combined CPT transformation (i.e. its Lagrangian is invariant under this operation). However, the individual transformations do not have to be good symmetries of the theory. Indeed, in the Standard Model the strong and electromagnetic interactions respect the three symmetries individually, but the weak interaction maximally violates parity, as was demonstrated in the previous discussion of the purely left-handed nature of the charged weak current. The combined CP transformation is also violated in the weak interactions of the K and B mesons. The effect can be deduced from the charged-current Lagrangian. As CP transforms a left-handed particle into its right-handed

antiparticle, performing the operation on Eq. 2.11 transforms the first term on the right side into the second term and vice versa, except for the CKM coefficients V_{ij}, which remain unchanged. Thus, if a term of the CKM matrix has an irreducible imaginary part, so that $V_{ij} \neq V_{ij}^*$, then the Lagrangian is not invariant under the CP transformation, and there is CP violation in the weak interaction of the Standard Model.[1] This corresponds to a fundamental difference in how the weak interaction acts on matter versus how it acts on antimatter. Also, under the CPT assumption, CP violation is equivalent to T violation.[2]

Andrei Sakharov demonstrated that CP violation, along with the presence of baryon-number violating processes and departure from thermal equilibrium, is one of the conditions necessary to create a baryon-antibaryon asymmetry from initially symmetric conditions [3]. The Big Bang is thought to have produced equal amounts of matter and antimatter, but as the expanding universe cooled, allowing matter and antimatter to annihilate into radiation, an excess of matter remained and formed the material structures of the present universe. The matter-antimatter asymmetry is observed in astronomical measurements at the level of 10^{-10} [13], indicating the presence of sizeable CP violation in the fundamental interactions of Nature. The relation between the largest cosmological scales and fundamental interactions at the smallest distances provides a compelling motivation for the study of CP violation in high-energy physics.

[1] The imaginary part originates in the complex couplings of the quark flavor eigenstates to the Higgs field through non-diagonal mass matrices that are the ultimate source of CP violation and flavor mixing in the SM. The imaginary part is irreducible only if no two quarks of the same charge have the same mass. It is interesting to note that mass and CP violation originate from the same mechanism in the Standard Model.

[2] The strong-interaction Lagrangian in the Standard Model also contains a P- and CP-violating parameter, the value of which is theoretically unconstrained in the SM but determined to be vanishingly small in measurements of the T-violating neutron electric dipole moment [14]. The correspondingly "fine-tuned" absence of CP violation in the strong interaction is frequently called the "strong CP problem" of the SM [15].

2.4 The CKM matrix and the Unitarity Triangle

The CKM matrix is a 3×3 complex matrix. Thus, mathematically it contains $2N^2 = 18$ real parameters that characterize its structure, where N is the number of columns. By the conservation of probability in the quantum field theory, it is also a unitary matrix, which imposes N real normalization constraints and $N(N-1)/2$ complex orthogonality constraints on its columns (which is equivalent to $N(N-1)$ real constraints, accounting for both the real and imaginary part of each complex constraint equation). This leaves N^2 independent parameters. In addition, $(2N-1)$ complex phases can be removed by redefining unphysical phases in the quark fields of the Lagrangian. Thus, we are left with $(N-1)^2 = 4$ independent parameters. These can be parameterized most readily as three rotation angles and one irreducible complex phase in the following notation:

$$V_{CKM} = \begin{pmatrix} c_{12}c_{13} & s_{12}c_{13} & s_{13}e^{-i\delta} \\ -s_{12}c_{23} - c_{12}s_{23}s_{13}e^{i\delta} & c_{12}c_{23} - s_{12}s_{23}s_{13}e^{i\delta} & s_{23}c_{13} \\ s_{12}s_{23} - c_{12}c_{23}s_{13}e^{i\delta} & -c_{12}s_{23} - s_{12}c_{23}s_{13}e^{i\delta} & c_{23}c_{13} \end{pmatrix}, \tag{2.12}$$

where $c_{ij} = \cos\theta_{ij}$, $s_{ij} = \sin\theta_{ij}$, and δ is the complex phase.

The three angles characterize the mixing between the three generations of quarks and are small as determined from experiment: $s_{12} \approx \lambda \approx 0.22$ (λ is the sine of the Cabibbo angle), $s_{23} \approx \lambda^2 \approx 0.05$, and $s_{13} \approx \lambda^3 \approx 0.01$. Thus, we can expand the CKM elements in λ to make transparent the hierarchy in their magnitudes, resulting in the Wolfenstein parameterization [16], which is the following to third order in λ:

$$V_{CKM} = \begin{pmatrix} 1 - \frac{1}{2}\lambda^2 & \lambda & A\lambda^3(\rho - i\eta) \\ -\lambda & 1 - \frac{1}{2}\lambda^2 & A\lambda^2 \\ A\lambda^3(1 - \rho - i\eta) & -A\lambda^2 & 1 \end{pmatrix} + O(\lambda^4). \tag{2.13}$$

The parameters A,ρ, and η are of order unity, with η parameterizing CP violation in

the Standard Model.

There are six orthogonality equations (not all independent) that can be written as a consequence of the unitarity condition $VV^\dagger = 1$:

$$\sum_i V_{ij} V_{ik}^* = 0. \tag{2.14}$$

Each equation represents a triangle of the same area (proportional to the degree of *CP* violation) in the complex plane, but only two of them have all three sides of similar length in the Standard Model, producing a non-degenerate triangle:

$$V_{ud} V_{ub}^* + V_{cd} V_{cb}^* + V_{td} V_{tb}^* = 0, \tag{2.15}$$

$$V_{ud} V_{td}^* + V_{us} V_{ts}^* + V_{ub} V_{td}^* = 0. \tag{2.16}$$

The first one of these is the one relevant to B-meson phenomenology and with the Wolfenstein parameterization can be represented as a triangle in the complex $(\rho, i\eta)$ plane as shown in Fig. 2.1. This visualization is referred to as the Unitarity Triangle, with the three angles defined as

$$\alpha \equiv arg\left[-\frac{V_{td}V_{tb}^*}{V_{ud}V_{ub}^*}\right],\ \beta \equiv arg\left[-\frac{V_{cd}V_{cb}^*}{V_{td}V_{tb}^*}\right],\ \gamma \equiv arg\left[-\frac{V_{ud}V_{ub}^*}{V_{cd}V_{cb}^*}\right]. \tag{2.17}$$

The measurement of the sides and angles of this triangle in redundant experimental observables constitutes a stringent test of the CKM picture of *CP* violation in the Standard Model.

2.5 *CP* Violation in B Decays

The B meson is a spin-0 bound state of a b quark and a light (u, d, s, c) quark with intrinsic parity of -1 (a pseudoscalar meson). It decays weakly with the relatively long lifetime of approximately 1.5 ps. *CP*-violating effects from the CKM mechanism

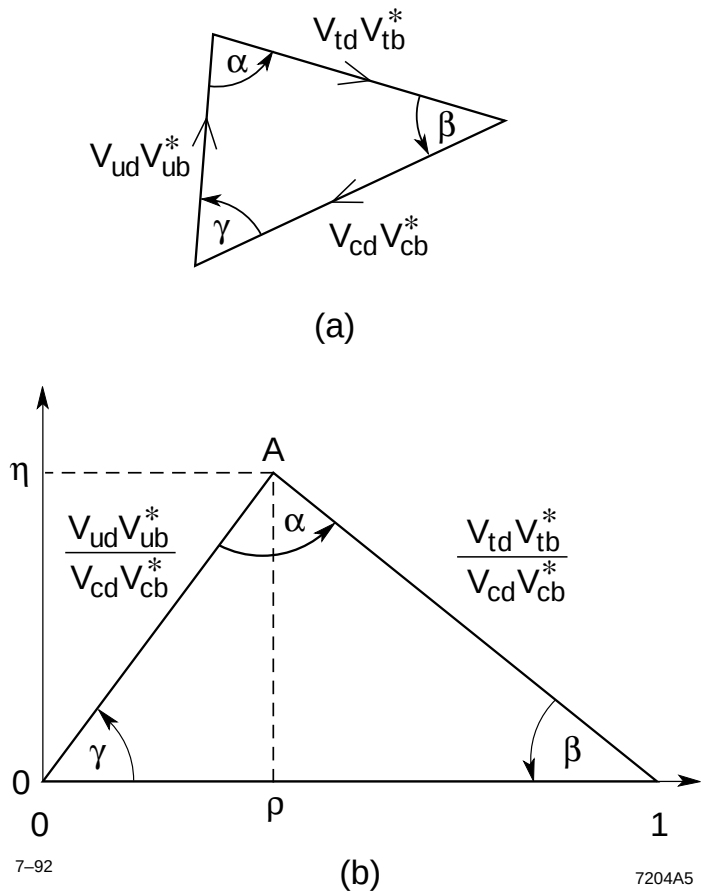

Figure 2.1: The Unitarity Triangle in the B system.

are expected to be large in B decays (unlike in K decays), so B mesons are excellent probes of CP violation [17]. In this thesis, we are concerned only with the first-generation B mesons, where the non-bottom quark is a member of the first generation of quarks. ($B^0 = \overline{b}d$, $\overline{B}^0 = b\overline{d}$, $B^+ = \overline{b}u$, $B^- = b\overline{u}$.)

CP violation can manifest itself in three different ways, the so-called CP violation in decay, in mixing, and in the interference between mixing and decay. CP violation is a result of complex phases in interaction couplings and, as in other areas of physics, these phases can be accessed only through interference effects. Thus, all three types of CP violation involve interference between several amplitudes that lead to the same final state with different phases.

2.5.1 *CP* violation in decay

CP violation in decay, or "direct" *CP* violation, is observed as the difference between the decay rate of a particle to a final state and the decay rate of its antiparticle to the corresponding charge-conjugate final state, usually expressed as a branching-fraction asymmetry,

$$\begin{aligned} A_{CP} &\equiv \frac{\mathcal{B}(\overline{B} \to \overline{f}) - \mathcal{B}(B \to f)}{\mathcal{B}(\overline{B} \to \overline{f}) + \mathcal{B}(B \to f)} \\ &= \frac{|\overline{A}_{\overline{f}}|^2 - |A_f|^2}{|\overline{A}_{\overline{f}}|^2 + |A_f|^2}, \end{aligned} \tag{2.18}$$

where A_f and $\overline{A}_{\overline{f}}$ are the total $B \to f$ and $\overline{B} \to \overline{f}$ decay amplitudes, respectively. A non-zero value of this asymmetry shows a clear difference between the decay of matter and the decay of antimatter through this process.

The asymmetry can be nonzero only if there are two or more interfering processes contributing to the total decay amplitude. Furthermore, these individual contributing amplitudes must have non-equal phases that change sign under *CP* ("weak" phases) and non-equal phases that do not change sign under *CP* ("strong phases"), for only then is their interference sensitive to CP-violating effects. This can be seen if we transparently parameterize the total decay amplitude in terms of the magnitudes a_j, weak phases ϕ_j, and strong phases δ_j of the contributing processes:

$$\begin{aligned} A_f &= \sum_j |a_j| e^{i(\delta_j + \phi_j)}\,, \\ \overline{A}_{\overline{f}} &= \sum_j |a_j| e^{i(\delta_j - \phi_j)}\,. \end{aligned} \tag{2.19}$$

With simple algebra, the numerator of the asymmetry becomes

$$|\overline{A}_{\overline{f}}|^2 - |A_f|^2 = 2 \sum_{i,j} |a_i||a_j| \sin(\phi_i - \phi_j) \sin(\delta_i - \delta_j), \tag{2.20}$$

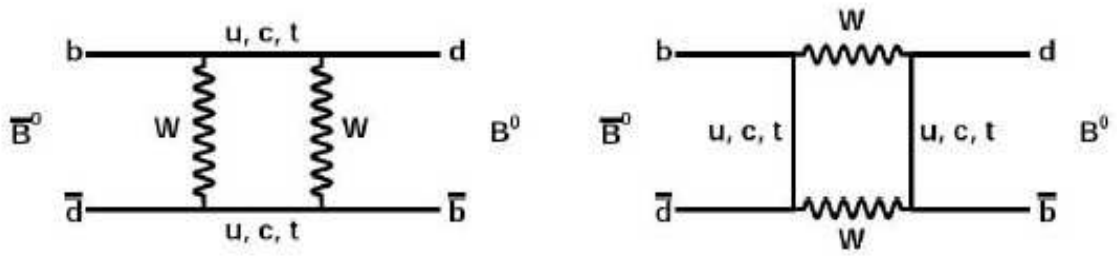

Figure 2.2: The box diagrams mediating $B^0 - \overline{B}^0$ mixing.

which is proportional to the interference between the amplitudes. If the strong and weak phases are not equal, then $|\overline{A}_{\overline{f}}/A_f| \neq 0$, $A_{CP} \neq 0$, and there is direct CP violation in decay mode f.

Up to now, direct CP violation has been observed in the kaon system at the level of a few parts per million [18], and in the $B^0 \to K^+\pi^-$ and $B^0 \to \pi^+\pi^-$ decays at the 10% and 50% levels [19], respectively.

2.5.2 CP violation in mixing

This type of CP violation, otherwise known as "indirect" CP violation, could be present in $B^0 - \overline{B}^0$ oscillations, which proceed through second-order weak processes (Fig. 2.2) as the B mesons propagate through space. In analogy to the CKM mechanism and quark mixing, the neutral B-meson flavor eigenstates and the mass eigenstates of the Hamiltonian are not the same:

$$|B_L\rangle = p|B^0\rangle + q|\overline{B}^0\rangle \tag{2.21}$$
$$|B_H\rangle = p|B^0\rangle - q|\overline{B}^0\rangle,$$

where $|p|^2 + |q|^2 = 1$ and H and L refer to the heavier and lighter mass eigenstates. Any linear combination of the flavor eigenstates

$$a|B^0\rangle + b|\overline{B}^0\rangle \tag{2.22}$$

propagates through space according to the time-dependent Schrödinger equation:

$$i\frac{d}{dt}\begin{pmatrix} a \\ b \end{pmatrix} = \mathbf{H}\begin{pmatrix} a \\ b \end{pmatrix} \equiv \begin{pmatrix} H_{11} & H_{12} \\ H_{21} & B_{22} \end{pmatrix}\begin{pmatrix} a \\ b \end{pmatrix} \equiv \left(\mathbf{M} - \frac{i}{2}\mathbf{\Gamma}\right)\begin{pmatrix} a \\ b \end{pmatrix}, \quad (2.23)$$

where $\mathbf{M}$ and $\mathbf{\Gamma}$ are 2×2 Hermitian matrices corresponding to the mass and decay properties of the B meson. The eigenstates B_H and B_L of $\mathbf{H}$ have mass and width splittings

$$\begin{aligned} \Delta m_d &\equiv M_H - M_L = -2Re(H_{12}H_{21})^{1/2} \\ \Delta\Gamma_d &\equiv \Gamma_H - \Gamma_L = -4Im(H_{12}H_{21})^{1/2}. \end{aligned} \quad (2.24)$$

(The subscript d identifies these quantities with B_d mesons, which contain a down quark, as opposed to B_s mesons, which contain a strange quark and have different splittings.) A state that is created as a B^0 or $\overline{B}^0$ is a mixture of these two mass eigenstates and thus oscillates between the two flavor states as a function of time according to

$$\begin{aligned} |B^0_{\rm phys}\rangle &= e^{-iMt-\Gamma t/2}\left(\cos(\Delta m_d t/2)|B^0\rangle + i\frac{q}{p}\sin(\Delta m_d t/2)|\overline{B}^0\rangle\right), \\ |\overline{B^0}_{\rm phys}\rangle &= e^{-iMt-\Gamma t/2}\left(i\frac{p}{q}\sin(\Delta m_d t/2)|B^0\rangle + \cos(\Delta m_d t/2)|\overline{B}^0\rangle\right), \end{aligned} \quad (2.25)$$

where $M \equiv (M_H + M_L)/2$ and $\Gamma \equiv (\Gamma_H + \Gamma_L)/2$.[3]

The off-diagonal elements of $\mathbf{M}$ determine $B^0 - \overline{B}^0$ mixing through the off-shell diagrams in Fig. 2.2, while the off-diagonal elements of $\mathbf{\Gamma}$ determine mixing through on-shell intermediate states to which both B^0 and $\overline{B}^0$ can decay. *CPT* invariance guarantees that $M_{21} = M_{12}^*$ and $\Gamma_{21} = \Gamma_{12}^*$, so that neither interference among several off-shell mixing amplitudes only, nor interference among several on-shell mixing amplitudes only can produce *CP* violation in mixing. However, in general $H_{21} \neq H_{12}^*$, and

[3]These equations neglect the width splitting, as it is very small in the B_d system: $\Delta\Gamma_d/\Gamma_d = \mathcal{O}(10^{-2})$ and $\Delta\Gamma_d \ll \Delta m_d$, as determined from branching-fraction and mixing measurements [20].

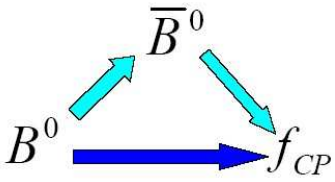

Figure 2.3: The two decay paths to the same final state that can interfere to produce CP violation in interference.

if both M_{12} and Γ_{12} are non-zero and have different phases, so that $Im(M_{12}\Gamma_{12}^*) \neq 0$, then there is CP violation in mixing. (An equivalent condition is $|q/p| \neq 1$, which can be clearly understood in Eq. 2.22 as a difference in how B^0 and $\overline{B}^0$ mesons mix.) As B-meson mixing is completely dominated by off-shell box diagrams, this type of CP violation is negligibly small in the B system, the currently best measurements giving [21]

$$\left|\frac{q}{p}\right| = 1.0015 \pm 0.0039, \tag{2.26}$$

which is consistent with unity.[4]

2.5.3 CP violation in interference between mixing and decay

The final form of CP violation can occur in B^0 and $\overline{B}^0$ decays to the same final state. In this situation, there can be interference between the direct decay of the meson into the final state and the alternate path of first mixing into the anti-meson and then decaying into the final state (Fig. 2.3). As mixing and decay amplitudes are present here, both q/p and $\overline{A}_{\overline{f}}/A_f$ are involved and the relevant quantity is

$$\lambda_f \equiv \eta_{CP}\frac{q}{p}\frac{\overline{A}_{\overline{f}}}{A_f}, \tag{2.27}$$

where η_{CP} is the CP eigenvalue of the final state. Following the previous discussion, one or both of direct CP violation and indirect CP violation is present if $|\lambda_{CP}| \neq 1$

[4] CP violation in mixing is present in the K system, and it was this type that was discovered by Cronin and Fitch.

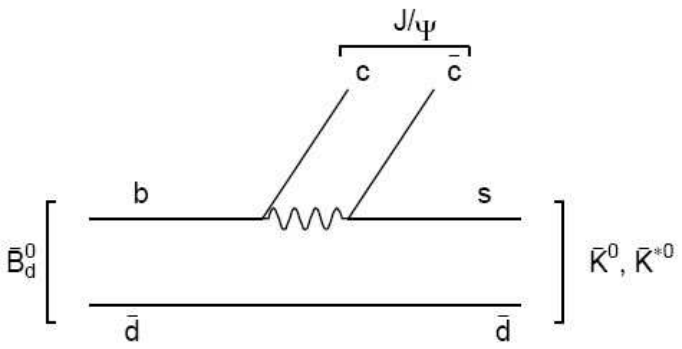

Figure 2.4: The dominant diagram mediating $B^0 \to J/\psi\, K^0$.

(and since *CP* violation in mixing is negligible in B decays, this would signify direct *CP* violation in the B system). However, if $|\lambda_{CP}| = 1$ but $\lambda_{CP} \neq 1$, then $Im(\lambda_{CP}) \neq 0$ and there is *CP* violation in the interference between decays to the final state f with and without mixing. This effect can be observed experimentally only in the difference in the time-dependent decay rates of B^0 and $\overline{B}^0$ mesons:

$$\begin{aligned} A_{CP}(t) &\equiv \frac{\Gamma(\overline{B}^0 \to f)(t) - \Gamma(B^0 \to f)(t)}{\Gamma(\overline{B}^0 \to f)(t) + \Gamma(B^0 \to f)(t)} \\ &= \frac{2Im(\lambda_f)}{1+|\lambda_f|^2}\sin(\Delta m_d t) - \frac{1-|\lambda_f|^2}{1+|\lambda_f|^2}\cos(\Delta m_d t) \\ &= S\sin(\Delta m_d t) - C\cos(\Delta m_d t)\,, \end{aligned} \tag{2.28}$$

where Δm_d, the difference in mass between the heavy and light B-meson eigenstates, is the $B^0 - \overline{B}^0$ mixing frequency. The coefficient S quantifies *CP* violation in decay-mixing interference, while C is a measure of direct *CP* violation. (In fact, the direct *CP* asymmetry $A_{CP} = -C$.) By construction, the two parameters satisfy $S^2 + C^2 \leq 1$, as this constraint is equivalent to the trivial condition $|Im(\lambda_f)| \leq |\lambda_f|$.

The first mode where *CP* violation in such interference was observed was $B^0 \to J/\psi\, K^0_S$ [4]. This mode proceeds primarily through the $b \to c$ tree diagram shown in Fig. 2.4, with a total phase of 2β through interference with the B-mixing diagrams after $K^0 - \overline{K}^0$ mixing in the final state is taken into account. The leading loop ("penguin") diagram has the same phase of 2β. As the decay amplitudes have the

same weak phase, direct *CP* violation is zero in this mode, so that

$$\begin{aligned} S_{J/\psi K^0_S} &= \sin(2\beta), \\ C_{J/\psi K^0_S} &= 0. \end{aligned} \tag{2.29}$$

As this mode is relatively free of hadronic uncertainties and has a clean experimental signature, it provided the first observation of *CP* violation in B decays in the year 2001 [4], with a non-zero observed value of β and thus a non-zero area of the Unitarity Triangle. Since then, the measurement of $\sin(2\beta)$ in this and other charmonium modes has reached the relative precision of 4%, and measurements in different modes are consistent with each other [22].

2.6 *CP* Violation in Penguin Decays and New Physics

Measurements of the angles and sides of the Unitarity triangle through processes dominated by tree-level amplitudes have so far shown that the CKM picture is to first order the correct description of *CP*-violating phenomena in the Standard Model. (The original aim of the B-factory experiments was establishing or excluding this possibility.) This can be seen by the agreement of these measurements in the $(\overline{\rho}, \overline{\eta})$ plane (Fig. 2.5), where

$$\begin{aligned} \overline{\rho} &= \rho(1 - \lambda^2/2), \\ \overline{\eta} &= \eta(1 - \lambda^2/2). \end{aligned}$$

However, the amount of *CP* violation originating from this mechanism is many orders of magnitude too small to account for the observed matter-antimatter asymmetry in the universe. In addition, there are compelling theoretical reasons to suspect that the Standard Model is not the complete description of fundamental interactions, such as the hierarchy problem between the Planck scale of gravitational interactions and

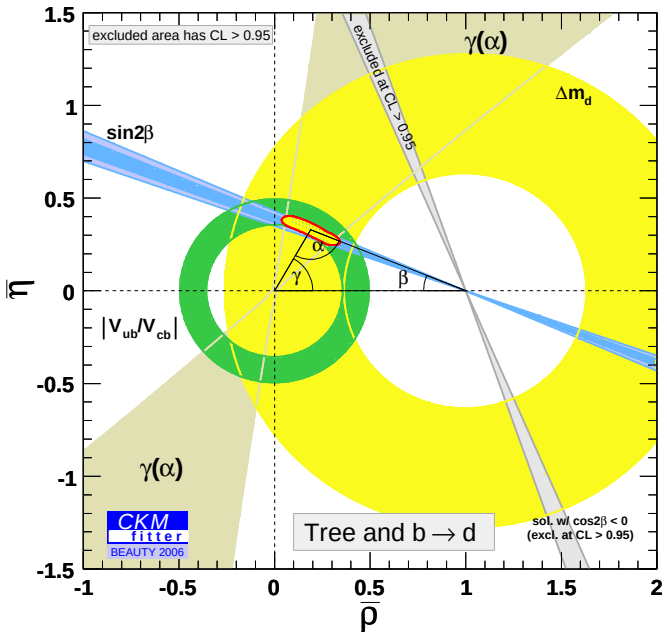

Figure 2.5: UT measurements in tree-level and B_d-mixing processes only [23].

the electroweak symmetry-breaking scale, and the large number of parameters with values unconstrained by theory. Theories such as Supersymmetry and Extra Dimensions that extend the Standard Model and resolve these issues posit new interactions and particles within reach of the next generation of high-energy colliders. Having established the CKM mechanism, the aim of the B factories has extended to the search for signatures of these new phenomena in the form of small deviations from CKM predictions in highly precise measurements of B decays. A particular focus is on finding additional sources of CP violating phases from these effects that might explain the observed cosmological matter-antimatter asymmetry.

As the mass scale of these new particles is predicted to be in the hundreds of GeV/c^2, the absence of sizeable non-SM effects in tree-level B decays is not surprising: the new amplitudes would involve highly off-shell massive bosons that are suppressed relative to the SM weak amplitudes proceeding through W propagators[5]. Thus, a promising area to search for "New-Physics" (NP) signatures is in the so-called

[5]Certain models such as R-parity- and baryon-number violating SUSY allow for new particles of lower mass to enter at tree level.

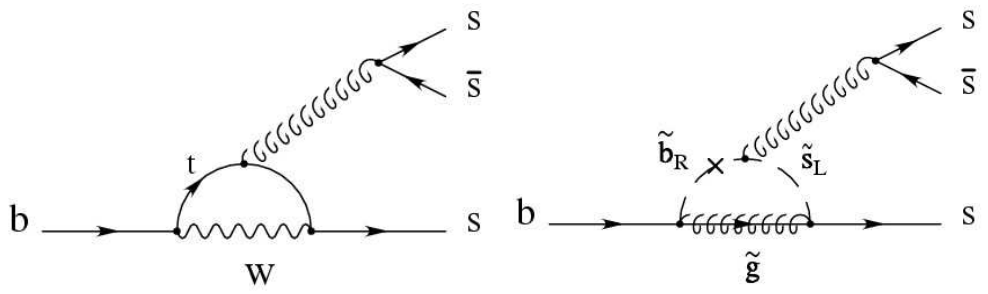

Figure 2.6: The $b \to s$ penguin loop mediated by Standard-Model (left) and New-Physics contributions (right).

"penguin" decays, which are processes where the leading-order amplitudes involve virtual loops. These amplitudes are suppressed in the Standard Model, lowering the SM branching fractions of these modes but allowing effects from potential NP particles to enter at comparable strength due to the virtuality of the loop [24]. Any *CP*-violating structure in these processes that differs from SM predictions would indicate the presence of NP contributions.

One class of these decays are $b \to s$ penguin decays, where the b quark in the B meson transforms to an s quark through a $W-t$ loop as shown in Fig. 2.6.[6] These modes have typical branching fractions of only 10^{-5}, as compared with 10^{-4} -10^{-3} for the charmonium modes. However, time-dependent *CP* asymmetries in many of these modes are sensitive to the UT angle β, and the large datasets collected by the B factories have made possible a rich experimental program of measuring this parameter. ($B^0 \to \phi K^0_S$, Fig. 2.7, was the first such mode to be investigated [5]). The comparison of the value of $\sin(2\beta)$ obtained from charmonium tree-level modes with the analogue obtained from $b \to s$ penguin modes provides a powerful test of the presence of additional *CP*-violating amplitudes in the virtual loops from NP contributions. A tantalizing experimental tension between the two observables has emerged, with the disagreement currently at a significance level greater than two standard deviations (Fig. 2.8). However, more data and theoretical work is needed

[6]These decays are called flavor-changing neutral-current (FCNC) decays, as the involved quark changes flavor but not electric charge, which would not be the case in charged-current weak decays. FCNC processes are forbidden at tree level in the Standard Model.

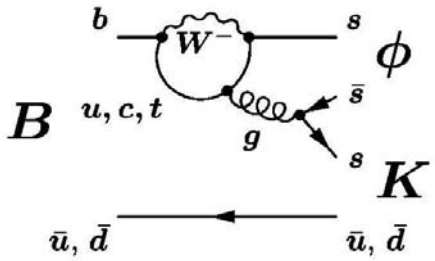

Figure 2.7: $B^0 \to \phi K^0$ decays were the first laboratory for the study of CP violation in $b \to s$ penguin modes.

to make a meaningful comparison with greater statistical confidence.

Similar CP-violating studies have been performed in electroweak $b \to s$ penguin decays, such as $B \to K^*\gamma$ and $B \to K\pi\gamma$, where a real or virtual photon takes the place of the gluon. However, the theoretical interpretation of these measurements vis-à-vis effects of New Physics is not as straightforward as in the case of the gluonic penguin modes. Overall, no significant deviations from SM predictions have been found in $b \to s$ penguin modes, and the CKM mechanism remains experimentally resistant to the effects of potential NP contributions. Figure 2.9 shows the agreement of all UT measurements in the $\overline{\rho}$–$\overline{\eta}$ plane.

Modes dominated by $b \to d$ penguin amplitudes represent the next level of rare-decay tests of the Standard Model, as they are suppressed by an additional CKM factor of $|V_{td}/V_{ts}|^2 \approx 5\%$ relative to $b \to s$ penguin modes. (Their branching fractions are at the 10^{-6} level.) Investigation of modes dominated by these transitions has become possible only recently as the B factories have accumulated hundreds of millions of $B\overline{B}$ pairs. As in the $b \to s$ case, there are electroweak variants of these decays, such as $B \to \rho\gamma$, which was observed recently by *BABAR* and Belle [6] , and gluonic variants, such as $B \to K\overline{K}$, strong evidence for which was observed by both experiments in the year 2004 [7, 8].

Examination of these modes opens a new area of inquiry for the B factories, particularly as NP contributions could produce different effects here than in $b \to s$ penguins. Figure 2.10 shows the space of NP parameter values that are still allowed

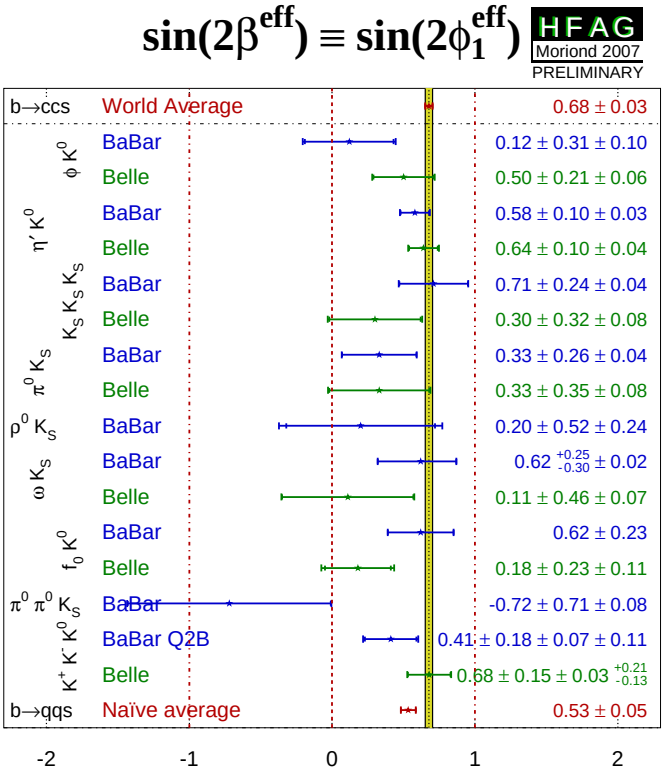

Figure 2.8: Measurements of $\sin(2\beta_{\rm eff})$ in $b \to s$ penguin decays compared with the value measured in charmonium modes (yellow vertical band) [21].

by experiment in the two cases, parameterized in terms of Supersymmetric mass insertions δ_{ij} that govern the mixing between the ith and jth generations in a particular SUSY framework [25]. Furthermore, $B \to K\overline{K}$ decays are the last class of two-body B decays without charm quarks in the final state to be investigated at the B factories: $B \to K\pi$ and $B \to \pi\pi$ decays have been studied extensively, with important results constraining the UT angle α in the latter, and large direct CP-violating effects observed in the former [19].

This thesis describes the observation at *BABAR* of the decays $B^0 \to K^0\overline{K}^0$ and $B^+ \to \overline{K}^0 K^+$, which are dominated by the gluonic $b \to d$ penguin transition shown in Fig. 2.11. It also describes the first measurement of time-dependent CP-violating asymmetries in the former mode, which is the first measurement of this type in a

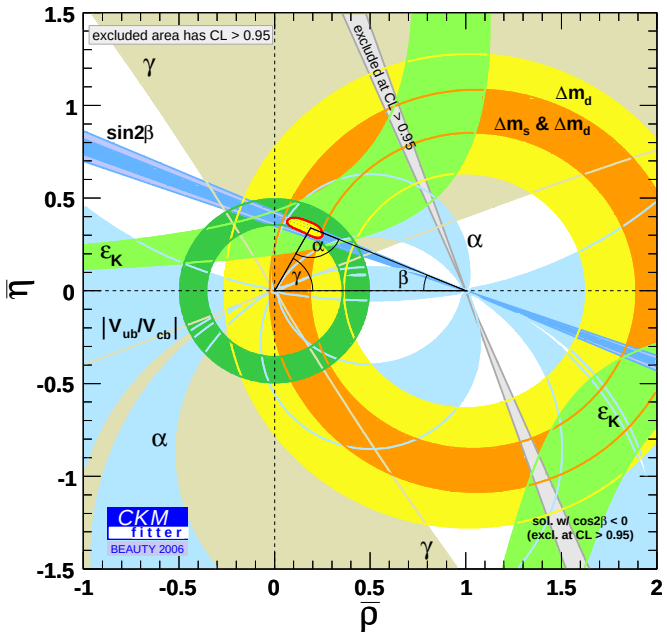

Figure 2.9: All experimental results of UT measurements shown in the $\overline{\rho}$–$\overline{\eta}$ plane [23].

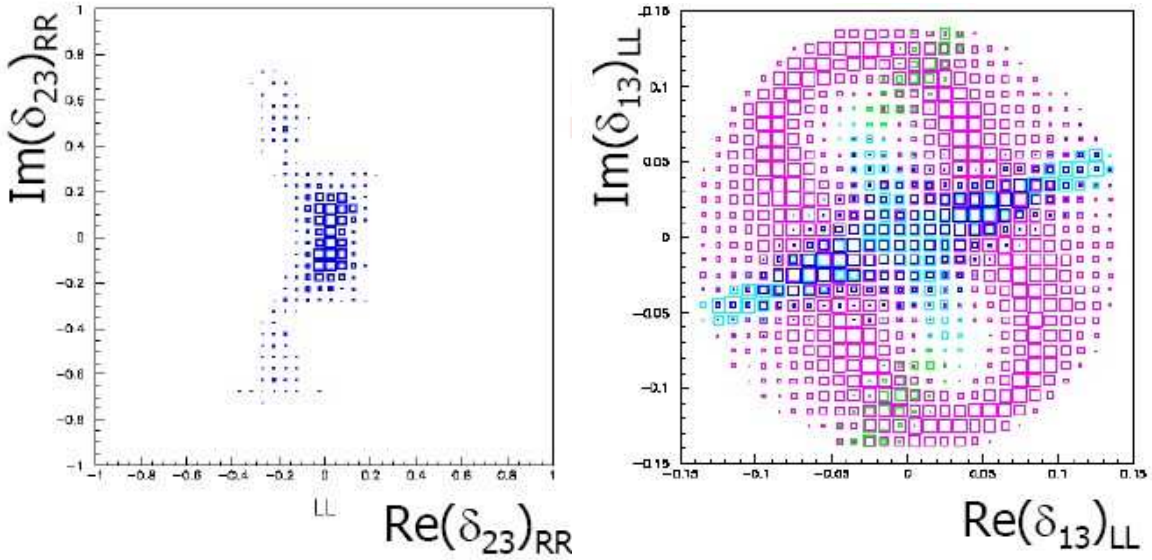

Figure 2.10: Values of Supersymmetric mass insertions allowed by experiment for the $b \to s$ (δ_{23}, left) and $b \to d$ case (δ_{13}, right). The size of a box indicates the degree to which that point is allowed, while the origin corresponds to the Standard Model. The colors in the right plot correspond to constraints from different sets of measurements.

$b \to d$ penguin-dominated process. (Both B^0 and $\overline{B}^0$ decay to this final state, so a time-dependent CP-violation measurement is possible.)

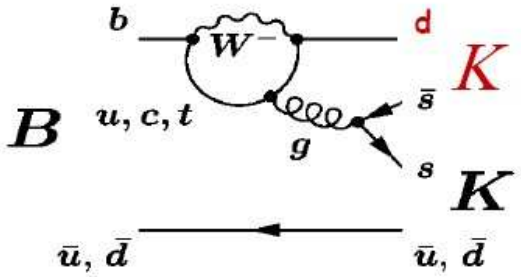

Figure 2.11: The $b \to d$ transition mediating $B \to K\overline{K}$ decays.

Relations between the branching fraction and the CP asymmetries in this mode can provide tests of SM predictions. Assuming that the top quark is dominant in the virtual loop mediating the decay through the GIM mechanism [26], the time-dependent asymmetry parameter S is expected to vanish, as then the mixing phase of the $B^0 - \overline{B}^0$ box diagram and the penguin decay phase cancel exactly:

$$\lambda_f \equiv \frac{q}{p}\frac{\overline{A}_{\overline{f}}}{A_f} = \left(\frac{V_{tb}^* V_{td}}{V_{tb} V_{td}^*}\right)\left(\frac{V_{tb} V_{td}^*}{V_{tb}^* V_{td}}\right) = 1. \tag{2.30}$$

However, contributions from up and charm quarks spoil this equality, while Supersymmetric particles could induce sizeable and thus observable asymmetries. One SM approach that uses QCD factorization methods to evaluate the strong-interaction effects of light quarks in the loop predicts $0.02 < S < 0.13$ and $-0.17 < C < -0.15$ [27]; the asymmetries are non-zero but still small. On the other hand, Fig. 2.12 shows a particular model prediction of large asymmetries for different values of the weak and strong phases of Supersymmetric contributions [28]. In general, most theoretical approaches agree that large CP-violating effects would indicate the likely presence of sizeable NP amplitudes.

The branching fraction and CP asymmetries of this mode can also be used to constrain the angles of the Unitarity Triangle. A calculation using QCD factorization

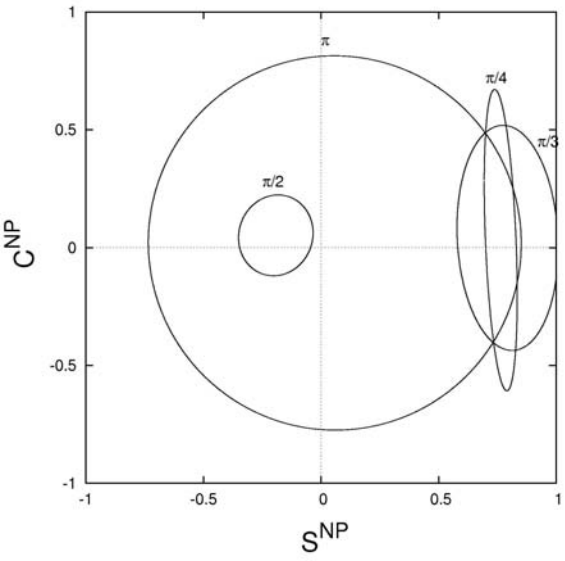

Figure 2.12: One prediction for S and C for different values of the Supersymmetric weak phase (separate circles) and strong phase ($\delta \in [0, 2\pi)$, azimuthal variation within each circle).

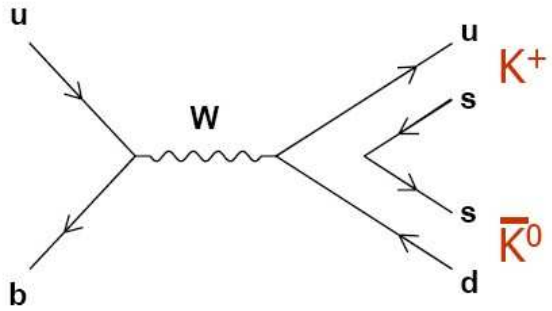

Figure 2.13: The annihilation amplitude contributing to $B^+ \to \overline{K}^0 K^+$ decays.

and perturbative QCD obtains [29]

$$\sin^2(\alpha) \sim \mathcal{B}\left(1 \pm \sqrt{1 - S^2 - C^2}\right), \tag{2.31}$$

where $\mathcal{B}$ is the branching fraction. Techniques using the U-Spin symmetry can likewise use this mode to help constrain the angle γ [30] and test predicted relations with other charmless modes [31]. In particular, the penguin amplitude in this mode is the same as in $B^0 \to \pi^+\pi^-$, up to $SU(3)$-breaking effects.

Similar conclusions hold for the direct CP asymmetry in the $B^+ \to \overline{K}^0 K^+$ mode. In addition, this mode can proceed through an additional annihilation amplitude, shown in Fig. 2.13. A comparison of the $B^+ \to \overline{K}^0 K^+$ and $B^0 \to K^0 \overline{K}^0$ branching fractions provides an estimate of the relative effect of this amplitude in the SM [32]. The measurement of the $SU(3)$-related mode $B^+ \to K^0 \pi^+$ is discussed as well.

Chapter 3

The PEP-II B Factory at SLAC

3.1 Overview

As was discussed in the previous chapter, B mesons are an ideal particle laboratory for the study of *CP* violation within and beyond the Standard Model. B factories are designed to produce copious numbers of B mesons in the pursuit of this quest. The B factory at the Stanford Linear Accelerator Center in Menlo Park, CA, comprising the PEP-II accelerator complex [33] and the *BABAR* detector [34], is described here. The B factory at KEK in Tsukuba, Japan, has a similar design [35].

In order to produce the hundreds of millions of B mesons necessary to study *CP*-sensitive rare decays, the B mesons must be produced at high luminosity in a relatively clean environment. To this end, the SLAC B factory studies electron-positron collisions at a center-of-mass (CM) energy of 10.58 GeV. This energy corresponds to the mass of the $\Upsilon(4S)$ resonance, which is a spin-1 bound state of a b quark and a b antiquark (a member of the "bottomonium" family of mesons).[1] The $\Upsilon(4S)$ mass is just above the $B\overline{B}$ production threshold, and this resonance decays almost exclusively through the strong interaction to approximately equal numbers of $B^0\overline{B}^0$ and B^+B^-

[1] 4S signifies that this resonance is the fourth state with zero orbital angular momentum between its constituent quarks in bottomonium spectroscopy. The spin of this resonance originates in the alignment of the half-integer spins of the two b quarks.

$e^+e^- \to$	Cross-section (nb)
$b\overline{b}$	1.10
$c\overline{c}$	1.30
$s\overline{s}$	0.35
$u\overline{u}$	1.39
$d\overline{d}$	0.35
$\tau^+\tau^-$	0.94
$\mu^+\mu^-$	1.16
e^+e^-	≈ 40

Table 3.1: Production cross-sections at $\sqrt{s} = M(\Upsilon(4S))$.

pairs. (The two branching fractions are measured to be equal to high precision [36].) Furthermore, at this energy approximately 20% of the hadronic e^+e^- cross-section is $b\bar{b}$ production (almost exclusively through the $\Upsilon(4S)$), resulting in a clean environment (Table 3.1).[2] A typical $\Upsilon(4S) \to B\overline{B}$ event has on average ten charged particles and twenty photons, as compared with the hundreds of charged particles in events recorded at hadronic colliders, which can also be used to study b-hadron decays.

As B mesons are pseudoscalars, the $B\overline{B}$ pair from the $\Upsilon(4S)$ decay evolves in a coherent p-wave and the two mesons have opposite flavor before one of them decays, in accordance with bose statistics. Thus, the experimenter can infer the flavor of a reconstructed B candidate ($B_{\rm rec}$) from the flavor of the other B in the $\Upsilon(4S)$ event ($B_{\rm tag}$) at the time of its decay. This can be done through charge correlations of the $B_{\rm tag}$ daughters without fully reconstructing its decay. Such flavor "tagging" of the other B in turn allows the measurement of time-dependent CP asymmetries in reconstructed final states to which both B^0 and $\overline{B}^0$ can decay.[3] The decay rate of $B_{\rm rec}$ is measured as a function of the difference in decay times of the two B's, $\Delta t \equiv t_{B_{\rm rec}} - t_{B_{\rm tag}}$.

The Δt difference is calculated from the distance between the decay vertices of

[2] *BABAR* also has an extensive charm- and tau-physics program, accessible due to the sizeable $c\bar{c}$ and $\tau^+\tau^-$ cross sections.

[3] This would be impossible otherwise, as the flavor of the reconstructed B cannot be inferred from its final-state daughters in this case.

the two B mesons. However, in $\Upsilon(4S)$ decays the B's are produced almost at rest in the CM frame ($\mathbf{p}^*_B = 340\,\mathrm{MeV}/c$, $\beta\gamma \approx 0.06$), resulting in a vertex separation of only about $30\,\mu$m by the time they decay. Such a distance cannot be resolved by typical silicon-vertex detectors, which have a spatial vertex resolution of about $50\,\mu$m. The B factories solve this problem by colliding electron and positron beams of unequal energies, thus boosting the e^+e^- system in the laboratory frame. PEP-II collides a 8.9 GeV electron beam with a 3.1 GeV positron beam, with a boost of $\beta\gamma = 0.56$. The resulting Lorentz time dilation of the B-meson lifetime elongates the average decay-vertex separation in the lab frame to about $250\,\mu$m in the beam direction, which is well within the resolution reach of silicon-detector technology. (The B mesons have negligible displacements in the plane transverse to the beam.) Nevertheless, the detector must have excellent vertex and tracking capabilities to enable this measurement and must accommodate the asymmetric nature of the collisions. I will now describe in more detail the PEP-II accelerator and the *BABAR* detector.

3.2 The PEP-II Asymmetric Collider

The PEP-II B factory is part of the accelerator complex at SLAC, shown in Fig 3.1 [33]. The electron beam is produced by the electron gun near the beginning of the two-mile long linear accelerator (the "linac"). The gun consists of a thermally heated cathode filament held under high voltage. Large numbers of electrons are "boiled off" the cathode, accelerated by the electric field, collected into bunches, and ejected out of the gun into the linac. The electron bunches are accelerated in the linac with synchronized radio-frequency (RF) electromagnetic pulses generated in RF cavities through which the beam passes by a series of 50 Megawatt klystron tubes. (Klystrons generate the pulses with their own lower energy electron beams' passing through resonant cavities.) The steering, bending, and focusing of the beam is carried out with magnets throughout the acceleration cycle.

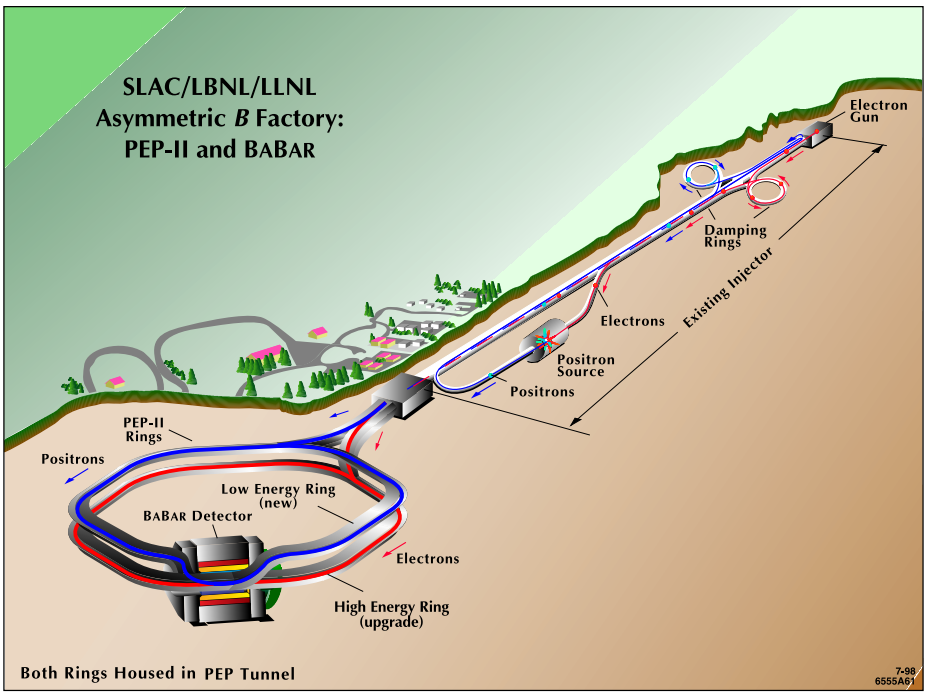

Figure 3.1: A schematic depiction of the B factory accelerator complex at SLAC.

After acceleration to an energy of approximately 1 GeV, the electron beam is directed to a damping ring, where the beam is stored for some time. As it circulates in the ring, it loses energy through synchrotron radiation and is continuously re-accelerated by RF cavities. The radiation and careful re-acceleration has the effect of reducing the emittance, or spatial and momentum spread of the beam, a necessary step in high-luminosity collisions. The "damped" beam is then re-directed to the linac and accelerated to 8.9 GeV.

Half of the generated electron bunches are used for the generation of the positron beam. They are accelerated to approximately 30 GeV, extracted from the linac, and directed onto a tungsten target, producing electromagnetic showers that contain large numbers of electron-positron pairs. The positrons are separated electromagnetically from the electrons, collected into bunches, accelerated, and sent through the return line to the source end of the linac. The positron beam is then accelerated and shaped like the electron beam through the linac and its own damping ring, culminating in an energy of 3.1 GeV.

After reaching their respective collision energies, the electron and positron beams are extracted from the linac and directed to the PEP-II storage rings, the High-Energy Ring (HER) for electrons and the Low-Energy Ring (LER) for the positrons, both housed in the same tunnel of 2.2 km circumference. As they circulate, they are focused further by a complex of magnets and accelerated by RF cavities to compensate the synchrotron-radiation losses. In the interaction region IR-2 (one of twelve such regions), where the *BABAR* detector is located, they are brought to a collision after a final-focus system squeezes the beams to the smallest possible emittance. During data taking, each ring contains about 1600 circulating bunches colliding every 5 ns. The collisions are then analyzed by the *BABAR* detector. About 10% of the time the beams are collided at an energy 40 MeV below the $\Upsilon(4S)$ resonance for calibration of the backgrounds, as no B mesons are produced then since this energy is below the $B\overline{B}$ threshold.

As data is collected, the collision and other losses reduce the currents in the rings, necessitating re-injection of electron and positron bunches. Initially in the life of the B factory from 1999-2002, data was taken for about an hour or two while the currents diminished, and then additional current was injected into the rings for a few minutes. Data could not be taken during injection due to the large backgrounds in the detector and the resulting danger to instrumentation. (The detector would have to be put into a "safe" but non-operational state during injection, with, for example, all high-voltage components ramped down to a lower, safer potential.) Starting in 2003, a new scheme for injection, called "trickle" injection, was developed, wherein new bunches are continuously injected at a rate large enough to replenish beam losses but low enough to not damage the detector. This has allowed more efficient operation of the B-factory with 30% more integrated luminosity for a given highest instantaneous luminosity.

The PEP-II collider was designed for an instantaneous luminosity of $3\times10^{33}\,\mathrm{cm}^{-2}\,\mathrm{s}^{-1}$, but has reached values of $1.2 \times 10^{34}\,\mathrm{cm}^{-2}\,\mathrm{s}^{-1}$ due to improvements in the RF cavi-

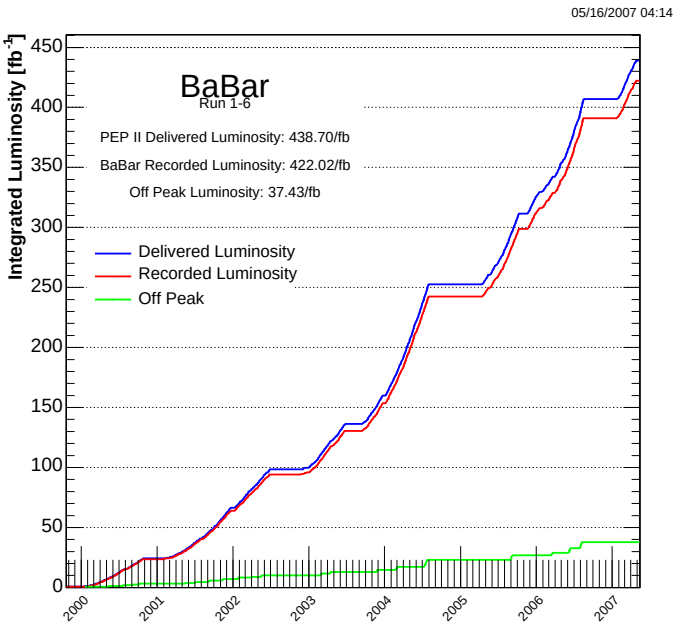

Figure 3.2: Total integrated luminosity delivered by PEP-II and recorded by the *BABAR* detector.

ties, beam-shaping cavities, and magnet systems.[4] The increased luminosity comes from larger beam currents (up to 3 A in the LER and 2 A in the HER) and a reduced emittance. Additional improvements that have been implemented will boost the instantaneous luminosity to 2×10^{34} by the end of operations in 2008. With these specifications and trickle injection, the machine generates hundreds of pb^{-1} of integrated luminosity daily during normal operations, and has integrated hundreds of fb^{-1} throughout its operating lifetime (Fig. 3.2). With a $B\overline{B}$ production cross-section of 1.1 nb, this corresponds to hundreds of millions of $B\overline{B}$ pairs. The goal of the B factory is the accumulation of about one billion such events by 2008.

[4]The luminosity is determined by measuring the rates of $e^+e^- \to e^+e^-$ Bhabha scattering and $e^+e^- \to \mu^+\mu^-$ and radiative $e^+e^- \to \mu^+\mu^-\gamma$ processes.

3.3 The *BABAR* Detector

In accordance with the B-factory environment and program, the detector must satisfy the following requirements:

- Excellent vertex reconstruction in the tracker, in both the parallel and transverse directions to the beam boost;
- Large acceptance, including at small polar angles relative to the boost direction in the lab frame;
- Excellent reconstruction efficiency and good momentum resolution for charged particles and photons from below 100 MeV to 5 GeV;
- Good charged-particle identification to separate lepton, pion, and kaon candidates;
- Radiation hardness, particularly for the inner tracking sub-detectors.

The *BABAR* detector is a large, multi-purpose hermetic detector with several components that together satisfy these requirements [34]. As shown in Fig. 3.3 the detector consists of two endcaps and a cylindrical barrel (Fig. 3.4) hugging the beam pipe along the z direction and roughly symmetric in the azimuth ϕ. The right-handed coordinate system is defined with the z axis pointing in the e^- direction, x pointing horizontally away from the center of the PEP-II rings, and y pointing upwards. The geometrical center is offset from the beam-beam interaction point towards forward polar angles to maximize the geometric acceptance for the boosted $\Upsilon(4S)$ decays.

The sub-detectors are arranged in layers of increasing distance from the beampipe. The silicon vertex tracker (SVT), the innermost detector, is used for vertexing particle decays and is the main source of information on the polar angle of charged particles. The Drift Chamber (DCH) is the main device for measuring charged-particle momenta with good resolution through gaseous wire-chamber technology. A Detector of

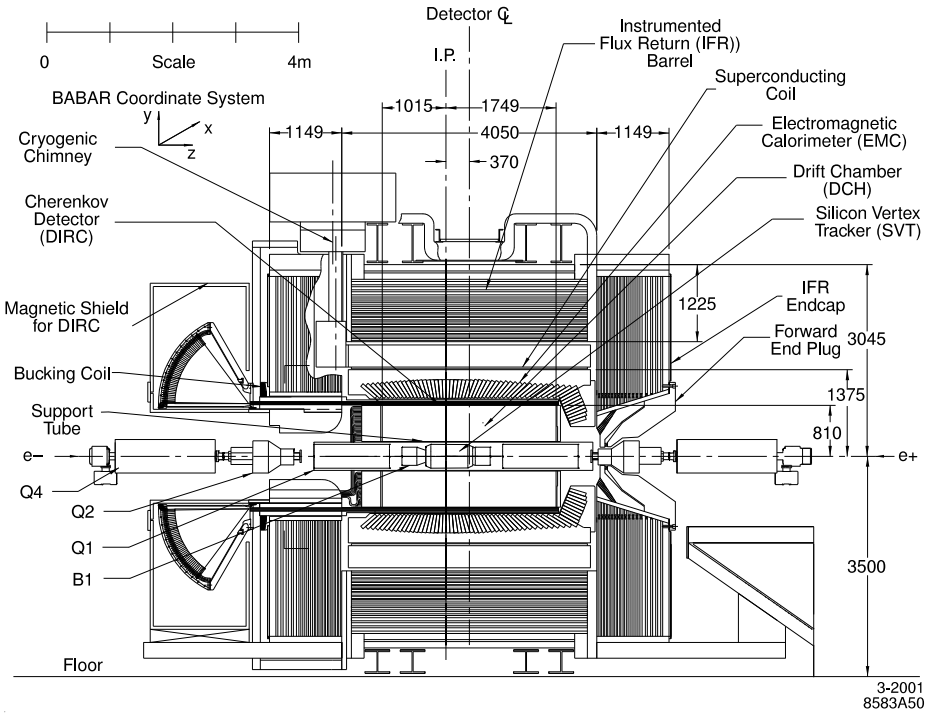

Figure 3.3: Longitudinal cross section of the *BABAR* detector.

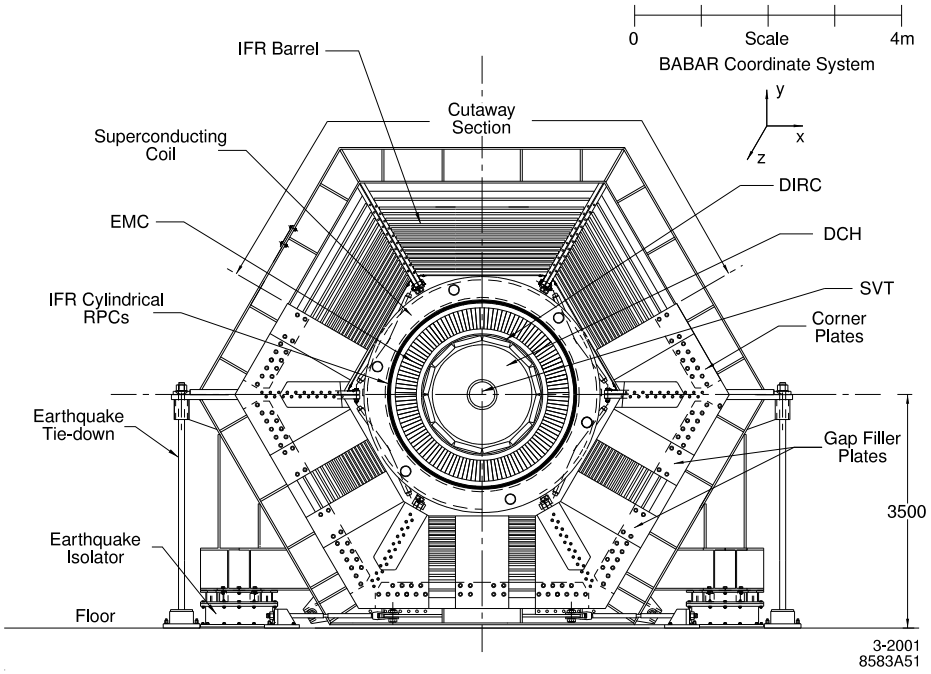

Figure 3.4: Transverse cross-section of the barrel of the *BABAR* detector.

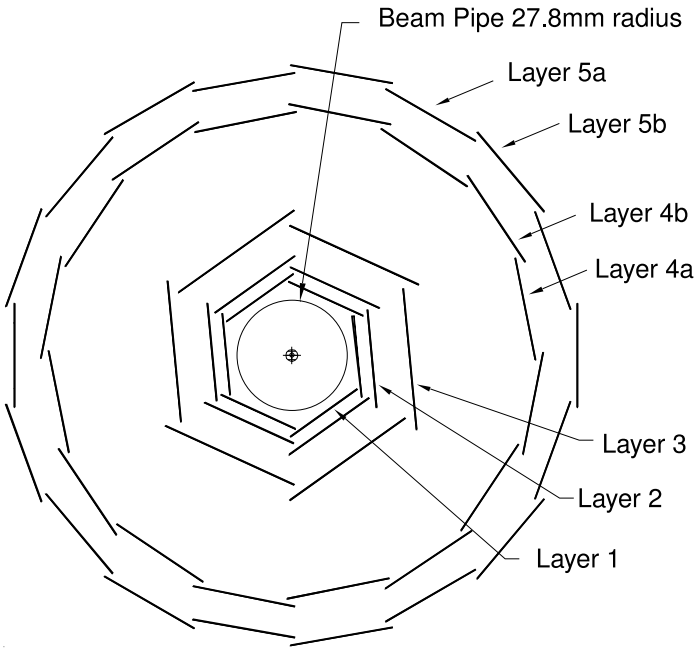

Figure 3.5: Transverse cross section of the SVT.

Internally Reflected Cherenkov Light (DIRC) is used to separate pions from kaons, while a crystal Electromagnetic Calorimeter (EMC) is used for energy measurement of photons and electrons and for electron identification. These components are placed within a 1.5-Tesla solenoidal magnet that provides the magnetic bending of charged particles needed to measure their momenta. Outside the magnet is the Instrumented Flux Return (IFR), which is used for the identification of muons and long-lived neutral hadrons. The detector signals are processed through detector electronics, and examined by a trigger system that selects physically interesting collision data to be stored. Various online and offline reconstruction procedures are employed to convert the data into a format amenable to analysis for the study of relevant B decays and other processes.

3.3.1 The Silicon Vertex Tracker

The SVT consists of five layers of double-sided silicon sensors segmented in both the z and ϕ directions, designed to measure accurately the positions and decay vertices

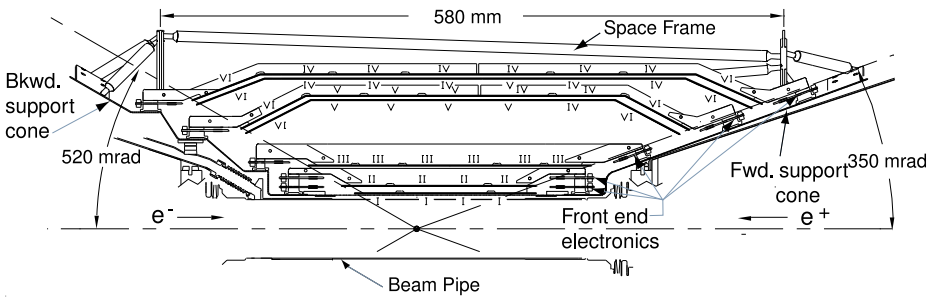

Figure 3.6: Side view of the SVT.

of B mesons and other particles (Fig. 3.5). This measurement is most accurate at small distances from the interaction point, as the trajectory of the particles farther away is affected by multiple scattering within the detector. Thus, the first three layers are located as close to the beampipe as possible. The outer two layers are closer to the drift chamber to facilitate matching of SVT tracks with DCH tracks. They also provide pattern recognition in track reconstruction, and the only tracking information for charged particles with transverse momenta below 120 MeV/c, as these may not reach the drift chamber. The SVT covers 90% of the solid angle in the CM frame (Fig. 3.6).

The silicon sensors are 300 μm-thick high-resistivity n-type silicon wafers, with n^+ and p^+ strips running orthogonally on opposite sides. As high-energy particles pass through the sensor they displace orbital electrons, producing conducting electrons and positive holes that then migrate under the influence of an applied depletion voltage. The resulting electrical signal is read-off from the strips, amplified, and discriminated with respect to a signal threshold by front-end electronics. The time over threshold of the signal is related to the charge of the signal and is read out by the data acquisition system for triggered events. The position resolution is in the 10 μm-50 μm range, depending on the orientation of the strip (ϕ or z) and the layer number.

The SVT is water-cooled and monitored for temperature, humidity, and position variations. Local and global position alignment is performed frequently in the online reconstruction software. As the SVT has to withstand a lifetime integrated radiation

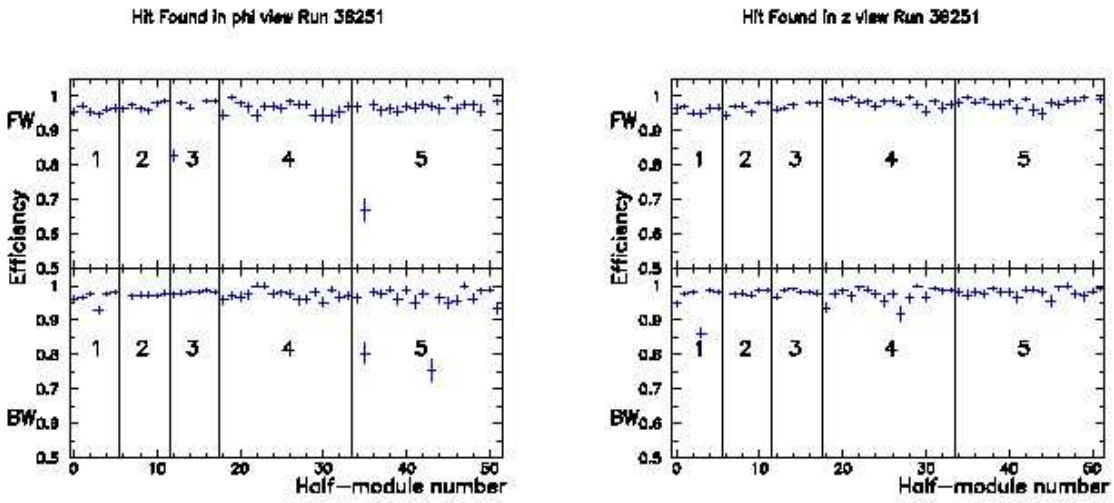

Figure 3.7: SVT reconstruction efficiency in the ϕ view (left) and the z view (right) as measured in $e^+e^- \to \mu^+\mu^-$ events.

dose of 2 Mrad, the sensors have a high threshold for radiation damage. Nevertheless, they are easily damaged by high instantaneous or integrated doses, and an extensive system of radiation monitoring with PIN and diamond diodes can abort the beams if dangerous background levels develop. Up to 2007 the monitoring systems have prevented any significant damage from occurring and the SVT has performed extremely well, with an average track reconstruction efficiency of 97% (Fig. 3.7).

3.3.2 The Drift Chamber

The Drift Chamber, a gaseous wire detector, is the primary tracker used for the measurement of the momenta of charged particles, as well as the only tracking device for the subset of long-lived particles such as K_S^0's that decay outside of the SVT. In addition, the DCH provides particle-identification capability by measuring track ionization losses as a function of position ($\mathrm{d}E/\mathrm{d}x$), particularly for tracks with momenta less than 700 MeV/c.

The inner wall of the drift chamber is placed close to the SVT outer wall to facilitate track-matching between the two devices. The chamber is 2.8 m long and

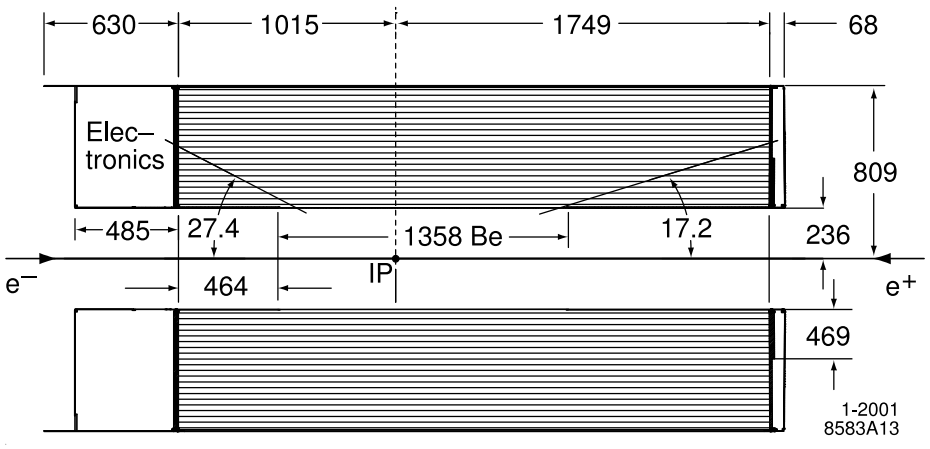

Figure 3.8: Side view of the DCH.

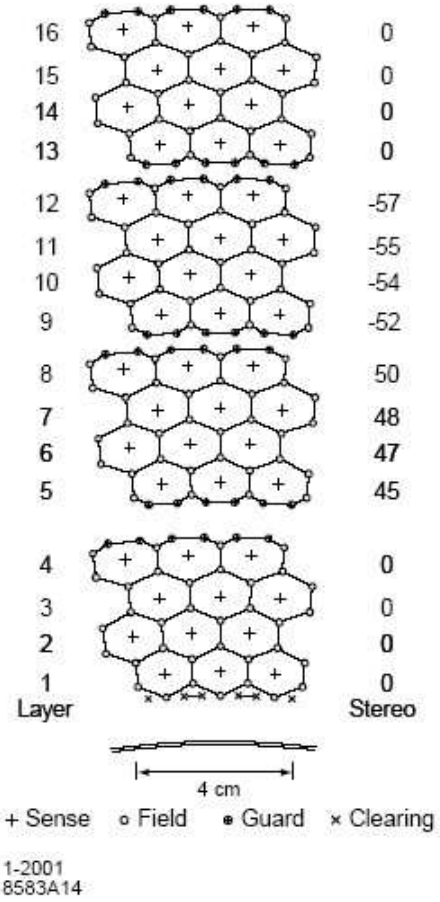

Figure 3.9: A schematic of the arrangements of the wires in the hexagonal cells of the DCH.

consists of 40 cylindrical layers of 12 mm by 19 mm hexagonal cells, each consisting of six field wires at the corners and one field wire in the center as shown in Figs. 3.8

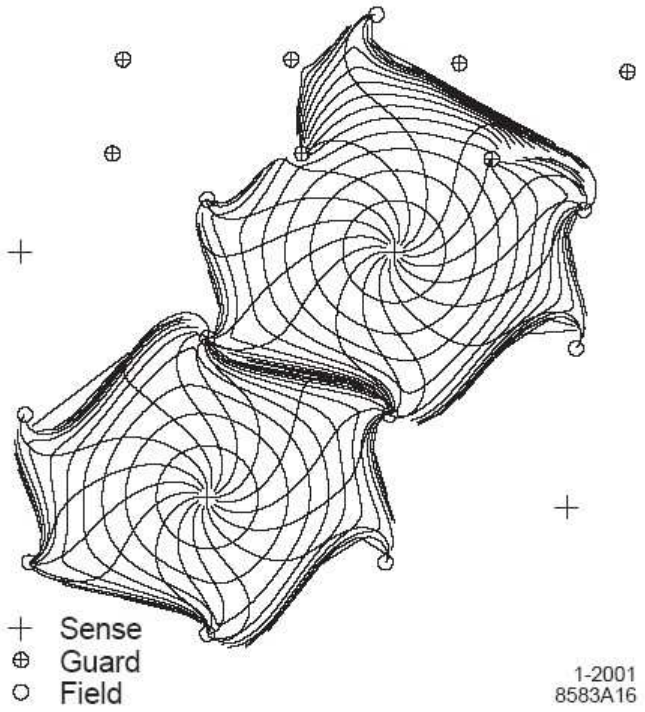

Figure 3.10: Isochrones in a typical DCH cell.

and 3.9.[5] The field wires are grounded, while the sense wire is held at high voltage, typically around 1900 V. The space around the wires is filled with a gas mixture containing 80% helium and 20% isobutane. High-energy particles ionize the gas as they traverse it, and the liberated electrons are then accelerated toward the sense wires, ionizing additional electrons, which are in turn accelerated themselves and result in the formation of a gas avalanche of electric charge. The avalanche collects on the sense wire with drift times of 10-500 ns and the charge and timing information of the signal is read-off through electronic circuits AC-coupled to the wire. The gain relative to the charge of the primary ionization is about 5×10^4. The grounded field wires produce a uniform electric field in the cell with evenly distributed isochrones, or contours of equal drift time, as shown in Fig. 3.10. "Stereo" wires in 24 of the 40 layers are placed at small angles with respect to the z direction in order to provide longitudinal information. The chamber has a typical position resolution of 140 μm.

[5]The 40 layers are grouped into 10 superlayers of 4 layers each.

Isobutane has large molecules with rotational degrees of freedom that can absorb electrical energy, and its presence in the gas mixture limits the growth of the avalanche in order to protect the chamber from damaging levels of accumulated charge. The choice of the gas mixture is motivated by considerations of aging and avalanche size as well as minimizing multiple scattering in the chamber, which is accomplished by choosing helium as the primary gas component and aluminum as the lightweight material for the multiple field wires.[6] The gas is circulated to flush out any degraded components, with one full volume of fresh gas ($5.2\,\mathrm{m}^3$) added every 36 h. In addition, the water content of the gas is maintained by a water bubbler at 3500 ± 200ppm and oxygen is removed with a catalytic filter, both measures designed to prevent Malter-effect discharges in the gas that would degrade the performance and aging behavior of the chamber.

The DCH has demonstrated excellent performance throughout the life of *BABAR* with track-reconstruction efficiencies at the 95% level. This includes the effect of disconnecting a fraction of the wires in superlayers 5 and 6 that were damaged during the commissioning phase. The $\mathrm{d}E/\mathrm{d}x$ response, with a resolution of about 7%, is shown in Fig. 3.11, and a new calibration in 2006 has improved the PID potential of this capability for high-energy tracks. The achieved resolution on transverse momentum is $\sigma_{p_\mathrm{t}}/p_\mathrm{t} = (0.13 \pm 0.01)\% \cdot p_\mathrm{t} + (0.45 \pm 0.03)\%$, where p_t is given in units of GeV/c.

3.3.3 The Detector of Internally Reflected Cherenkov Light

The DIRC is the main PID sub-detector of *BABAR*, providing $\pi{-}K$ separation of 2.5σ or more over the momentum range $700\,\mathrm{MeV}/c{-}4.2\,\mathrm{GeV}/c$. It is thin and light, minimizing the size and the impact on performance of the EMC that is located outside the DIRC in the radial direction. Cherenkov devices detect light radiated by particles that move faster than the speed of light in a given medium, with the Cherenkov angle

[6] The total thickness of the DCH at normal incidence is only 1.08% of the radiation length.

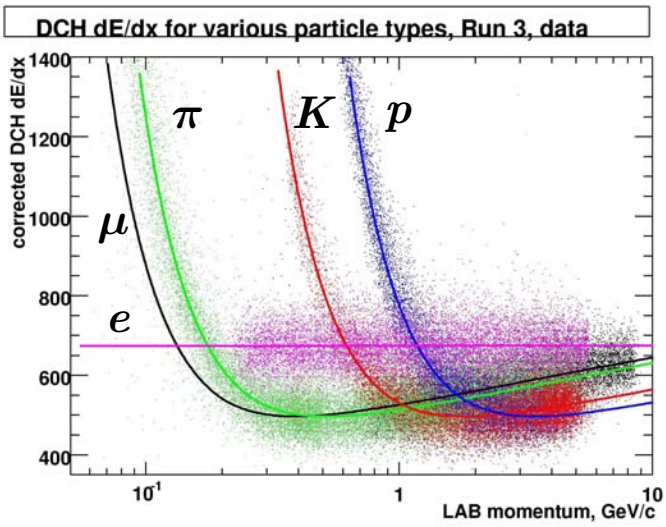

Figure 3.11: dE/dx in the DCH as a function of track momentum for different charged particles: protons (blue), kaons (red), pions (green), muons (black), and electrons (magenta).

θ_C of the radiated photons given by

$$\cos(\theta_C) = \frac{1}{n\beta} = \frac{c}{nv}, \tag{3.1}$$

where n is the index of refraction of the medium and v is the particle's velocity. For a given momentum, particles of different mass will have different velocities, differentiating particle-mass hypotheses for a track and thus different PID hypotheses.[7]

The DIRC consists of 144 bars made of fused silica running along the z direction, with dimensions of 17 mm by 35 mm and 4.9 m in length. The silica serves as the Cherenkov radiator, with the high index of refraction of $n = 1.437$, and as a waveguide, with a low attenuation length. A charged particle passing through radiates Cherenkov photons, which then propagate to the longitudinal end of the bar, trapped within by total internal reflections at the flat boundaries of the bar. Each reflection preserves the original Cherenkov angle. At the end of the bars, the photons pass through a standoff box filled with purified water that has a similar refractive index

[7]The velocity of the track must be above the Cherenkov threshold, $v > c/n$.

of $n = 1.346$, so that refraction at the silica-water boundary is minimized. The water must be highly transparent as the photons pass through about one meter of water in the standoff box, so it is filtered, de-gassed, de-ionized, exposed to UV radiation to prevent the growth of bacteria, and treated with a reverse-osmosis unit.

The rear surface of the standoff box is instrumented with 12 sectors of 896 photomultiplier tubes (PMTs) each, which collect the photons, convert them to electrons with photocathodes, and amplify the signal using the gas-avalanche principle. As the standoff box is located outside the solenoid magnet, it is possible to limit the magnetic field in its volume to about 1 Gauss with a bucking coil that counteracts the field of the solenoid. Thus, conventional PMTs, which do not tolerate high magnetic fields, can be used. To limit the number of PMTs, there is only one standoff box, located at the backward end of the detector to exploit the forward boost environment of the collisions. The forward ends of the silica bars have mirrors perpendicular to the axis of the bars, so that forward-pointing photons are reflected and reach the backward end of the bars as well. The detector is depicted schematically in Fig. 3.12. The total photon detection efficiency is at the 5% level, with the average number of detected photons ranging from 20 at normal track incidence to 65 at large polar angles.

As the Cherenkov angle of the emitted photons is preserved, it can be reconstructed from the PMT signals, the timing information, and the track momentum vectors obtained by matching the signal with tracks from the DCH and SVT. The resolution on the single-photon Cherenkov angle $\theta_{\mathrm{C},\gamma}$ is 10.2 mrad, while the resolution that can be obtained for a track from all its radiated photons is

$$\theta_{\mathrm{C,track}} = \frac{\theta_{\mathrm{C},\gamma}}{\sqrt{N_\gamma}}, \tag{3.2}$$

where N_γ is the number of detected photons. This yields typical track angular resolutions of 3 mrad.

The resulting $\pi - K$ discrimination is crucial for the $B^+ \to \overline{K}^0 K^+$ analysis, where

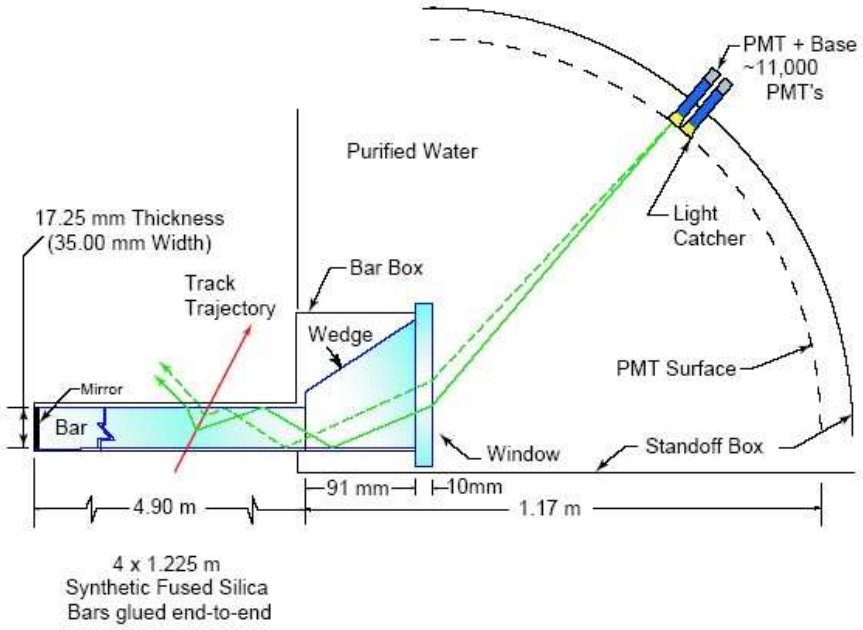

Figure 3.12: Schematic layout of the DIRC.

$\overline{K}^0 K^+$ candidates have to be separated from $K^0\pi^+$ candidates. The discriminating power of the DIRC over the track-momentum range relevant for this analysis is shown in Fig. 3.13. The analysis uses a calibration of the DIRC response obtained with a control sample of $D^{*+} \to D^0\pi^+(D^0 \to K^-\pi^+)$ decays, where highly accurate PID can be obtained independently of the DIRC from charge correlations of the tracks.

3.3.4 The Electromagnetic Calorimeter

The EMC is designed to detect electromagnetic showers from photons and electrons with excellent energy and angular resolution over the energy range of 20 MeV to 9 GeV. This functionality is necessary to reconstruct π^0 and η^0 mesons that decay to two photons, as well as for identification of high-energy photons from rare radiative B decays. The electron ID is necessary for J/ψ reconstruction, for tagging the flavor of the non-signal B in the event through semileptonic decays (see section 3.1), as well as for reconstruction of semileptonic and rare B decays. The detector must be hermetic

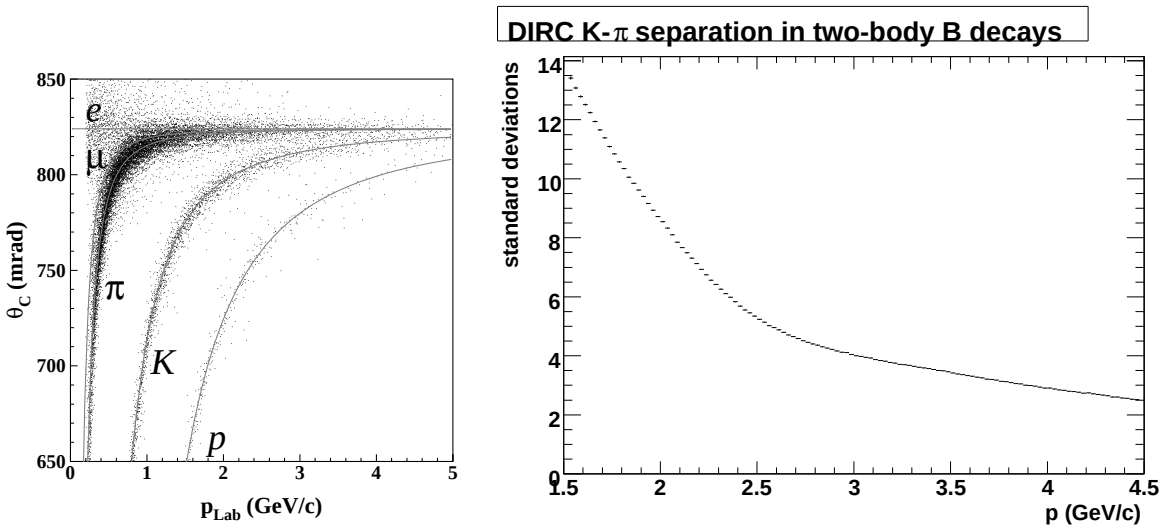

Figure 3.13: The dependence of the measured Cherenkov angle $\theta_{\rm C}$ in the DIRC on track momentum $p_{\rm Lab}$ for different charged particles (left). The right plot illustrates the $\pi-K$ separation for two-body B decays in units of standard deviations.

and operate within the 1.5-T magnetic field. The amount of material in front of the EMC has been kept to a minimum in the design of the *BABAR* detector in order to allow for the detection of photons and electrons down to energies of 20 MeV.

The EMC is composed of 6580 Thallium-doped Cesium iodide (CsI(Tl)) scintillating crystals (Fig. 3.14), separated into a cylindrical barrel of 48 rings and a forward endcap of eight rings (Fig. 3.15). The EMC covers 90% of the CM acceptance and does not contain a backward endcap as the CM acceptance is low at backward polar angles. CsI(Tl) was chosen for its high light yield of $50,000\,\gamma/\,\mathrm{MeV}$, allowing for excellent energy resolution, and its small Molière radius of 3.8 cm, which allows for excellent angular resolution.[8] The transverse segmentation is at the scale of the Molière radius to optimize the angular resolution while limiting the number of crystals and readout channels. The crystals serve as radiators for the traversing electrons and photons, with a short radiation length of 1.85 cm.[9] The crystals scintillate under the influence of the showers, and the light is then passed through total internal reflection

[8]The Molière radius is the intrinsic limit of the position resolution of electromagnetic showers in a crystal.

[9]The EMC is thus a "total" absorption calorimeter.

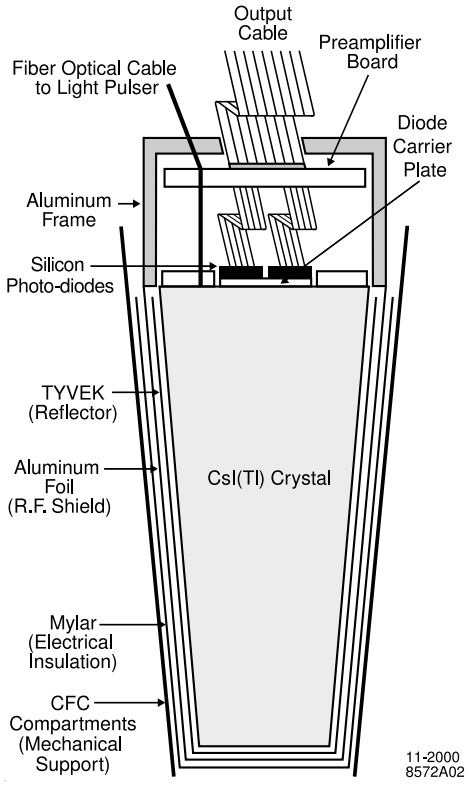

Figure 3.14: A schematic view of the EMC crystal.

to the outer face of the crystal, where it is read out by silicon PIN diodes. As these diodes are well suited for operation in the high magnetic fields in the EMC, part of the motivation for the crystal choice was that the frequency spectrum of CsI(Tl) is detected by silicon PIN sensors with the high quantum efficiency of 85%. The EMC is cooled by water and Fluorinert coolant and monitored for changes in the environmental and radiation conditions and for changes in the light response of individual crystals.

The energy response of the EMC is calibrated using low-energy photons from a radioactive source and high-energy photons from radiative e^+e^- Bhabha events. As electromagnetic showers spread throughout several crystals, a reconstruction algorithm is used to associate activated crystals into clusters and either to identify them as photon candidates or to match individual maxima of deposited energy to extrapolated tracks from the DCH-SVT tracker. Additional PID is obtained from the spatial

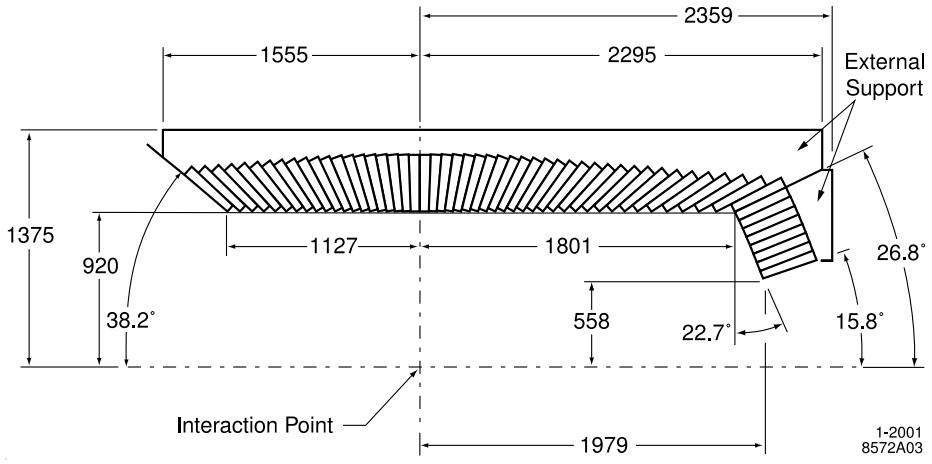

Figure 3.15: Longitudinal cross section of the EMC, showing the 56 rings of crystals.

shape of the shower. The energy and angular resolutions are determined to be

$$\frac{\sigma_E}{E} = \frac{(2.32 \pm 0.30)\%}{\sqrt[4]{E(\,\mathrm{GeV})}} \oplus (1.85 \pm 0.12)\%, \tag{3.3}$$
$$\sigma_\theta = \sigma_\phi = \frac{(3.87 \pm 0.07)\,\mathrm{mrad}}{\sqrt{E(\,\mathrm{GeV})}} \oplus (0.00 \pm 0.04)\,\mathrm{mrad}.$$

In both cases, the first term is due to fluctuations in the number of photons and to electronic noise of the photon detector and electronics, while the second term arises from the non-uniformity of light collection, leakage and absorption due to materials between and in front of the crystals, and calibration uncertainties. Figure 3.16 shows the agreement between data and simulation of the angular resolution of the EMC and its π^0-reconstruction performance.

3.3.5 The Instrumented Flux Return

The IFR is the primary muon detector at *BABAR* and is also used for the identification of long-lived neutral hadrons (primarily K_L^0's). This capability is important for the leptonic measurements discussed in the above description of the EMC but in the muon rather than electron channels. The IFR is divided into a hexagonal barrel, which covers 50% of the solid-angle in the CM frame, and two endcaps (Fig. 3.17).

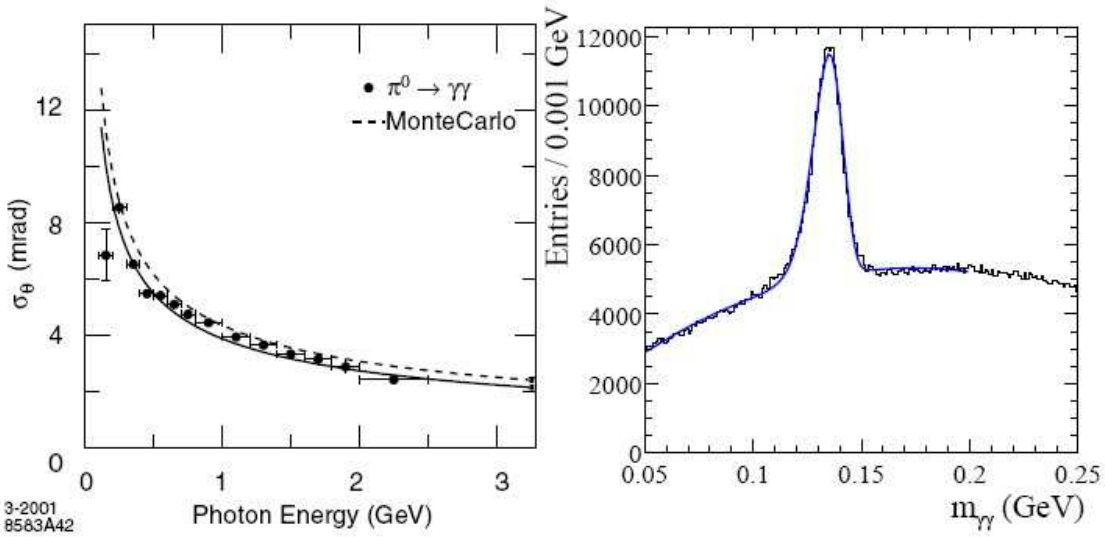

Figure 3.16: Angular resolution in the EMC as a function of photon energy (left) and the reconstructed diphoton peak at the π^0-mass region.

Originally, it consisted of layers of steel of varying thickness interspersed with Resistive Plate Chambers (RPCs), 19 layers in the barrel and 18 in each endcap.[10] The steel serves as a flux return for the solenoidal magnet as well as a hadron absorber, limiting pion contamination in the muon ID. RPCs were chosen as they were believed to be a reliable, inexpensive option to cover the 2000 m^2 of instrumented area in this outermost region of *BABAR* with the desired acceptance, efficiency, and background rejection for muons down to momenta of 1 GeV/c.

The RPCs detect high-energy particles through gas-avalanche formation in a high electric field. The chambers consist of 2 mm-thin bakelite sheets kept 2 mm apart by an array of spacers located every 10 cm (Fig. 3.18). The space in between is filled with a non-flammable gas mixture of 56.7% argon, 38.8% freon 134a, and 4.5% isobutane, while the sheets are held at a potential of 8000 V. The inside surface of the bakelite is smoothed with a linseed-oil coating so that the electric field is uniform, thus preventing discharges in the gas and large dark currents. The RPCs operate in streamer mode, wherein the avalanche grows into a streamer, a mild, controlled

[10] Additional cylindrical RPCs were placed just outside the solenoid magnet to improve the matching between IFR and EMC showers.

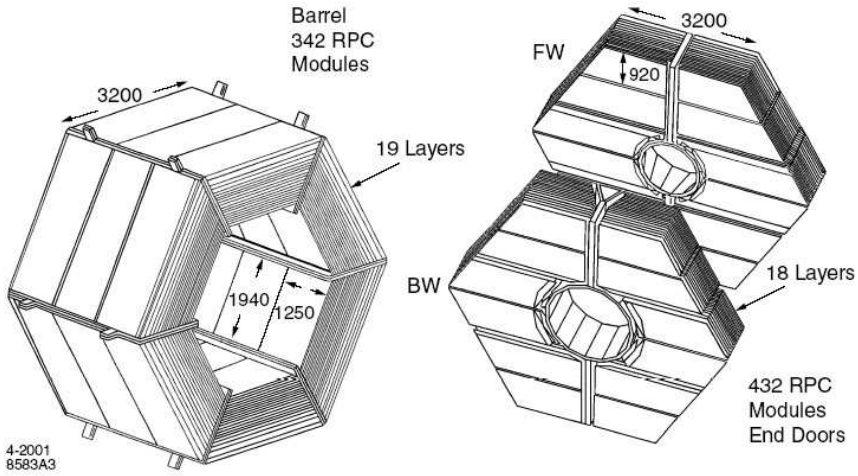

Figure 3.17: Drawing of the IFR barrel and endcaps.

form of electrical discharge in the gas. The streamer charge is read out in both the ϕ and z directions by aluminum strips located outside and capacitively coupled to the chamber. The streamer is kept from producing electrical breakdown of the gas by the quenching action of the freon and isobutane molecules, as described in the description of the DCH.

In streamer mode, the gas gain is at the 10^8 level. The factor of $10-1000$ increase in gain over avalanche mode greatly simplifies the readout electronics. Moreover, the charge of the streamer is independent of the primary-ionization charge, resulting in an effectively digital signal with high efficiency.[11] Initially, the RPCs performed at over 90% efficiency as expected geometrically from inactive space in the detector, resulting in a muon detection efficiency of 90% for a pion misidentification rate of $6-8\%$ in the momentum range of $1.5 < p < 3.0\,\mathrm{GeV}/c$, as shown in Fig. 3.19.

Shortly after the start of data-taking with *BABAR* in 1999, the performance of the RPCs started to deteriorate rapidly. Numerous chambers began drawing dark currents and developing large areas of low efficiency. The overall efficiency of the RPCs started to drop and the number of non-functional chambers (with efficiency

[11]The DCH operates in proportional avalanche mode, where the size of the signal is proportional to the charge of the original ionization, complicating the read-out.

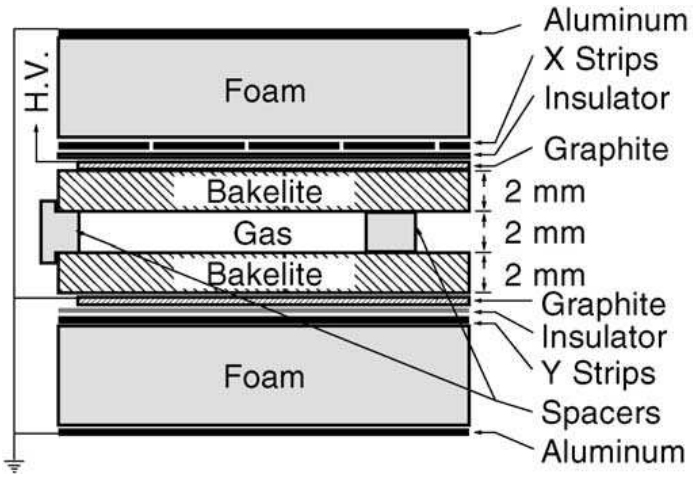

Figure 3.18: Cross section of a *BABAR* RPC.

less than 10%) rose dramatically (Fig. 3.20), deteriorating muon ID. The problem was traced to insufficient curing and R&D of the linseed-oil coating and to the high temperature at which the RPCs were operated initially. Uncured oil droplets would form columns under the action of the strong electric field and the high temperature (up to 37 deg C), bridging the bakelite gap and resulting in large currents and dead space (Fig 3.21). Various remediation measures were attempted, including flowing oxygen through the chambers to cure the oil and introuducing water cooling of the IFR, but they did not solve the problem. Extrapolating the efficiency trend showed a clear path towards losing muon ID capability at *BABAR* within a couple of years of operations, so an upgrade of the IFR detector was deemed necessary by the collaboration.

The forward endcap was retrofitted with new improved RPCs in 2002. The new chambers were screened much more stringently with QC tests and had a much thinner linseed-oil coating that was properly cured and tested. They have performed well since then. The backward endcap was not retrofitted, as its acceptance in the CM frame is small. In the barrel, the collaboration decided to upgrade the detector with Limited Streamer Tube (LST) technology. The RPCs were removed and replaced by 12 layers of LSTs and 6 layers of brass to improve hadron absorption. (The last layer of RPCs is inaccessible, so the old chambers there were disconnected from all utilities but kept

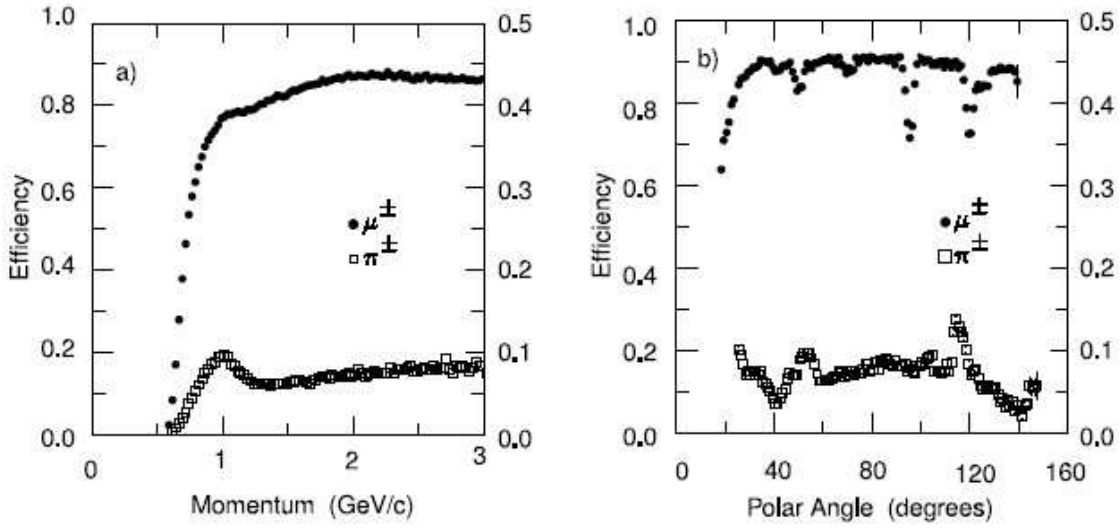

Figure 3.19: Initial muon-identification performance of *BABAR* RPCs.

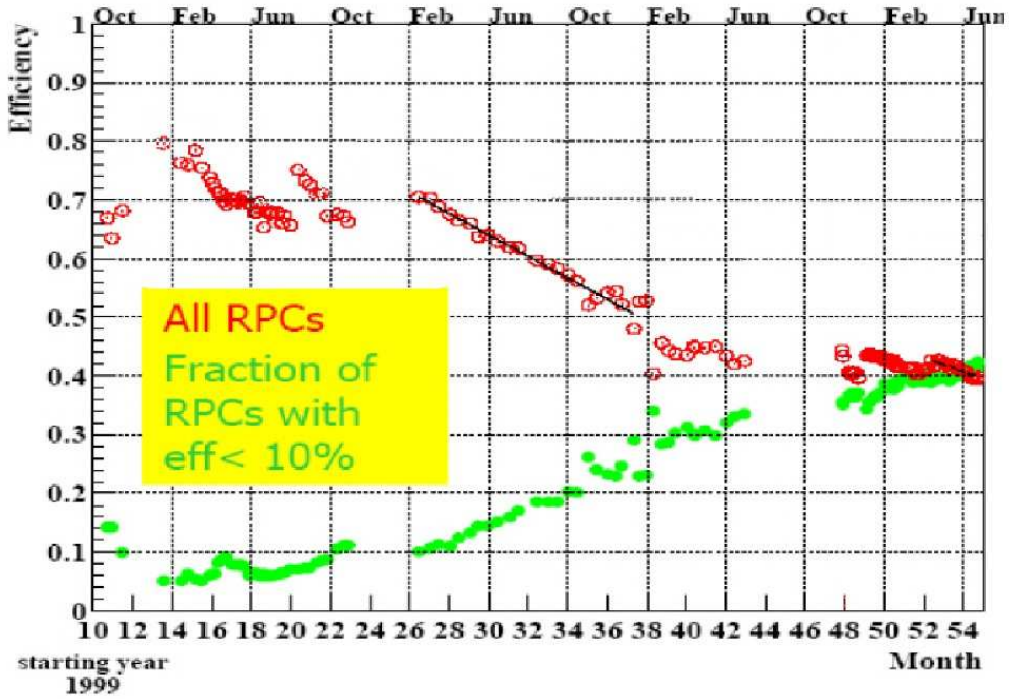

Figure 3.20: Deterioration with time of the average RPC efficiency (red). The green dots show the fraction of RPCs with efficiency lower than 10%.

in place.) As the author was heavily involved in this upgrade and as the project was a laborious and careful but time-sensitive project undertaken at a mature age of the experiment, it will be described in more detail than the other components of the

Figure 3.21: Photographs of defects on the linseed oil coating of a malfunctioning RPC.

detector.

Figure 3.22: The mechanical structure of *BABAR* LSTs.

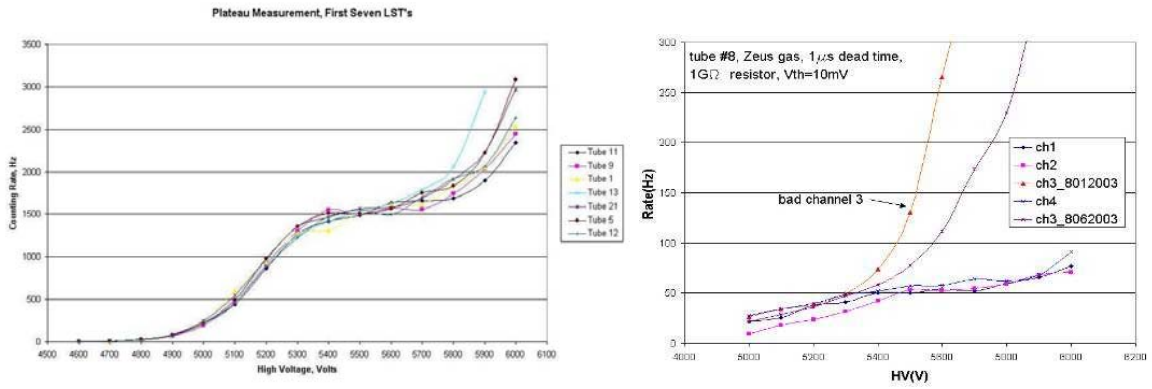

Figure 3.23: A singles' rate plateau seen versus applied voltage for several LSTs (left). Defects in the chamber can spoil the plateau (right).

The LSTs consist of a PVC comb of eight 15 mm by 17 mm cells about 3.5 m in length, encased in a PVC sleeve, with a 100 μm gold-plated beryllium-copper wire running down the center of each cell (Fig. 3.22). The cells in the comb are covered with graphite, which is grounded, while the wires are held at 5500 V and held in place by wire holders located every 50 cm. The gas mixture consists of 3.5% argon, 8% isobutane, and 88.5% carbon dioxide. Like the RPCs and as their name implies, the LSTs are operated in streamer mode. The signal is read off directly from the wires through AC-coupled electronics (granularity of two wires per channel in the ϕ direction) and from strips running perpendicular to the tubes and capacitively coupled to the wires (35 mm pitch in the z direction).

Experience with the RPCs underscored the crucial role of R&D and QC at every level of development of the new technology. Thus, during R&D at Princeton stringent QC methodology was developed after the final design of the tubes was chosen. During construction, the mechanical quality of the graphite surface was inspected and the resistivity tested. The chambers were strung with wires tested for thickness and tested for gas leaks after sealing. The tubes were then conditioned under progressively higher applied voltages to burn off any dirt accumulated during construction. Only tubes that could hold the operational voltage without drawing excessive currents were accepted.

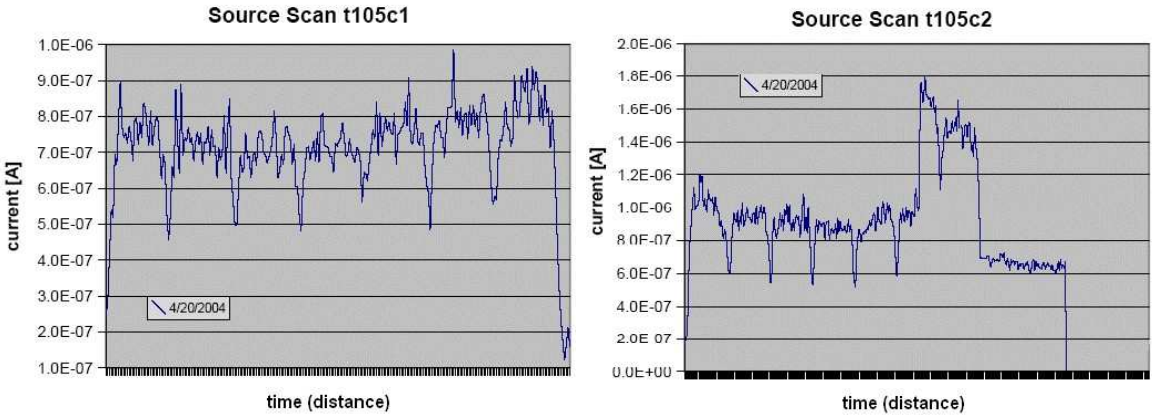

Figure 3.24: Plot of the current drawn by an LST versus position of the source as it scans along the length of the chamber (left). The dips correspond to the geometrically inefficient regions located every 0.5 m around the wire holders. Defects in the chamber can cause self-sustaining high-current discharges (right).

One of the crucial performance characteristics was the "singles'-rate", or counting-rate, plateau. As the streamer signals are effectively digital, given a constant incident flux of particles, the chamber should show a counting-rate plateau over a range of applied voltage where the charge of every streamer is above the read-out threshold (Fig. 3.23). The plateau provides operational tolerance of the applied HV, allowing operations of the LSTs at the middle of the plateau to safeguard against fluctuations in efficiency due to changes in the gas gain from pressure or voltage fluctuations. Defects in the surface of the graphite or dirt accumulated on the wire can result in large discharges in the tube (including the Malter effect) that raise the singles' rate and spoil the plateau (Fig. 3.23). In addition, a short plateau is an indication of poor aging behavior. Thus, the quality of the plateau is a powerful QC test.[12]

Another powerful QC procedure is scanning the tube with a localized, focused radioactive source, subjecting small regions of the tube to intense radiation rates. Although the incident flux is then much higher than what the tube would experience in the experiment, the stress reveals weak points in the tube, where the source initiates

[12]The plateau eventually fails at 5900 V or higher due to multiple streamers formed from electrons photoelectrically ejected from the graphite by UV photons radiated by the original streamer. At high voltages, enough UV photons are produced to overwhelm any signal dead-time imposed by the electronics, thus raising the singles' rate.

a self-sustaining discharge of high current that continues even when the source is removed while the high-voltage is applied (Fig. 3.24).[13] Only tubes that do not exhibit this behavior are accepted for installation.

The LSTs were constructed at PolHiTech, an Italian company that was located in Carsoli, outside of Rome. The construction and QC procedures outlined above were conducted under the supervision of *BABAR* personnel. After all QC tests, the tubes were held under high voltage for a month to verify that no premature aging behavior occurred. Thereafter, they were assembled into modules of two to three tubes at Princeton University and The Ohio State University and then shipped to SLAC for installation, which occurred in two stages: two sextants of the hexagonal barrel in the Summer of 2004 and the remaining four sextants in the Fall of 2006.[14] QC procedures were performed at every step to make sure that only the best tubes were installed in the detector. The engineering and installation effort was led by Princeton University, employing the engineering and machining resources of EP Lab (Elementary Particle Laboratory).

By the time the LSTs arrived at Princeton, only about 5% of the tubes did not pass QC. Most of these were recovered with remediation techniques such as treatment with negative high voltage. Negative potential (-3000 to -4000 V) induces a corona discharge around the wires and the ion flow towards the wire is able to eliminate dirt or debris that has accumulated. (At this advanced stage of QC most tubes with permanent mechanical defects have been eliminated and problems arise mostly from removable debris introduced into the tube during the assembly process.) The small number of tubes that were not cured this way were opened up in a clean room and defects in the graphite coating or dirt on the wire removed manually. The remediated tubes were only used as spares for installation.

The project involved the manufacture of 1500 LSTs including contingency, with

[13] This happens when a conductive channel is formed in the gas around a mechanical defect.

[14] The delay of the second phase was due to an electrical accident at SLAC in the Fall of 2004 that shut down the lab for half a year.

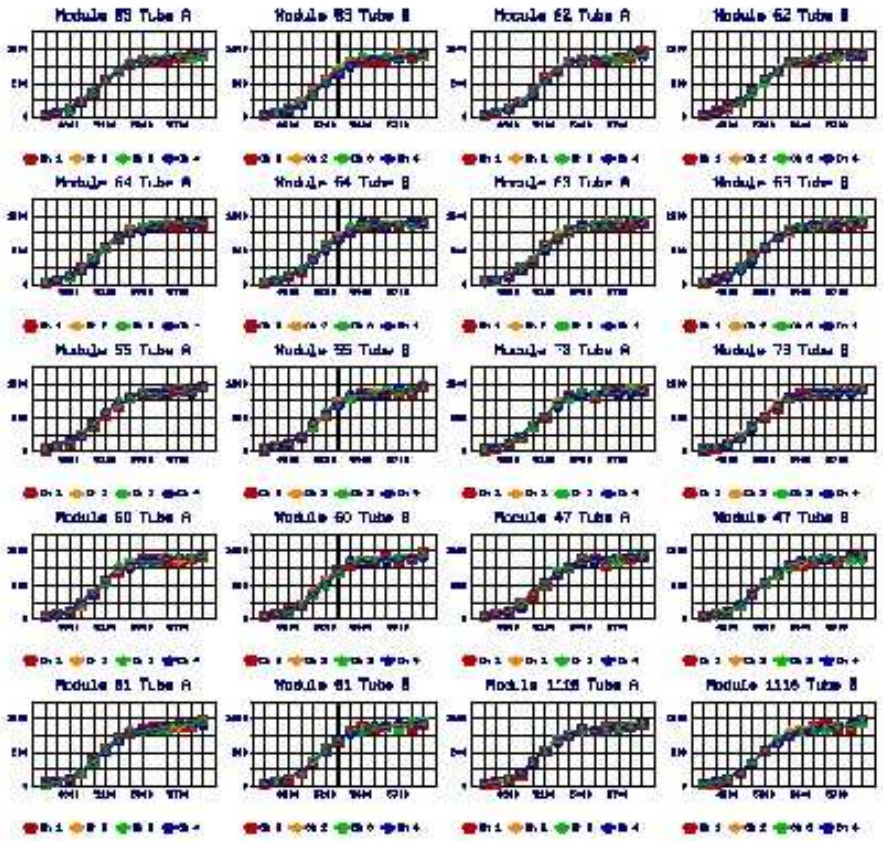

Figure 3.25: Singles' rate plateaus from a sample of installed LSTs.

more than 1200 installed in the detector. It also necessitated the design and fabrication of custom read-out electronics (done by INFN Ferrara in Italy), HV power supplies (The Ohio State University), and gas system (SLAC). The project was completed successfully, safely, and ahead of schedule. After installation, the tubes have performed extremely well since 2005 in two sextants and since the beginning of 2007 in all sextants, with failures rates below 0.5% for both the tubes and z-strips. The efficiencies of all layers are at the geometrically expected level of 90%. Regular testing of singles' rates with cosmic rays has verified continuing excellent behavior with long singles'-rate plateaus (Fig. 3.25). Figure 3.26 shows muon tracks in the LST part of the IFR, while Fig. 3.27 shows the efficiency maps for a sample layer and the improved muon ID of the new and fully functional muon system.

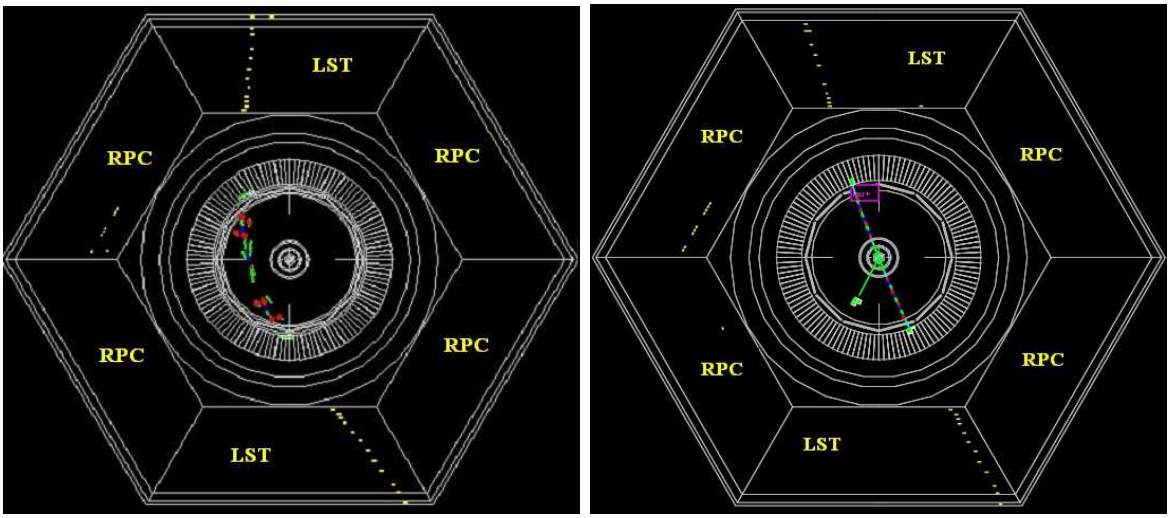

Figure 3.26: Cosmic-ray muon (left) and an $e^+e^- \to \mu^+\mu^-$ muon pair from a beam collision (right) passing through the two sextants that were retrofitted with LSTs in 2004.

3.3.6 Trigger, Data Acquisition and Reconstruction

Data relevant for B physics is selected for storage from the flow of collision information collected by the detector by a two-level trigger system. The Level 1 (L1) trigger is hardware-based, consisting of several dedicated microprocessor systems that analyze data from the front-end electronics (FEEs) of the DCH, EMC, and IFR to form primitive physics objects used to make the trigger decision. These include tracks of minimum transverse momentum that penetrate to a particular depth into the DCH and energy clusters in the EMC above set thresholds. The selections are optimized to maintain nearly perfect $B\overline{B}$ efficiency while removing most of the beam-induced backgrounds in the process of reducing the data collection rate from about 20kHz to a few kHz, which can be processed by the next trigger level. Some "prescaled" events of random beam-beam crossings and special event types are also collected for efficiency, diagnostic, and background studies. The trigger decision is made and communicated within the 12.8 μs buffer limit of the FEEs. The L1 trigger has greater than 99.5% efficiency for $B\overline{B}$ processes.

After an L1 accept decision, the L1 output is passed on to the Level 3 (L3) trigger,

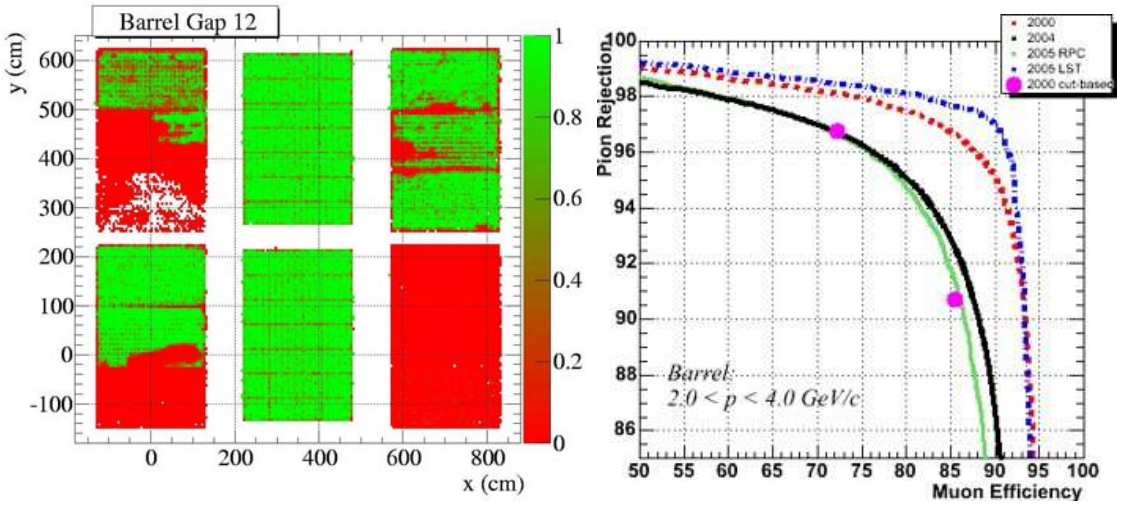

Figure 3.27: Color-coded efficiency maps (left) for a sample layer, showing the difference between RPC sextants in the left and right columns and the LST sextants in the middle column. The scale goes from 0% (red) to 100% (green). The muon ID performance of the LSTs is better than even the initial performance of the RPCs (right).

which consists of software-based algorithms run on a farm of commercial PCs.[15] The L3 trigger also has access to the complete event data and refines the L1 decision with more sophisticated selections, such as requirements on a track's distance of closest approach to the interaction point or the total invariant mass of an event. It maintains the $B\overline{B}$ selection efficiency at more than 99% while reducing the data rate to about 200 Hz. Each event corresponds to about 30 kB of detector information.

An event that results in an L3 accept decision is processed by the data-acquisition electronics and event-building software. In this process, charged tracks are reconstructed from DCH and SVT information and extrapolated to the outer part of the detector, incorporating knowledge of the distribution of material in the detector and the magnetic field. The momentum of tracks is measured from the sagitta in the curves of the tracks.[16] PID is refined with DIRC, EMC, and IFR information as well

[15]The numbering scheme is historical and based on trigger systems with two-hardware based levels and a third, software-based level, as commonly implemented in hadron colliders. *BABAR* requires only one hardware-based level, but the first software-based level maintains the tertiary designation.

[16]Charged particles are deflected by the magnetic field of the solenoid and propagate in helices around the magnetic field lines with the radius of curvature $R \sim p/B$, where p is the momentum of the particle and B is the magnetic field. The orientation of the bending depends on the charge of

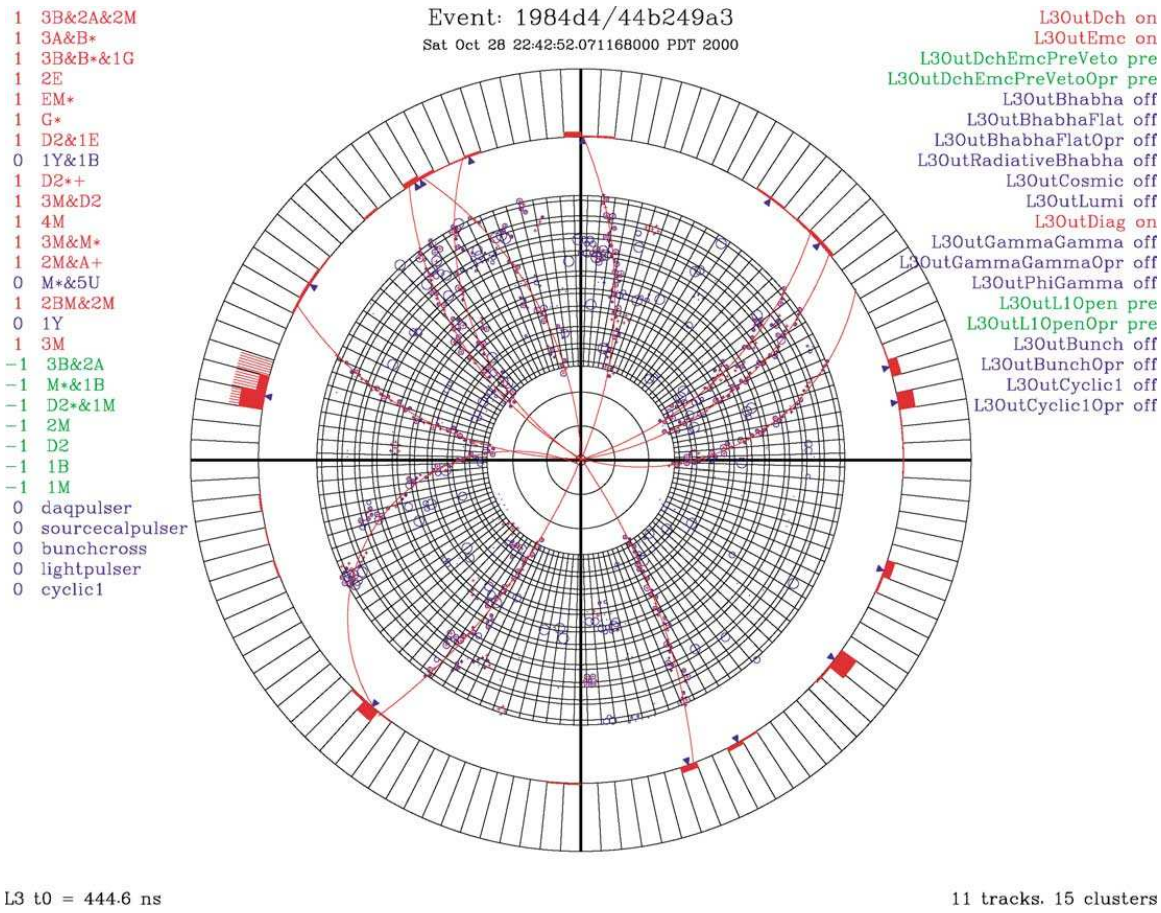

Figure 3.28: Online event display for an event passing the Level 3 trigger, showing wire hits in the DCH (circles and crosses in the inner rings), reconstructed tracks (red curves), and energy deposits in the EMC (red bars in the outer ring, with the height of the bar being proportional to the energy deposited and a full bar being equal to 2 GeV).

as with attempts to match objects in those sub-detectors with tracks in the DCH. Fundamental physical objects reconstructed in the detector are also used to assemble candidates for composite particles, such as π^0's from two photon candidates and K^0_S's from two charged track candidates (from the $K^0_S \to \pi^+\pi^-$ process). Lists of particle candidates as well as the original digitized data is stored on tape in collections that are retrieved later for high-level analysis by individual groups of users.

Throughout event reconstruction various calibrations such as alignment constants and energy-scale adjustments in the EMC are applied to detector information to

the particle.

refine reconstruction performance. Calibration information is updated frequently during data taking to keep it consistent with running conditions. Data-quality scripts monitor detector behavior and various physics processes to verify that the collected data is not compromised by deviations from expected behavior of the detector or accelerator. A parallel system based on the EPICS slow-control environment is used to monitor and control the detector elements for all subsystems. Detector, accelerator, and environmental conditions are recorded in another "ambient" database. The entire data-taking process is supervised at all times by at least two *BABAR* shifters on the detector side and several accelerator operators on the PEP-II side. A typical event display for an event selected by the L3 trigger is shown in Fig. 3.28.

3.3.7 Simulation of Detector Performance

In order to develop analysis methodology, detailed expectations of the detector response to the physical processes of interest are obtained by studying large datasets of Monte Carlo (MC) simulated events. For a given physical process, the MC generators EvtGen [37] and JetSet [38] are used to simulate events with random sampling from distributions of momenta, positions, and decays of the involved particles according to appropriate physical models. The detector response to the generated event is then simulated using the GEANT algorithm [39], which uses a detailed software model of the detector. The resulting detector output is then propagated through the entire reconstruction chain and stored in the database as if it were a real collision event. Stored collections of such events provide an approximate description of what a given process will look like in the detector so that analytical methods can be tuned and tested.

Chapter 4

Analysis of $B^0 \to K^0\overline{K}^0$

4.1 Overview

As the $B^0 \to K^0\overline{K}^0$ decay has a branching fraction at the 10^{-6} level, analyzing its properties is challenging. Out of the millions of $B\overline{B}$ decays and about a billion $e^+e^- \to q\overline{q}$ "continuum" events present in the *BABAR* dataset, we expect to find a few tens of $B^0 \to K^0\overline{K}^0$ decays, taking into account typical reconstruction efficiencies. Thus, we need to be able to reject these backgrounds at a level greater than 10^5 in order to be able to find the signal. Analyzing the time-dependent properties of these decays is an additional challenge.

As the B and K mesons are pseudoscalars with spin 0, the $K^0\overline{K}^0$ system proceeds in an S-wave with zero orbital angular momentum. The particle-antiparticle $K^0\overline{K}^0$ system is thus a CP-even eigenstate, as exchanging the two particles through charge conjugation and then inverting space through parity in the CM frame preserves the original system in the absence of orbital angular momentum. As both K^0 and $\overline{K}^0$ can proceed as either the K^0_S or K^0_L mass eigenstate, in principle we can expect to detect the $K^0_SK^0_S$, $K^0_LK^0_L$, and $K^0_SK^0_L$ final states. The final state, however, must also proceed in an S-wave (corresponding to $CP = (-1)^L = (-1)^0 = 1$), and since these three states are CP eigenstates with values of 1, 1, and -1, respectively, only the

first two final states are allowed by CP conservation (which in the kaon system is violated at a negligible level for this analysis). Thus, the final state for this decay is equal parts $K^0_S K^0_S$ and $K^0_L K^0_L$.

The great majority of the long-lived K^0_L's do not decay in the detector and can only be identified through hadronic showers in the EMC and IFR with no kinematic information. Thus, reconstructing a B meson from a final state with only K^0_L's is nearly impossible in general, and certainly impossible in such a rare decay mode. Hence, we limit ourselves to the $K^0_S K^0_S$ final state, reducing the number of detectable signal decays by a factor of two. Moreover, K^0_S's decay roughly 2/3 of the time to $\pi^+\pi^-$ and 1/3 of the time to $\pi^0\pi^0$, and the latter mode improves our sensitivity only negligibly due to systematic effects from π^0 reconstruction. Thus, we only analyze $K^0_S \to \pi^+\pi^-$ decays, decreasing efficiency by an additional factor of roughly $(2/3)^2$. The signature for the $K^0_S K^0_S$ signal is relatively distinct from backgrounds, however, as the final state has two high-energy K^0_S particles ($p_{\rm LAB} \approx 3\,{\rm GeV}/c$), which is not common in other B decays or in $e^+e^- \to q\overline{q}$ events. In fact, other B decays are a completely negligible background in this analysis.

4.1.1 Analysis Strategy

The analysis exploits kinematic and topological information to separate the signal from the backgrounds. The main background is continuum events, which tend to produce two collimated jets of particles from the hadronization of the two quarks. The two jets are roughly collinear in the CM frame, conserving momentum in the two-body process. In contrast, B decays are roughly isotropic in the CM frame, as the B mesons are produced almost at rest in the threshold $\Upsilon(4S)$ decay without a preferred direction. Thus, several variables describing the shape of the event have different distributions for signal and continuum events and are used to suppress this background. Kinematic variables that describe the reconstructed B meson distinguish it further from continuum events, which have no analogous bound-state structure.

The analysis is performed in a "blind" manner, wherein the data are not examined in the ranges of the variables where the signal is likely to be found until the analysis procedure is finalized. Studies of the signal region are performed on simulated MC samples of $B^0 \to K^0\overline{K}^0$ events, while signal-free regions of the data are used to study the backgrounds wherever possible.

The analysis is performed in several stages. The *BABAR* dataset is first searched for events with the $K^0_S K^0_S$ ($K^0_S \to \pi^+\pi^-$) final state. Then, a B-meson candidate is reconstructed from the final state with an algorithm that constructs the B decay vertex and computes the kinematic, event-shape, and time-dependent variables of the decay. The K^0_S mesons are relatively long-lived and are undetected until they decay several centimeters (on average) away from the B-decay vertex. As there are thus no prompt charged tracks pointing to this vertex, a technique that utilizes knowledge of the interaction point is used to determine the vertex location. The dataset is then reduced through a series of loose selections on kinematic and event-shape variables, which accomplishes the bulk of the background rejection and discards poorly reconstructed signal decays. The signal in the resulting sample of candidate decays is then analyzed using an unbinned extended maximum-likelihood fit to the distributions of the variables in order to extract the branching fraction and the time-dependent CP-violating parameters.

4.1.2 The Maximum-Likelihood Fit

Using a maximum-likelihood fit is a more powerful alternative to the simpler "cut-and-count" method. In the latter technique, strict selections are made on the discriminating variables to exploit the difference in distributions for signal and background. The selections are tuned to maximize the statistical significance of a detected signal, which is a trade-off between keeping as much signal as possible (high signal efficiency) and rejecting as much background as possible. The efficiency of the selection for signal decays is determined from simulated Monte-Carlo samples that predict what the

signal decay would look like in the detector. Similarly, the expected number of background events after the selections is predicted using MC studies and data in regions where no signal is present (such as the off-resonance data mentioned in the previous chapter.) The number of signal decays in the data sample after the selections is then computed as an excess over the background expectation, up to Poissonian counting uncertainties.

In the maximum-likelihood fit, we instead impose loose selections that preserve a larger sample of candidates where the shape of the distributions of the variables can be fitted. For each variable x_i we construct a probability density function (PDF) $P(x;\mathbf{q})$ that describes how the variable is distributed for a particular category of events (signal or background). $\mathbf{q}$ is a set of parameters that describe the shape of the distribution for a given functional form and includes physical quantities such as time-dependent CP asymmetries. These parameters are either fixed to predetermined values or determined by the fit itself. Assuming m uncorrelated variables, the total PDF for a given category of decay is simply the product of the m individual PDFs:

$$P(\mathbf{q}) = \prod_{i=0}^{m} P(x;\mathbf{q}). \tag{4.1}$$

A likelihood function for a given event j in the fitted sample is formed from the PDFs P^j for each possible category, evaluated at the values of the variables for this event:

$$\mathcal{L}_j = N_{\rm sig} P^j_{\rm sig}(\mathbf{q}) + N_{\rm bkg} P^j_{\rm bkg}(\mathbf{q}), \tag{4.2}$$

where $N_{\rm sig}$ and $N_{\rm bkg}$ are the number of events in the signal and background categories, respectively (the event "yields"). The total likelihood for the sample is formed from a product of the likelihoods for each event and a prefactor that accounts for the Poissonian behavior of the event yields relative to the total number of events in the

sample:

$$\mathcal{L} = \frac{e^{-N_{tot}}}{N!} \prod_{j=0}^{N} \left(N_{\rm sig} P^j_{\rm sig}(\mathbf{q}) + N_{\rm bkg} P^j_{\rm bkg}(\mathbf{q}) \right), \tag{4.3}$$

where $N_{\rm tot} = N_{\rm sig} + N_{\rm bkg}$.[1]

The fit consists of maximizing this function with respect to the event yields and the "floated" (not fixed) parameters in $\mathbf{q}$. The values at the maximum of $\mathcal{L}$ are a statistically optimized estimate of the true values of the parameters.[2] The uncertainties of the floating parameters in the fit are determined from the covariance matrix given by

$$C_{ij} = \frac{\partial^2(\ln\mathcal{L})}{\partial x_i x_j}, \tag{4.4}$$

where x_i is the i'th floated parameter in the fit. The fit is performed by the `Minuit` package, which also computes unequal positive and negative uncertainties if the likelihood has an asymmetrical shape around the fit minimum.

This technique uses the information about the entire shape of the distributions of the discriminating variables, rather than just the integral of the PDF within the chosen selection, as is the case in cut-and-count analyses. In effect, the maximum-likelihood fit performs a cut-and-count analysis at each value of a variable, using the difference in the expected probability of finding a signal versus a background event at that value. (The "unbinned" nature of this fit means that this is done functionally, using functional PDFs, rather than histogrammatically, where the PDFs would be binned histograms.) Thus, it is a statistically more powerful procedure and obtains more precise results (statistically) than either a cut-and-count or binned maximum-likelihood analysis. The complicated nature of the fit requires extensive validation, while imperfect modeling of the PDFs and of the correlations between the variables increases the systematic uncertainties. However, for analyses where

[1] The Poissonian factor effectively constrains the sum of the event yields to be equal to the number of events in the sample.

[2] In practice the fit is performed through iterative computational algorithms, rather than analytically, so for computational tractability the negative logarithm of the likelihood is *minimized* instead, which is analytically equivalent.

dominant uncertainties are statistical rather than systematic, this is a good trade-off. In particular, this technique is well suited for rare decays, such as the ones described in this thesis.

4.1.3 Time-Dependent Measurement

As was mentioned in the previous chapter, the difference in decay times Δt of the two B mesons in an $\Upsilon(4S)$ decay can be used to extract CP-violating parameters [40]. Δt is extracted from the distance along the z direction in the lab frame between the decay vertices of the two B's in the event: $\Delta t = \Delta z/\beta\gamma c$, where c is the speed of light, and $\beta\gamma$ is the boost of the $\Upsilon(4S)$ system relative to the lab frame. In this entangled $B\overline{B}$ environment, the time-dependent decay rates are a slight modification of Eq. 2.29:

$$\begin{aligned} f_{B^0_{\rm tag}}(\Delta t) &= \frac{e^{-|\Delta t|/\tau}}{4\tau}[1 + S\sin(\Delta m_d \Delta t) - C\cos(\Delta m_d \Delta t)], \\ f_{\overline{B}^0_{\rm tag}}(\Delta t) &= \frac{e^{-|\Delta t|/\tau}}{4\tau}[1 - S\sin(\Delta m_d \Delta t) + C\cos(\Delta m_d \Delta t)] \end{aligned} \tag{4.5}$$

for decays where the other B in the event, $B_{\rm tag}$, is identified as a B^0 and $\overline{B}^0$, respectively. τ and Δm_d are the B^0 lifetime and $B^0 - \overline{B}^0$ mixing frequency, respectively. S and C were defined in Ch. 2, and are determined from the maximum-likelihood fit as parameters of the Δt PDF for signal decays.

4.1.4 The Discriminating Variables

Kinematic Variables

The fit uses two kinematic variables, $m_{\rm ES}$ and ΔE. Both variables exploit the two-body nature of the $e^+e^- \to \Upsilon(4S) \to B\overline{B}$ decay, where by four-momentum conservation each B meson has the same energy as the beam in the e^+e^- CM frame: $E^*_B = E^*_{\rm beam}$, where the asterisk denotes a variable evaluated in the CM frame. Thus,

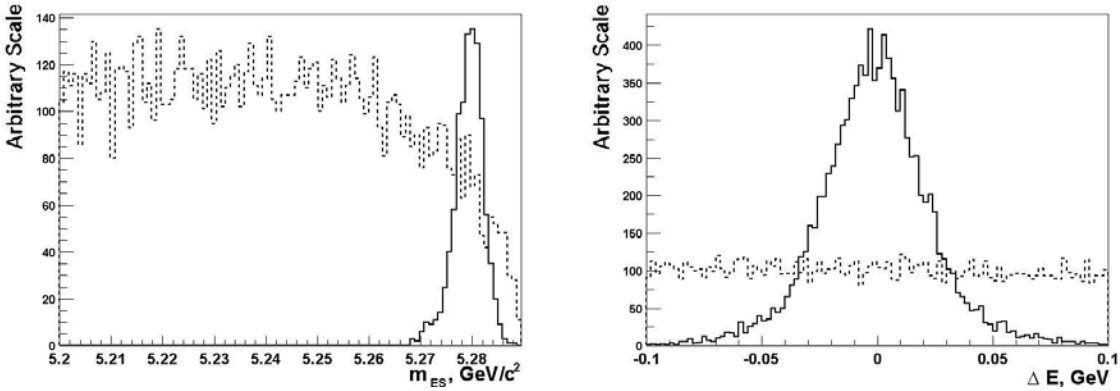

Figure 4.1: Typical distributions of $m_{\rm ES}$ (left) and ΔE (right) for $B\overline{B}$ (solid) and continuum (dotted) events.

the energy difference,

$$\Delta E = E_B^* - E_{\rm beam}^*, \tag{4.6}$$

has a distribution centered near zero GeV for B decays,[3] while the distribution for continuum events should have a smooth phase-space shape and should not exhibit any peaking structure (Fig. 4.1). The resolution is dominated by the uncertainty in the measurement of track momenta and varies across different decay modes, ranging from 20 MeV to 40 MeV.

The corresponding invariant mass

$$m_{\rm ES} = \sqrt{E_{\rm beam}^{*2} - \mathbf{p}_B^{*2}}, \tag{4.7}$$

has a distribution centered at $m_{\rm ES} = 5.28\,{\rm GeV}/c^2$ (near the B mass) for B decays, and a smooth threshold shape for continuum decays with a high cutoff at $m_{\rm ES} = 5.29\,{\rm GeV}/c^2$ (the beam energy), corresponding to $\mathbf{p}_B^* = 0$ (Fig. 4.1). The resolution for $B\overline{B}$ decays is dominated by the beam-energy spread. As the beam energy is known much more precisely (at the 2 MeV level) than the measured B energy, this substitution improves the B mass resolution by a factor of ten. $m_{\rm ES}$ is of course a

[3]Detector effects and uncertainties in the reporting of beam energies lead to small deviations from zero.

Lorentz-invariant variable, and it can be expressed in the lab frame as

$$m_{ES} = \sqrt{(s/2 + \mathbf{p_0} \cdot \mathbf{p_B})^2/E_0^2 - p_B^2}, \tag{4.8}$$

where $(E_0, \mathbf{p_0})$ is the four-momentum of the e^+e^- system in the lab frame and $\sqrt{s}/2 = E^*_{\rm beam}$. This definition is used to compute $m_{\rm ES}$ in practice, as the B momentum is measured in the lab frame and transforming it to the CM frame would require knowledge of the masses of the B daughters, which would in turn require PID assumptions.

Event-shape Variables

Four event-shape variables are used: sphericity, sphericity angle, R_2, and a Fisher discriminant constructed from Legendre moments of momentum flow. Sphericity is a measure of how isotropic the shape of the event is [41]. It is formed from the sphericity tensor

$$S^{\alpha\beta} = \frac{\sum_i p_i^\alpha p_i^\beta}{\sum_i \mathbf{p}_i^2}, \tag{4.9}$$

where $\mathbf{p}_i$ is the momentum of particle i in the event, α and β range over the x, y, and z components of the particle's momentum, and the sum is over all particles in the event. The sphericity is then defined as

$$S = \frac{3}{2}(\lambda_2 + \lambda_3), \tag{4.10}$$

where λ_2 and λ_3 are the two largest eigenvalues of the sphericity tensor. The direction of the eigenvector corresponding to the largest eigenvalue is called the sphericity axis of the event. Sphericity is defined to range from 0 to 1, corresponding to the most directional and the most isotropic events, respectively. In effect, it characterizes the degree of randomness in the orientation of the momenta of the particles in the event with respect to the sphericity axis.

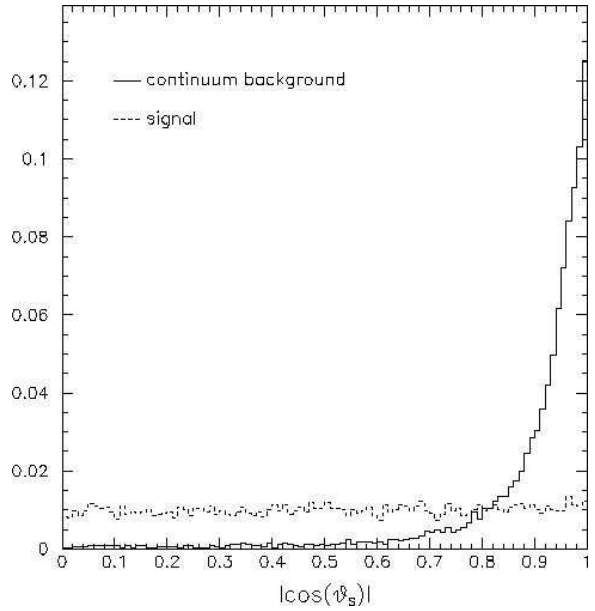

Figure 4.2: Typical distributions of $|\cos\theta_S|$ for $B\overline{B}$ (dashed) and continuum (solid) events.

We can also determine the sphericity axes separately for the two B candidates in the event. The angle between the two axes is then called the sphericity angle, θ_S. For true $B\overline{B}$ events, $|\cos\theta_S|$ has a flat distribution, as the two isotropically decaying mesons have little directional correlation with each other. Two-jet events, on the other hand, have a distribution peaking at 1, displaying the collinear event shape of continuum processes (Fig. 4.2).

R_2 is a ratio formed from the Fox-Wolfram moments, H_l, defined as [42]

$$H_l = \sum_{i,j} \frac{|\mathbf{p}_i| \cdot |\mathbf{p}_j|}{E_{\rm vis}^2} P_l(\cos\theta_{ij}), \tag{4.11}$$

where P_l are the Legendre polynomials of order l, $\mathbf{p}_{i,j}$ are the momenta of particles i and j, θ_{ij} is the opening angle between the momentum vectors of the two particles, and $E_{\rm vis}^2$ is the total visible energy of the event. R_2 is defined as H_2/H_0. Assuming perfect reconstruction, the zeroth moment is equal to 1 by energy and momentum conservation and thus serves as a normalization in the ratio. For two-jet events, the odd-numbered moments are approximately zero, while the even moments peak at 1,

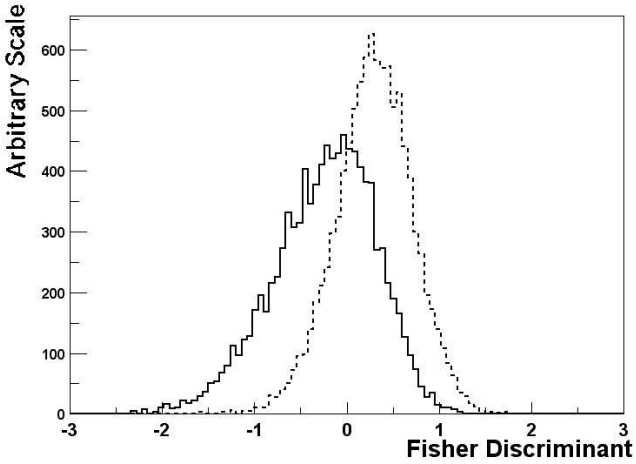

Figure 4.3: Typical distributions of the two-body Fisher discriminant for $B\overline{B}$ (solid) and continuum (dotted) events.

allowing continuum suppression through an upper cut on R_2.

The last topological variable is the Fisher discriminant [43], defined as

$$\mathcal{F} = \sum_i \alpha_i x_i, \tag{4.12}$$

where x_i are discriminating variables and α_i are coefficients optimized for the best possible separation of signal from background. Two such variables are used here, defined as

$$\begin{aligned} x_0 &= \sum_i p_j, \\ x_2 &= \sum_i p_j |\cos\theta_j|^2, \end{aligned} \tag{4.13}$$

where the sum is over all particles in the event that are not part of the reconstructed B candidate, p_j is the momentum of particle j in this set of particles, and θ_j is the angle between the momentum vector of the particle and the thrust axis of the particles composing the reconstructed B candidate.[4] These variables describe the

[4]The thrust axis of a system of particles is the direction of the unit vector $\mathbf{n}$ that maximizes $\sum_i |\mathbf{n}\cdot\mathbf{p}_i| / \sum_i |\mathbf{p}_i|$. The axis is a means of defining an overall directional orientation of the system.

momentum flow of the particles in the rest of the event relative to the decay axis of the B candidate. Using simulated samples of signal and background, the Fisher coefficients used in this analysis were optimized for B decays to two-body final states containing only kaons and pions [44]. The final Fisher discriminant is

$$\mathcal{F} = 0.5139 - 0.6023x_0 + 1.2698x_2, \tag{4.14}$$

where the constant term was chosen so that the distribution for signal decays is centered at approximately zero. Figure 4.3 illustrates the typical signal-background separation of this variable.

4.2 Data set

This analysis is performed on a dataset collected by *BABAR* in Runs 1-5 from 1999 to the Summer of 2006. This corresponds to $316\,\text{fb}^{-1}$ of e^+e^- collision data at the $\Upsilon(4S)$ resonance, which include 347 million $B\overline{B}$ pairs. In addition, $134,000$ simulated $B^0 \to K^0\overline{K}^0$ events were used for MC studies.

4.3 Reconstruction and Selection

4.3.1 K^0_S Selection

K^0_S candidates are reconstructed from pairs of oppositely charged tracks originating from a common decay point, as determined by a vertexing algorithm. The invariant mass of the pair is required to lie within $11.2\,\text{MeV}/c^2$ of the nominal K^0_S mass, $0.4976\,\text{GeV}/c^2$, as provided by the Particle Data Group (PDG) [20]. This selection corresponds to roughly 2.5 times the resolution of the reconstructed mass peak. As shown in Fig. 4.4, the selection retains almost all real K^0_S's and a small background underneath the peak, which consists of random combinations of pions and kaons that

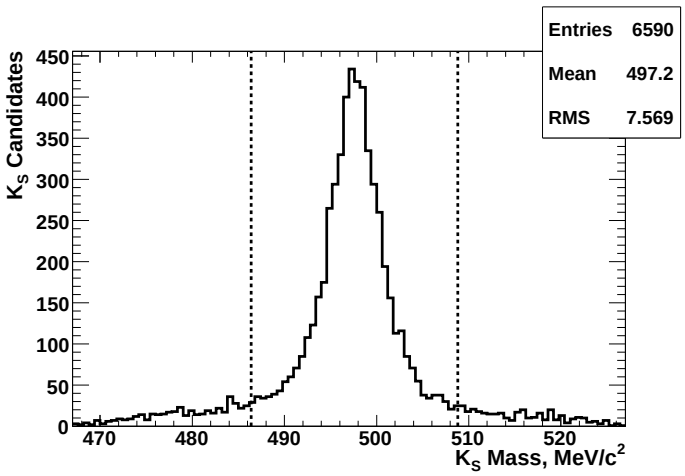

Figure 4.4: Distribution of the invariant mass of the reconstructed K_S^0 candidates after all other selection requirements. The dashed vertical lines indicate the imposed selection on the invariant mass itself.

happen to originate from the same location and to fall in this invariant-mass range. The spatial resolution on the vertex location is approximately 100 μm. An additional requirement on the K_S^0 candidate is that the decay time of the K_S^0 divided by its error be greater than 5. This requirement on the decay-time significance is computed from the distance between the decay point and the interaction point along the line of flight of the candidate. It is imposed to reject poorly reconstructed K_S^0's, where an inadequately determined decay vertex results in a large uncertainty on the measured decay time.

4.3.2 B Reconstruction and Vertexing

Signal B candidates are reconstructed from pairs of K_S^0 candidates satisfying the above requirements. The position of the B decay vertex has to be computed since it is needed for the time-dependent measurement. As the K_S^0 mesons have the relatively long lifetime of 90 ps, their decay vertices are separated from the B decay vertex by a few centimeters on average. This complicates the measurement since the neutral K_S^0's are undetected in the tracker until they decay, so there are no prompt charged tracks originating from the B decay vertex in this mode.

To perform the measurement, we used a method previously employed in other K^0_S analyses without prompt charged tracks, wherein the B meson is constrained in the vertex fit to decay within the interaction point in the plane transverse to the beam direction [45].[5] In effect, the z position of the vertex is determined from the intersection in the $x-y$ plane of the K^0_S line of flight with the interaction point. The interaction point is very precisely known from the location of the two crossing beams, as provided by PEP-II diagnostic measurements for each crossing ($\sigma_x \approx 110\,\mu$m, $\sigma_y \approx 3.3\,\mu$m). This method exploits the threshold nature of the $\Upsilon(4S) \to B\overline{B}$ decay, where the B mesons are almost at rest in the CM frame and therefore have negligible displacement in the lab frame in the non-boosted transverse direction. Thus, the assumption that the decay vertex is located within the beamspot in the transverse plane introduces negligible biases.

The z position of the vertex of the $B_{\rm tag}$ candidate is then determined from the remaining tracks in the event, with the requirement that the vertex be located within the beamspot in the transverse plane (like the signal B candidate) and that the $B_{\rm tag}$ energy be equal to the beam energy in the CM frame. (These two requirements, which must be true in the underlying physical event, improve the resolution of the z measurement.) The $\Upsilon(4S) \to B_{\rm rec}B_{\rm tag}$ decay vertex is then computed, constraining the sum of the decay times of the two B's to be equal to twice the B lifetime τ with an uncertainty of $\sqrt{2}\tau$. The constraint is meant to partially correct the decay vertices for the small transverse displacement of the B's, which improves the Δz resolution. With this method, the resolution of the z position of the signal B vertex is still better than the resolution on the vertex position of $B_{\rm tag}$, yielding a Δt precision (approximately 0.9 ps) comparable to that in modes where the signal B has prompt charged tracks in the final state (where the beamspot constraint on the signal B candidate is not required).

Only K^0_S mesons that decay within the volume of the SVT are suitable for the

[5] This technique was developed at *BABAR*.

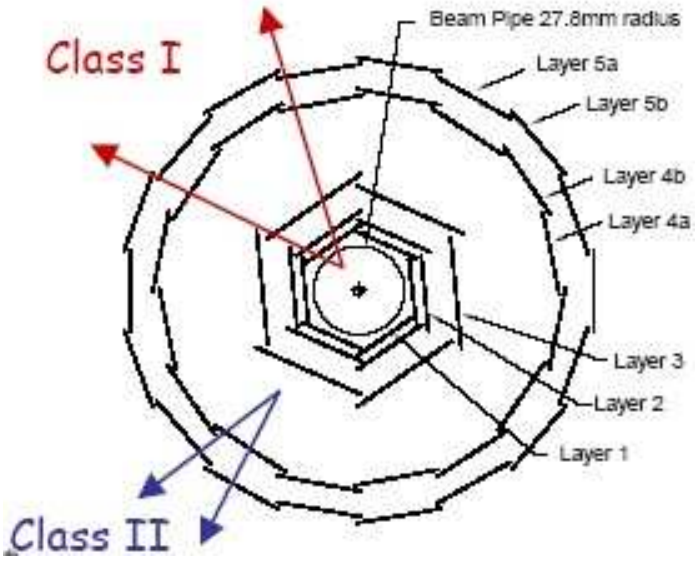

Figure 4.5: Schematic view of Class I and Class II K_S^0 decays.

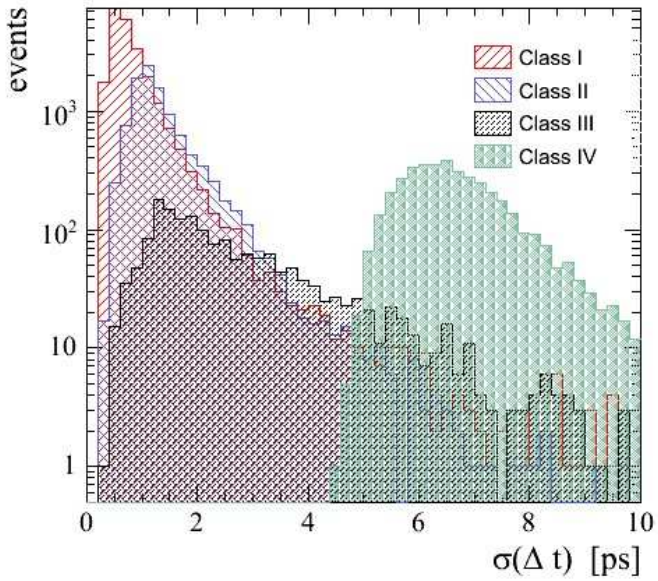

Figure 4.6: Distribution of the uncertainty on Δt separated according to vertex quality of the better vertexed K_S^0 in the signal B, as evaluated on simulated $B^0 \to K^0\overline{K}^0$ events. Only Class I and Class II B candidates are used for the time-dependent measurement.

time-dependent measurement, as the DCH alone does not provide sufficiently accurate vertexing. Thus, we classify K_S^0 candidates into three mutually exclusive categories depending on the SVT information available for the two π daughters (Fig. 4.5):

- Class I – each daughter pion has at least one z-hit and at least one ϕ-hit in the inner three layers of the SVT;
- Class II – not in Class I, each daughter pion has at least one z-hit and at least one ϕ-hit in the SVT;
- Class III – not in Class I or Class II, there is at least one hit in the SVT;
- Class IV – no SVT information.

Class I and Class II K_S^0's are suitable for the time-dependent measurement, corresponding to roughly 60% of K_S^0's . However, only one such K_S^0 meson is needed to employ this method: the other K_S^0 must originate from the same vertex and including it within the beamspot constraint only negligibly improves the measurement. Thus, we classify B candidates into "CP-Good" and "CP-Bad" categories according to the better vertexed K_S^0:

- Good:
  - at least one of the K_S^0's is Class I or Class II;
  - $\Delta t < 20\,\text{ps}$;
  - $\sigma_{\Delta t} < 2.5\,\text{ps}$;
- Bad:
  - all other candidates.

The requirements on Δt and its uncertainty in the first category further refine the quality of the vertex information.

Only CP-Good candidates are used to determine the time-dependent CP parameter S. However, all candidates are used to determine the signal and background yields (where vertexing information is not needed) and, if flavor information on B_{tag} is available, the CP parameter C, as described later. Since only one out of the two

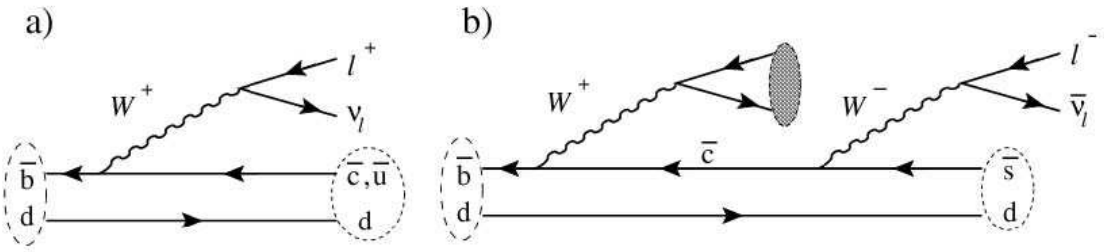

Figure 4.7: Feynman diagrams of semileptonic neutral-B decays with a right-sign primary lepton (a) and a wrong-sign secondary lepton (b).

K_S^0's must be Class I or II, the fraction of signal B decays suitable for the time-dependent measurement increases to 82%. Figure 4.6 shows the typical distribution of $\sigma_{\Delta t}$ in simulated signal decays, separated according to the quality of the K_S^0-vertex information.

4.3.3 Flavor Tagging

As was discussed in Ch. 3, the measurement of time-dependent CP asymmetries in final states to which both B^0 and $\overline{B}^0$ can decay is only possible if the flavor of $B_{\rm tag}$ can be determined at the time of its decay, which in turn identifies the opposite flavor of the reconstructed B at that time. Although $B_{\rm tag}$ is vertexed from the tracks in the rest of the event, its decay mode is not fully reconstructed. Nevertheless, kinematic and PID information can be used to select classes of decays where the charge of some of the daughters are highly correlated with the flavor of the mother B. For example, in semileptonic $b \to c$ decays, such as $B \to Dl\nu_l$ ($l = e,\ \mu$), a positively charged lepton could only come from a B^0 and a negatively charged lepton only from a $\overline{B}^0$ (Fig. 4.7a). These primary, "right-sign" leptons have high momentum whose direction is closely correlated to the missing-momentum direction from the undetected neutrino. This signature makes these leptons easy to separate from secondary leptons from $b \to c \to s$ decays, which originate from a semileptonic decay of the daughter D meson and whose charge has the opposite correlation with the flavor of the B ("wrong-sign" leptons, Fig. 4.7b). Thus, a high-momentum lepton tag has a high

probability of tagging the B flavor correctly. The trade-off is that such semileptonic decays have a low efficiency of being identified, thus accounting for a small fraction of flavor-tagged events.

A more efficient flavor-tag is the charge of a kaon from $b \to c \to s$ decays, determined by identifying a track as a kaon with information from the DIRC. These kaons have the same charge-flavor correlation as the primary leptons. Although plentiful, they suffer from a background of wrong-sign kaons from many other processes. Thus, the higher efficiency is counteracted by a higher probability of misidentifying the $B_{\rm tag}$ flavor. Another tag is the charge of slow pions from $D^* \to D\pi$ decays, which have the opposite correlation to lepton and kaon tags. Background to these slow pions can be reduced as their direction is highly correlated with the direction of the D in the lab frame, since in the D^* rest frame the two daughters are produced almost at rest due to the small mass difference between the D^* and the D. Other high-momentum charged particles can also be used for tagging.

Information from the aforementioned tags is used by a multivariate neural-network algorithm to assign events to six mutually exclusive tagging categories [46]. A category is characterized by a tagging efficiency ϵ, indicating the fraction of events belonging to this category, and mistag fraction w, or fraction of events in this category with a misidentified $B_{\rm tag}$ flavor. About 25% of events are assigned to a seventh, "untagged" category where no flavor determination is made due to insufficient tagging information. These events cannot be used for the measurement of either of the CP parameters, S or C.

The efficiencies and mistag fractions are evaluated on a high-purity sample, $B_{\rm flav}$, of fully reconstructed B decays to $D^{(*)-}(\pi^+,\ \rho^+,\ a_1^+)$ final states. These decays are "self-tagged", since the charges of the daughters uniquely identify the flavor of the parent B, allowing a highly accurate determination of the tagging performance on the other B in the event. As the tagging of $B_{\rm tag}$ is independent of the decay mode of $B_{\rm rec}$, we use the results from the $B_{\rm flav}$ sample in this analysis. The error on the

Tagging Category	ϵ, %	w, %
Lepton	8.7 ± 0.1	2.90 ± 0.36
Kaon1	11.0 ± 0.1	5.24 ± 0.42
Kaon2	17.2 ± 0.1	14.99 ± 0.42
KaonPion	13.8 ± 0.1	23.35 ± 0.53
Pions	14.3 ± 0.1	32.66 ± 0.55
Other	9.6 ± 0.1	41.88 ± 0.68

Table 4.1: The six tagging categories and their efficiencies ϵ and mistag fractions w.

S asymmetry parameter goes as $1/\sqrt{Q}$, where $Q = \sum_k \epsilon_k (1 - 2w_k)^2$ is summed over the six tagging categories. In the B_{flav} sample, $Q = (30.4 \pm 0.3)\%$, indicating that effectively only about a third of the tagged decays contribute to the measurement of S and C. Table 4.3.3 lists the six categories and their efficiencies and mistag fractions.

4.3.4 Background Suppression

The following selections are imposed to reject backgrounds:

- At least three charged tracks must be found in the event;
- $R_2 < 0.95$ and sphericity > 0.01;
- $|\cos\theta_S| < 0.8$;
- $5.2 < m_{\text{ES}} < 5.2895\,\text{GeV}/c^2$;
- $|\Delta E| < 0.1\,\text{GeV}$.

The first three requirements accomplish the bulk of continuum rejection. As the last two variables are used in the maximum-likelihood fit, the corresponding selections are quite loose and do not reject large signal-free "sidebands" needed in the fit to estimate the background levels underneath the peaking signal. These two selections are thus almost 100% efficient on signal decays. We define the m_{ES} sideband as $5.2 < m_{\text{ES}} < 5.26\,\text{GeV}/c^2$. The signal peaks at $m_{\text{ES}} = 5.28\,\text{GeV}/c^2$ with a width less

Selection	Efficiency (%)
Reconstruction, three tracks, R_2, Sphericity	$56.90 \pm 0.14 \pm 0$
$\lvert\cos\theta_S\rvert < 0.8$	$76.70 \pm 0.15 \pm 2.5$
$(M - M_K^0) < 11.2\,\mathrm{MeV}/c^2$	$90.13 \pm 0.12 \pm 0$
Decay-Time Significance > 5	$95.28 \pm 0.09 \pm 0$
$\lvert\Delta E\rvert < 0.10\,\mathrm{GeV}$, $5.2 < m_{\mathrm{ES}} < 5.2895\,\mathrm{GeV}/c^2$	$98.32 \pm 0.06 \pm 0.84$
Nominal Efficiency	$36.85 \pm 0.13 \pm 1.24$
K_S^0 Reconstruction Correction	$0.9800 \pm 0.0097 \pm 0$
K_S^0 Mass-Cut Correction	$0.988 \pm 0 \pm 0.012$
$\mathcal{B}(K^0\overline{K}^0 \to K_S^0 K_S^0)$	50
$\mathcal{B}(K_S^0 \to \pi^+\pi^-)^2$	$(68.95 \pm 0 \pm 0.14)^2$
Total Efficiency	$8.49 \pm 0.09 \pm 0.30$

Table 4.2: Summary of selection efficiencies for signal $B^0 \to K^0\overline{K}^0$ decays, as determined from 134,000 simulated Monte Carlo events. The efficiency on each cut is relative to the previous one and the first error is statistical while the second is systematic.

than $3\,\mathrm{MeV}/c^2$, so essentially all events in this sideband are background events, as $5.26\,\mathrm{GeV}/c^2$ is more than six standard deviations away from the B mass.

Table 4.2 shows the efficiencies of all the selection criteria as evaluated on the simulated signal MC sample. Included are the assumption of 50% for $K^0\overline{K}^0 \to K_S^0 K_S^0$ and the branching fraction for $K_S^0 \to \pi^+\pi^-$, taken from the PDG [20]. The table shows statistical uncertainties on the efficiencies from limited MC statistics and systematic uncertainties due to differences between the MC and data samples, which will be discussed later.

MC studies of $B\overline{B}$ processes showed that the only possible $B\overline{B}$ background could come from the $K^*K_S^0$ mode. The efficiency of this decay in our analysis has been shown to be 10^{-3} smaller than that of $K^0\overline{K}^0$. Hence, it could affect this measurement at the one-event level ($\sim 3\%$) only if its branching fraction is greater than the $K^0\overline{K}^0$ branching fraction by a factor of 10 or more. Although no precise measurements of the $K^*K_S^0$ branching fraction exist, the decay proceeds through similar amplitudes and is affected by the same CKM factors as $K^0\overline{K}^0$. Therefore, the two branching

Table 4.3: Composition of the final candidate sample with respect to vertex quality, tagged flavor, and tagging category.

Tagging	*CP* Good			*CP* Bad			Total		
Category	B^0	$\overline{B}^0$	Total	B^0	$\overline{B}^0$	Total	B^0	$\overline{B}^0$	Total
Lepton	3	7	10	1	0	1	4	7	11
Kaon1	36	31	67	10	12	22	46	43	89
Kaon2	82	80	162	16	16	32	98	96	194
KaonPion	91	87	178	23	15	38	114	102	216
Pions	107	117	224	40	33	73	147	150	297
Other	114	111	225	18	29	47	132	140	272
Tagged	433	433	866	108	105	213	541	538	1079
Untagged			659			166			825
Total			1525			379			1904

fractions should have comparable magnitudes, allowing us to neglect the $K^*K^0_S$ mode in this analysis. Thus, backgrounds from $B\overline{B}$ processes are negligible in this analysis.

4.3.5 Final Sample of Candidates

The final sample after all selection criteria contains 2321 candidates. The breakdown of the sample according to tagging category, flavor of $B_{\rm tag}$, and quality of the time-dependent vertexing is given in Table 4.3. The corresponding information for signal decays as evaluated on the signal MC sample is shown in Table 4.4

4.4 The Fit and PDF Modeling

The unbinned extended maximum likelihood fit is performed for two categories, signal and continuum background, using four variables. The total likelihood for an event is

$$\mathcal{L} = \frac{e^{-N'}}{N!}\prod_{i=1}^{N}\left(N_{\rm sig}\mathcal{P}_{\rm sig} + N_{\rm bkg}\mathcal{P}_{\rm bkg}\right), \tag{4.15}$$

Table 4.4: Composition of the signal MC sample with respect to vertex quality, tagged flavor, and tagging category after all selection criteria have been applied.

Tagging	*CP* Good			*CP* Bad			Total		
Category	B^0	$\overline{B}^0$	Total	B^0	$\overline{B}^0$	Total	B^0	$\overline{B}^0$	Total
Lepton	1908	1934	3842	362	402	764	2270	2336	4606
Kaon1	2141	2156	4297	454	419	873	2595	2575	5170
Kaon2	3425	3392	6817	707	669	1376	4132	4061	8193
KaonPion	2872	2690	5562	608	582	1190	3480	3272	6752
Pions	2804	3047	5851	643	755	1398	3447	3802	7249
Other	1962	2089	4051	443	542	985	2405	2631	5036
Tagged	15112	15308	30420	3217	3369	6586	18329	18677	37006
Untagged			9972			2397			12369
Total			40392			8983			49375

where $N_{\rm sig}$ and $N_{\rm bkg}$ are the signal and background yields and the corresponding PDFs $\mathcal{P}$ are given by

$$\mathcal{P} = \mathcal{P}(m_{\rm ES})\mathcal{P}(\Delta E)\mathcal{P}(\mathcal{F})\mathcal{P}(\Delta t). \tag{4.16}$$

(The variables were defined in Sec. 4.1.4). Four physical parameters are extracted from the fit: $N_{\rm sig}$, $N_{\rm bkg}$, S, and C.

The assumption of uncorrelated variables underlying the PDF product above can be studied using two-dimensional scatter plots of the variables in the signal MC sample and in the background-only $m_{\rm ES}$ sideband (Figs. 4.8-4.19).[6] No correlations are observed, except for a linear 10% $m_{\rm ES}$-ΔE correlation in the signal MC sample, which can also be derived analytically for $B\overline{B}$ decays from the definitions of the two variables. This correlation has been noted in many other analyses in *BABAR* and found not to bias the results of the fit. Nevertheless, any resulting bias would be detected in validation studies of the fit and its effect included as a systematic uncertainty on the results.

As there are very few signal events in the data sample, we parameterize the signal

[6]The figures also show profile histograms, where the error bars on each bin correspond to the RMS of the bin's contents divided by $\sqrt{N}$, where N is the number of points in the bin.

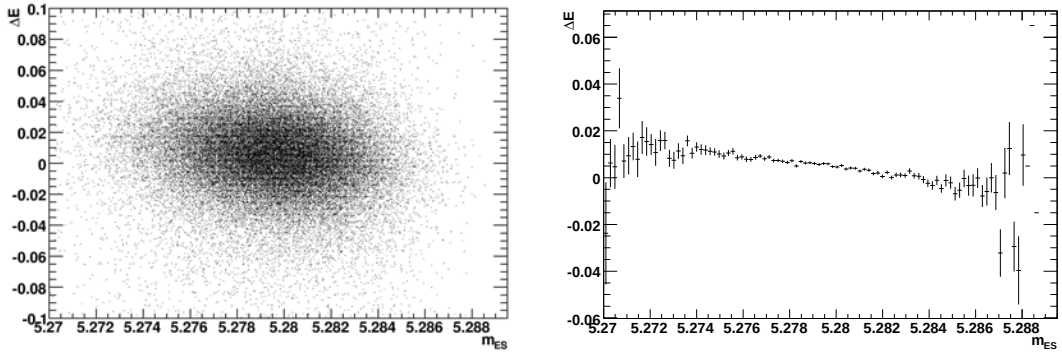

Figure 4.8: Scatter plot (left) of ΔE vs. $m_{\rm ES}$ in signal MC events, and the corresponding profile histogram (right). The error bars in the profile histogram correspond to the error on the mean of the bin.

PDFs using the signal MC sample. Differences between data and MC are considered as sources of systematic uncertainty and estimated using studies of related modes with branching fractions large enough to permit signal studies in data. These modes have similar final-state topologies with one or more K^0_S's and include $B^+ \to K^0\pi^+$, which is analyzed in the next chapter. The studies are described later. The functional forms for the continuum background PDFs are taken from the $m_{\rm ES}$ sideband, but most of the parameters of the PDFs are floated in the final fit to data, eliminating uncertainties due to MC modeling of the background distributions. This is possible since there are enough background events in the fitted sample to characterize the PDFs. I will describe the parameterization of the PDFs for the four variables in turn.

4.4.1 $m_{\rm ES}$

The signal $m_{\rm ES}$ distribution is modeled as a double Gaussian function:

$$\mathcal{P}_{\rm sig}(m_{\rm ES}) = f_{\rm core}e^{-(m_{\rm ES}-\mu_{\rm core})^2/(2\sigma^2_{\rm core})} + (1-f_{\rm core})e^{-(m_{\rm ES}-\mu_{\rm tail})^2/(2\sigma^2_{\rm tail})}, \qquad (4.17)$$

where μ and σ are the mean and variance of a Gaussian, "core" and "tail" refer to the narrower and the wider Gaussian, respectively, and $f_{\rm core}$ is the fractional component

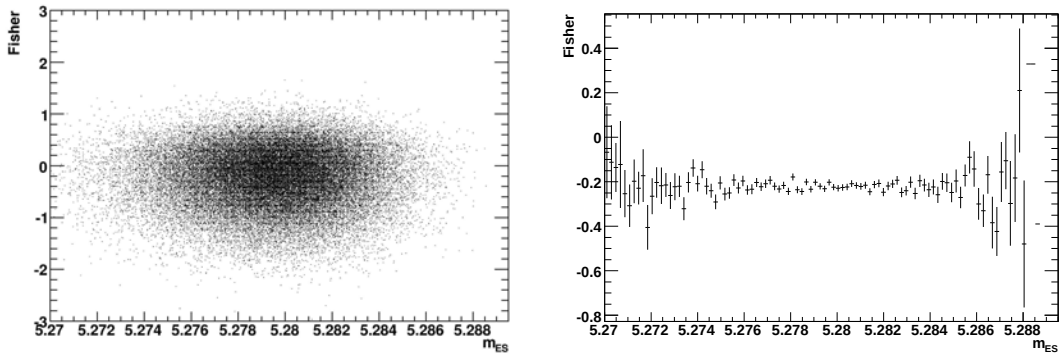

Figure 4.9: Scatter plot (left) of $\mathcal{F}$ vs. $m_{\rm ES}$ in signal MC events, and the corresponding profile histogram (right). The error bars in the profile histogram correspond to the error on the mean of the bin.

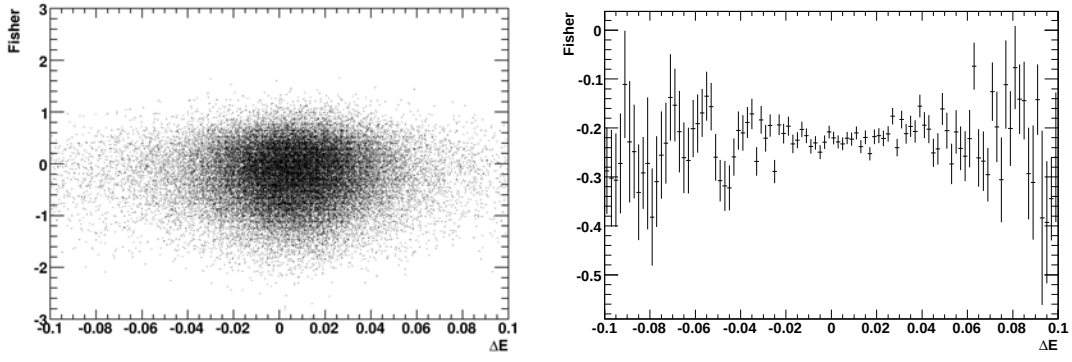

Figure 4.10: Scatter plot (left) of $\mathcal{F}$ vs. ΔE in signal MC events, and the corresponding profile histogram (right). The error bars in the profile histogram correspond to the error on the mean of the bin.

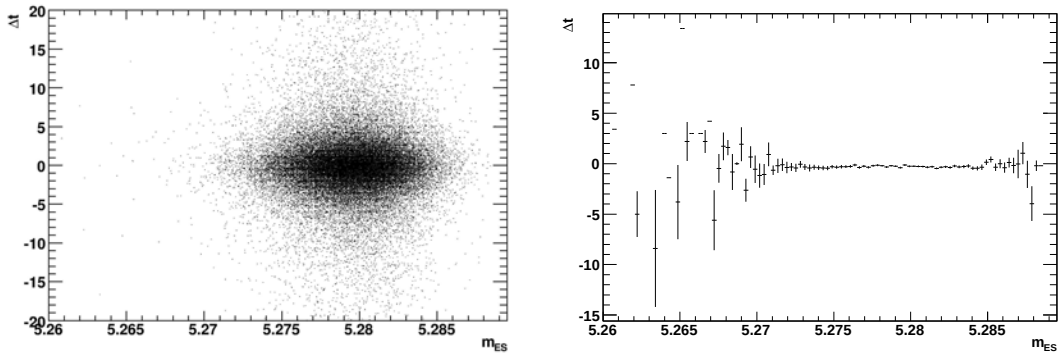

Figure 4.11: Scatter plot (left) of Δt vs. $m_{\rm ES}$ in signal MC events, and the corresponding profile histogram (right). The error bars in the profile histogram correspond to the error on the mean of the bin.

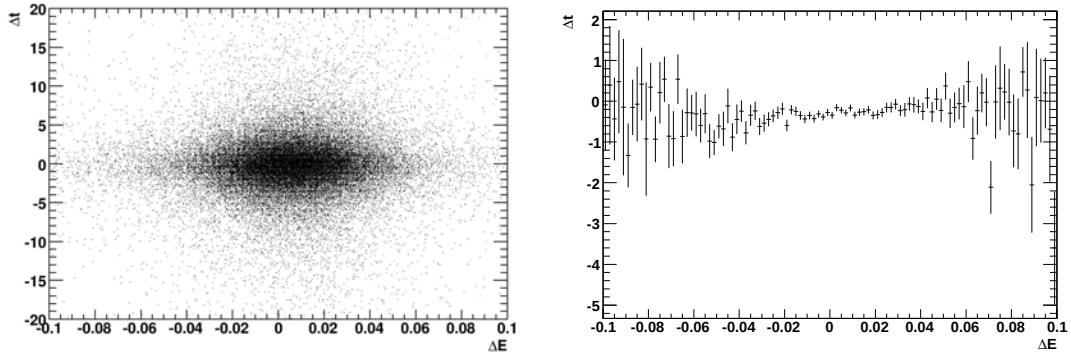

Figure 4.12: Scatter plot (left) of Δt vs. ΔE in signal MC events, and the corresponding profile histogram (right). The error bars in the profile histogram correspond to the error on the mean of the bin.

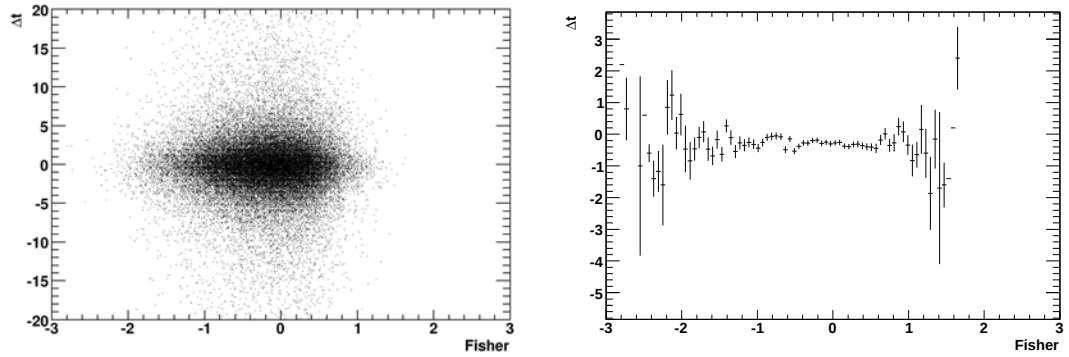

Figure 4.13: Scatter plot (left) of Δt vs. $\mathcal{F}$ in signal MC events, and the corresponding profile histogram (right). The error bars in the profile histogram correspond to the error on the mean of the bin.

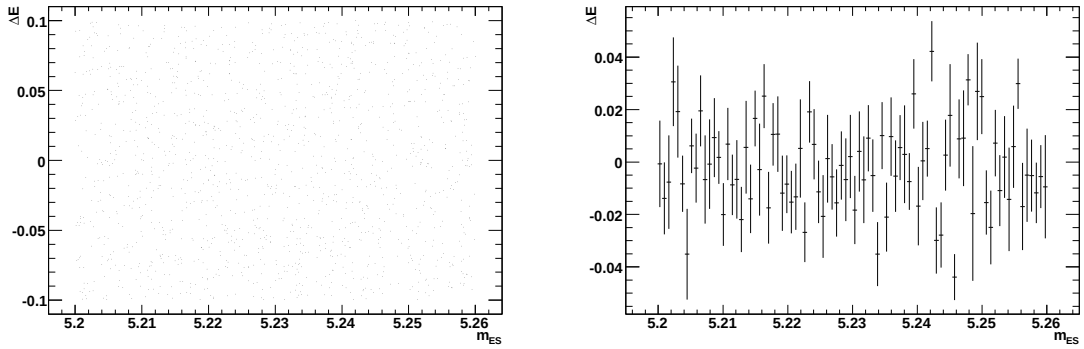

Figure 4.14: Scatter plot (left) of ΔE vs. $m_{\rm ES}$ in on-resonance $m_{\rm ES}$-sideband events, and the corresponding profile histogram (right). The error bars in the profile histogram correspond to the error on the mean of the bin.

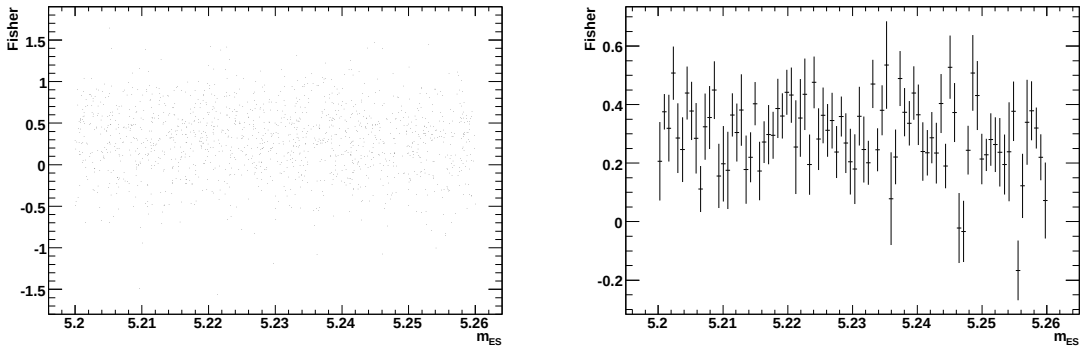

Figure 4.15: Scatter plot (left) of $\mathcal{F}$ vs. $m_{\rm ES}$ in on-resonance $m_{\rm ES}$-sideband events, and the corresponding profile histogram (right). The error bars in the profile histogram correspond to the error on the mean of the bin.

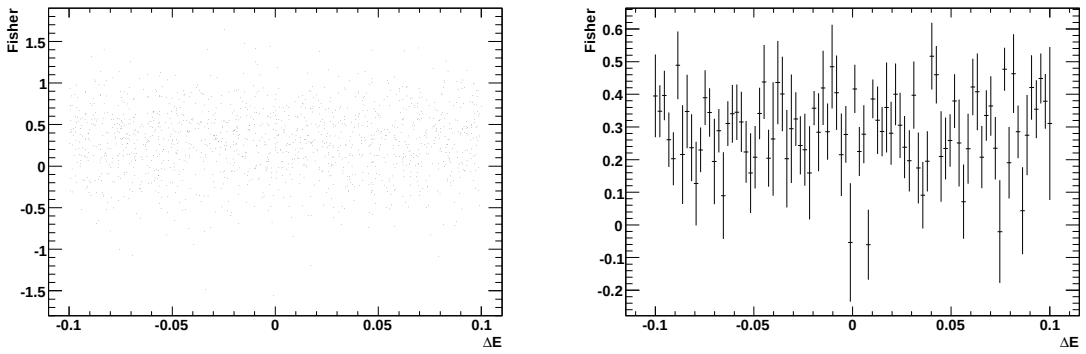

Figure 4.16: Scatter plot (left) of $\mathcal{F}$ vs. ΔE in on-resonance $m_{\rm ES}$-sideband events, and the corresponding profile histogram (right). The error bars in the profile histogram correspond to the error on the mean of the bin.

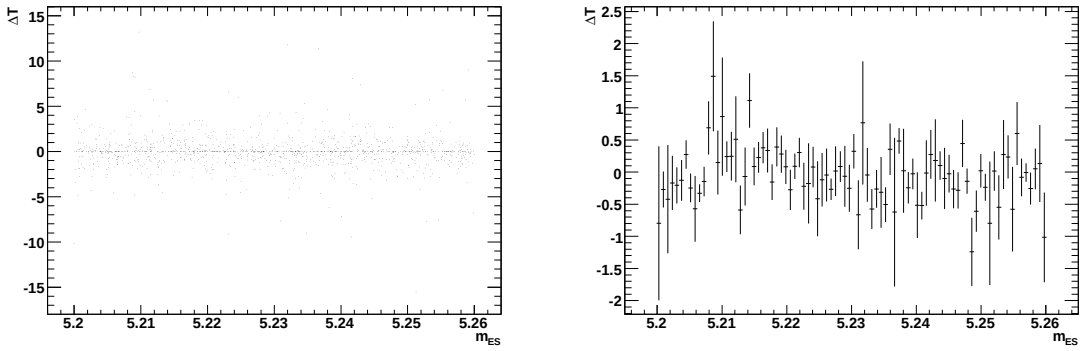

Figure 4.17: Scatter plot (left) of Δt vs. $m_{\rm ES}$ in on-resonance $m_{\rm ES}$-sideband events, and the corresponding profile histogram (right). The error bars in the profile histogram correspond to the error on the mean of the bin.

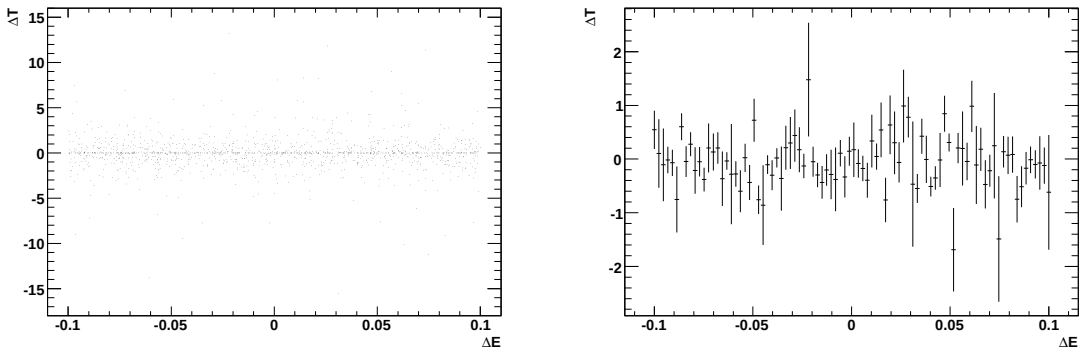

Figure 4.18: Scatter plot (left) of Δt vs. ΔE in on-resonance $m_{\rm ES}$-sideband events, and the corresponding profile histogram (right). The error bars in the profile histogram correspond to the error on the mean of the bin.

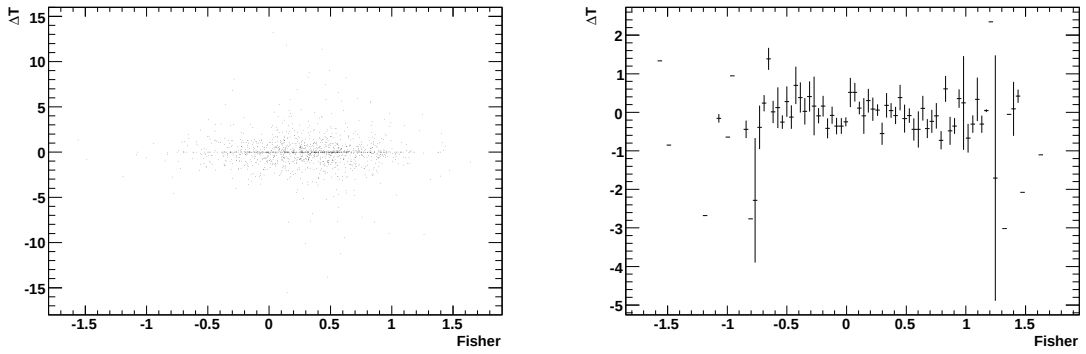

Figure 4.19: Scatter plot (left) of Δt vs. $\mathcal{F}$ in on-resonance $m_{\rm ES}$-sideband events, and the corresponding profile histogram (right). The error bars in the profile histogram correspond to the error on the mean of the bin.

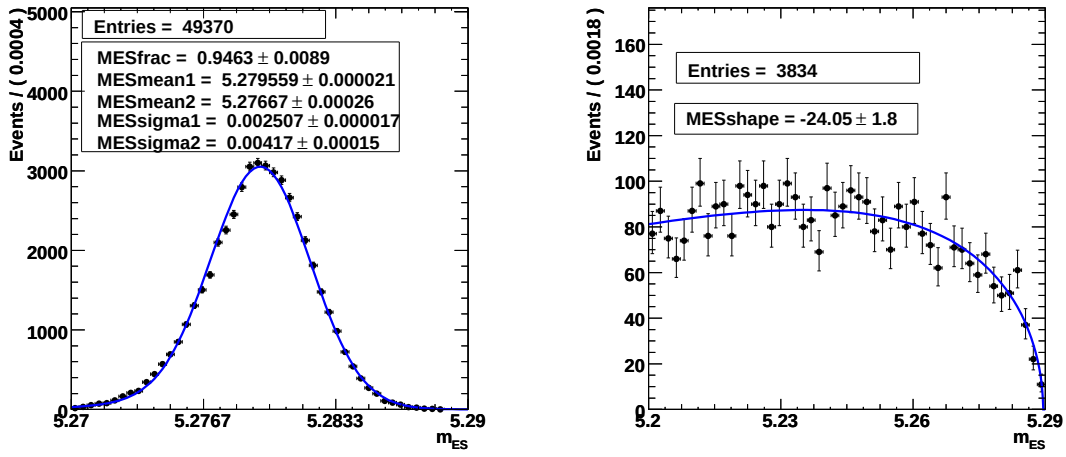

Figure 4.20: Distributions of $m_{\rm ES}$ for $B^0 \to K^0\overline{K}^0$ MC events (left) and on-resonance data (right) in the region $0.1 < |\Delta E| < 0.3\,{\rm GeV}$. The solid curves show the results of unbinned maximum likelihood fits to each sample.

of the core Gaussian.[7] Using a simple one-dimensional unbinned maximum likelihood fit, we fit the $m_{\rm ES}$ distribution in the $B^0 \to K^0\overline{K}^0$ signal MC sample to a double Gaussian hypothesis, obtaining $5.279559 \pm 0.000022\,{\rm GeV}/c^2$ and $2.507 \pm 0.017\,{\rm MeV}/c^2$ for the core mean and variance, respectively, with a core fraction of 0.9463 ± 0.0089. The corresponding numbers for the tail Gaussian are $5.27667 \pm 0.00026\,{\rm GeV}/c^2$ for the mean and $4.170 \pm 0.150\,{\rm MeV}/c^2$ for the variance (Fig. 4.20). The difference in the core mean in the related $B^+ \to K^0\pi^+$ analysis between the fit to the signal MC sample and the fit to data is only $0.4\,{\rm MeV}/c^2$. Thus, we use the value of the core mean from the MC fit in the fit to data in this analysis.

The continuum $m_{\rm ES}$ variable is parameterized by an empirically determined threshold function with a cut-off at $5.2895\,{\rm GeV}/c^2$ (corresponding to $\sqrt{s}/2$, the CM beam energy), first proposed by the ARGUS collaboration:

$$\mathcal{P}_{\rm bkg}(m_{\rm ES}) = \sqrt{1-(m_{\rm ES}/\sqrt{s})^2}\; e^{-\xi(1-(m_{\rm ES}/\sqrt{s})^2)}. \tag{4.18}$$

Its single parameter, the curvature parameter ξ is floated in the fit to data. A fit to the ΔE sideband, defined as $0.1 < |\Delta E| < 0.3\,{\rm GeV}$, in our data sample yields $\xi = 24.05 \pm 1.80$ (right side of Fig. 4.20), which is consistent with the final fit to data shown later.

4.4.2 ΔE

The distribution of the ΔE variable in the signal is parameterized as a double Gaussian, with both Gaussians constrained to a common mean. The two variances as well as the weights of the two components are determined in a fit to the $B^0 \to K^0\overline{K}^0$ MC sample, shown in Fig. 4.21. We obtain $0.018760 \pm 0.00019\,{\rm GeV}$ and $0.0447 \pm 0.0011\,{\rm GeV}$ for the two variances and $0.760 \pm 0.012\,{\rm GeV}$ for the fraction of the first component of the double Gaussian.

[7] All PDFs are normalized to unity, but the normalization factor is not shown in the equations for simplicity.

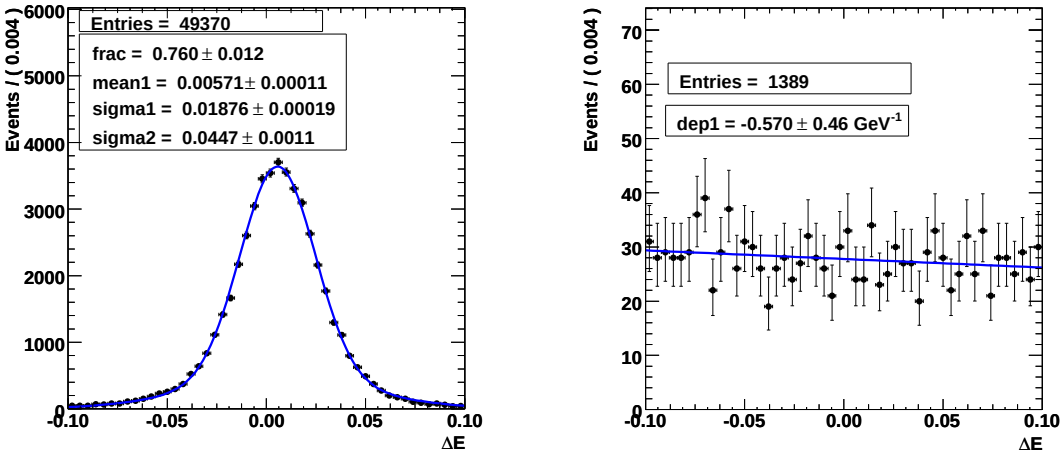

Figure 4.21: Distributions of ΔE for $B^0 \to K^0\overline{K}^0$ signal MC events (left) and on-resonance data in the $m_{\rm ES}$-sideband region (right). The solid curves show the results of unbinned maximum likelihood fits.

The fit produces a mean of 5.71 ± 0.11 MeV. In *BABAR*'s Monte Carlo samples, the signal MC value of this parameter shows a clear dependence on the number of K^0_S's in the final state in the three modes, $B^+ \to K^0_S\pi^+$, $B^0 \to K^0_S K^0_S$, and $B^0 \to K^0_S K^0_S K^0_S$: the three values are 2.80 ± 0.10 MeV, 5.71 ± 0.11 MeV, and 7.11 ± 0.15 MeV, respectively. This relationship is due to slight flaws in K^0_S reconstruction and is imperfectly modeled by the GEANT detector simulation. Considering the difference between data and signal MC in the value of the core mean, we observe statistically consistent offsets in $K^0_S\pi^+$ and $K^0_S K^0_S K^0_S$. (The offsets are -3.4 ± 1.5 MeV and -3.1 ± 2.5 MeV, respectively. These two modes have enough signal in data to float the ΔE mean in the fit to data.) We assume that the data-MC offset in $K^0_S K^0_S$ is the average of the corresponding offsets in $K^0_S\pi^+$ and $K^0_S K^0_S K^0_S$. Thus, to correct for the discrepancy between the data and MC samples, we adjust the value of the mean obtained from the $K^0_S K^0_S$ MC sample to $2.6^{+1.5}_{-3.2}$ MeV. The asymmetric errors cover the interval $[-0.6, 4.1]$ MeV, where the left and right boundaries are the values of the mean in the fit to data in the $K^0_S\pi^+$ and $K^0_S K^0_S K^0_S$ analyses, respectively, as we conservatively assume that the data value in $K^0_S K^0_S$ lies between them (since it does in the MC samples).

The background ΔE shape is modeled as a first-degree polynomial

$$\mathcal{P}_{\rm bkg}(\Delta E) = 1 + p\Delta E, \tag{4.19}$$

with the slope p floated in the fit. A fit to the $m_{\rm ES}$ sideband in our data sample yields $p = -0.570 \pm 0.46\,{\rm GeV}$ (right side of Fig. 4.21), which is consistent with the final fit to data shown later.

4.4.3 $\mathcal{F}$

We parameterize the signal Fisher shape with an asymmetrical Gaussian, having a different variance on the left and right side of the mean:

$$\mathcal{P}_{\rm sig}(\mathcal{F}) = \begin{cases} e^{-(\mathcal{F}-\mu)^2/(2\sigma_L^2)} & \mathcal{F} \leq \mu \\ e^{-(\mathcal{F}-\mu)^2/(2\sigma_R^2)} & \mathcal{F} > \mu \end{cases} \tag{4.20}$$

We determine its parameters from a fit to the $B^0 \to K^0\overline{K}^0$ MC sample. The fitted values are 0.001 ± 0.006 for the mean, and 0.6875 ± 0.0042 and 0.3981 ± 0.0037 for the left and right variances, respectively.

The background Fisher is modeled as a double Gaussian. Its five parameters are floated in the final fit. The set of parameter values extracted from a double-Gaussian fit to the $m_{\rm ES}$-sideband is consistent with the final fit to data. Figure 4.22 shows the distributions and fits of the Fisher in the signal MC sample and in the $m_{\rm ES}$-sideband.

4.4.4 Δt

The Δt PDF, which depends on the $B_{\rm tag}$ flavor, is parameterized separately for the *CP*-Good and *CP*-Bad components of the signal and background. For the *CP*-Good signal PDF we use Eq. 4.6 modified for the effects of imperfect flavor tagging, such as the mistag rates w, and detector-resolution effects [46]. For convenience, we define the dilution parameter $D = 1 - 2w$. Dilutions can be different for B^0 and $\overline{B}^0$ decays,

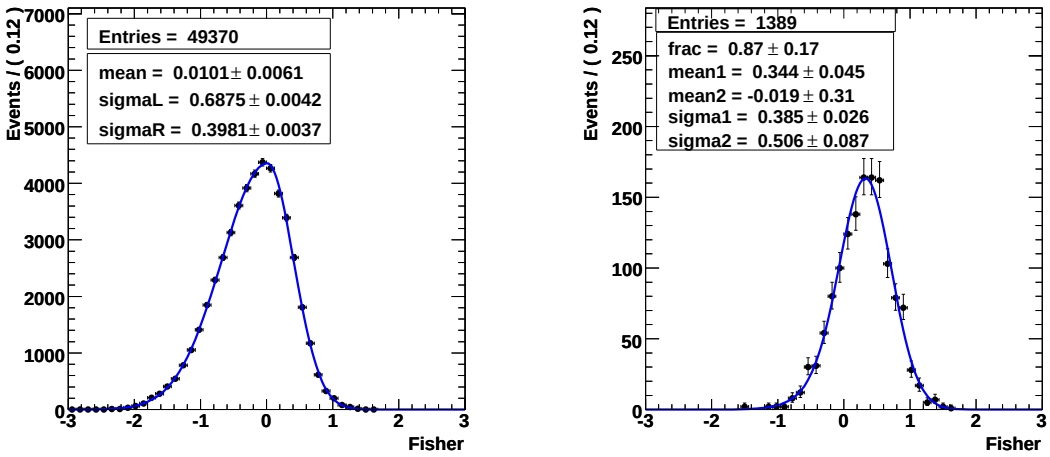

Figure 4.22: Distributions of $\mathcal{F}$ for $B^0 \to K^0\overline{K}^0$ MC events (left) and on-resonance data (right) in the $m_{\rm ES}$-sideband region. The solid curves show the results of unbinned maximum likelihood fits to each sample.

as can be the tagging efficiencies ϵ, introducing fake CP-violating effects that need to be taken into account in the Δt PDF. We define the average dilution and dilution difference

$$\begin{aligned} \langle D \rangle &= \frac{D + \overline{D}}{2}, \\ \Delta D &= D - \overline{D}, \end{aligned} \tag{4.21}$$

and an average efficiency and efficiency asymmetry

$$\begin{aligned} \langle \epsilon \rangle &= \frac{\epsilon + \bar{\epsilon}}{2}, \\ \mu &= \frac{\epsilon - \bar{\epsilon}}{\epsilon + \bar{\epsilon}}, \end{aligned} \tag{4.22}$$

Category	D	ΔD	μ	$\epsilon_{\rm tag}$
Lepton	0.9420 ± 0.0072	-0.0014 ± 0.0136	0.0029 ± 0.0121	0.087 ± 0.001
Kaon1	0.8952 ± 0.0084	0.0160 ± 0.0154	-0.0005 ± 0.0118	0.110 ± 0.001
Kaon2	0.7002 ± 0.0084	0.0112 ± 0.0144	-0.0036 ± 0.0103	0.172 ± 0.001
KaonPion	0.5330 ± 0.0106	0.0608 ± 0.0170	-0.0183 ± 0.0116	0.138 ± 0.001
Pions	0.3468 ± 0.0110	-0.1054 ± 0.0170	-0.0300 ± 0.0116	0.143 ± 0.001
Other	0.1624 ± 0.0136	-0.0776 ± 0.0204	0.0214 ± 0.0133	0.096 ± 0.001

Table 4.5: Summary of the signal Δt parameterization used in the maximum likelihood fit.

where quantities with and without a bar indicate a B^0 and $\overline{B}^0$ tag for the other B in the event, respectively. Accounting for these effects, the PDF becomes

$$f_{B^0_{\rm tag}}(t) = \frac{e^{-|\Delta t|/\tau}}{4\tau\left(1 - C\mu\zeta\right)}\langle\epsilon\rangle \left\{1 + \frac{\Delta D}{2} + \mu\langle D\rangle + \left[\langle D\rangle + \mu\left(1 + \frac{\Delta D}{2}\right)\right]\mathcal{A}\right\}, \quad (4.23)$$
$$f_{\overline{B}^0_{\rm tag}}(t) = \frac{e^{-|\Delta t|/\tau}}{4\tau\left(1 - C\mu\zeta\right)}\langle\epsilon\rangle \left\{1 - \frac{\Delta D}{2} - \mu\langle D\rangle - \left[\langle D\rangle - \mu\left(1 - \frac{\Delta D}{2}\right)\right]\mathcal{A}\right\},$$

where

$$\mathcal{A} = \left[S\sin\left(\Delta m_d \Delta t\right) - C\cos\left(\Delta m_d \Delta t\right)\right], \quad (4.24)$$

τ is the B-meson lifetime, Δm_d is the $B^0 - \overline{B}^0$ mixing frequency, $\zeta = \frac{1}{1+(\tau\Delta m)^2}$, and S and C are the CP parameters. We can see that mistagging changes the measured number of events of each flavor as well as the fraction of events that oscillate according to $\mathcal{A}$. For an event in a given tagging category, the PDF is evaluated with the appropriate values of the mistag parameters obtained from the $B_{\rm flav}$ sample, as summarized in Table 4.5. The values of τ and Δm_d are taken from the PDG [20].

Δt is determined from the vertices of the two B mesons in an event. The instrumental and vertexing uncertainty on this measurement results in deviations δt of the measured value from the true value, with an average of 0.9 ps. The resolution

Tagging Category	b_{core}	S_{core}
Lepton	-0.0412 ± 0.0339 ps	1.0417 ± 0.0518 ps
Others	-0.1833 ± 0.0153 ps	1.0898 ± 0.0250 ps
b_{tail}	-1.1985 ± 0.1567 ps	
S_{tail}	3 ps	
f_{tail}	0.1028 ± 0.0097	
μ_{outl}	0 ps	
σ_{outl}	8 ps	
f_{outl}	0.0037 ± 0.0007	

Table 4.6: Summary of the signal Δt parameterization of the resolution function used in the maximum likelihood fit.

function that models this difference follows a triple Gaussian shape,

$$\mathcal{R}(\delta t) = \sum_{k=\text{core, tail}} \frac{f_k}{S_k \sigma_{\Delta t}\sqrt{2\pi}} \exp\left(-\frac{(\delta t - b_k \sigma_{\Delta t})^2}{2(S_k \sigma_{\Delta t})^2}\right) + \frac{1 - f_{\text{core}} - f_{\text{tail}}}{\sigma_{\text{outl}}\sqrt{2\pi}} \exp\left(-\frac{(\delta t)^2}{2\sigma_{\text{outl}}^2}\right), \tag{4.25}$$

with core and tail Gaussians having bias b and scale factor S both scaled by the measured Δt uncertainty. (The third "outlier" Gaussian parameterizes poorly vertexed decays with large Δt uncertainties.) As the Δt resolution is a linear function of its measured uncertainty, the scale factor effectively provides a separate resolution function at each measured value of $\sigma_{\Delta t}$ for a more accurate modeling of the detector resolution. The bias is also linearly dependent on $\sigma_{\Delta t}$ as it mostly arises from D decay vertices, which can be displaced by a up to a few hundred microns from the vertex of the parent B. This effect is dependent on the direction of the D momentum, with varying effect on the uncertainty: the effect will be largest for a D propagating along the beam direction, resulting in a large Δt uncertainty, while a D traveling transversely will not significantly affect Δz or its error. The biases b model this correlation.

The functional form and the parameters of the resolution function are taken from the B_{flav} sample. This can be done since the Δt resolution is dominated by the uncertainty on the B_{tag} vertex, which is the same for all decay modes of the signal B.

For the core Gaussian the parameters are different for the Lepton tagging category than for the other categories, while no category dependent differences are imposed for the tail and outlier Gaussians (Table 4.6). The final Δt PDF is Eq. 4.24 convoluted with the resolution function:

$$\mathcal{P}_{\rm sig}(\Delta t) = \int_{-\infty}^{\infty} \mathcal{P}(\tau)\mathcal{R}(\Delta t - \tau)d\tau, \tag{4.26}$$

which effectively applies the resolution function separately at each point of the raw PDF. Figure 4.23 shows the Δt distributions in signal MC separated according to flavor and tagging categories with the results of the full fit on the MC sample overlaid. Figure 4.24 shows the corresponding plot summed over all tagging categories. As the signal MC sample was generated with $S = 0.9118$ and $C = 0$, the distributions show a clear offset between B^0 and $\overline{B}^0$ tags due to the large sinusoidal term in the PDF.

The *CP*-Bad signal events do not have sufficient vertex information to be used in a time-dependent fit. For these events we use instead the *CP*-Good distribution integrated over the Δt range to extract the direct-*CP* violating parameter C, which is constrained in the fit to be the same as the C parameter in the *CP*-Good PDF. The integrated PDF is the following:

$$f_{B^0_{\rm tag}}(t) = \frac{1}{2\left(1 - C\mu\zeta\right)}\langle\epsilon\rangle \left\{1 + \frac{\Delta D}{2} + \mu\langle D\rangle - C\cdot\zeta\left[\langle D\rangle + \mu\left(1 + \frac{\Delta D}{2}\right)\right]\right\}, \tag{4.27}$$
$$f_{\overline{B}^0_{\rm tag}}(t) = \frac{1}{2\left(1 - C\mu\zeta\right)}\langle\epsilon\rangle \left\{1 - \frac{\Delta D}{2} - \mu\langle D\rangle + C\cdot\zeta\left[\langle D\rangle - \mu\left(1 - \frac{\Delta D}{2}\right)\right]\right\},$$

where are all parameters are the same as in the *CP*-Good PDF. For untagged events no CP information can be extracted and all the tagging parameters are set to zero in the above PDF.

The background does not contain any $B\overline{B}$ events and the quarks in continuum events hadronize with an effective lifetime of zero. However, they are susceptible to similar resolution effects (such as D-meson bias) as the signal, so the background

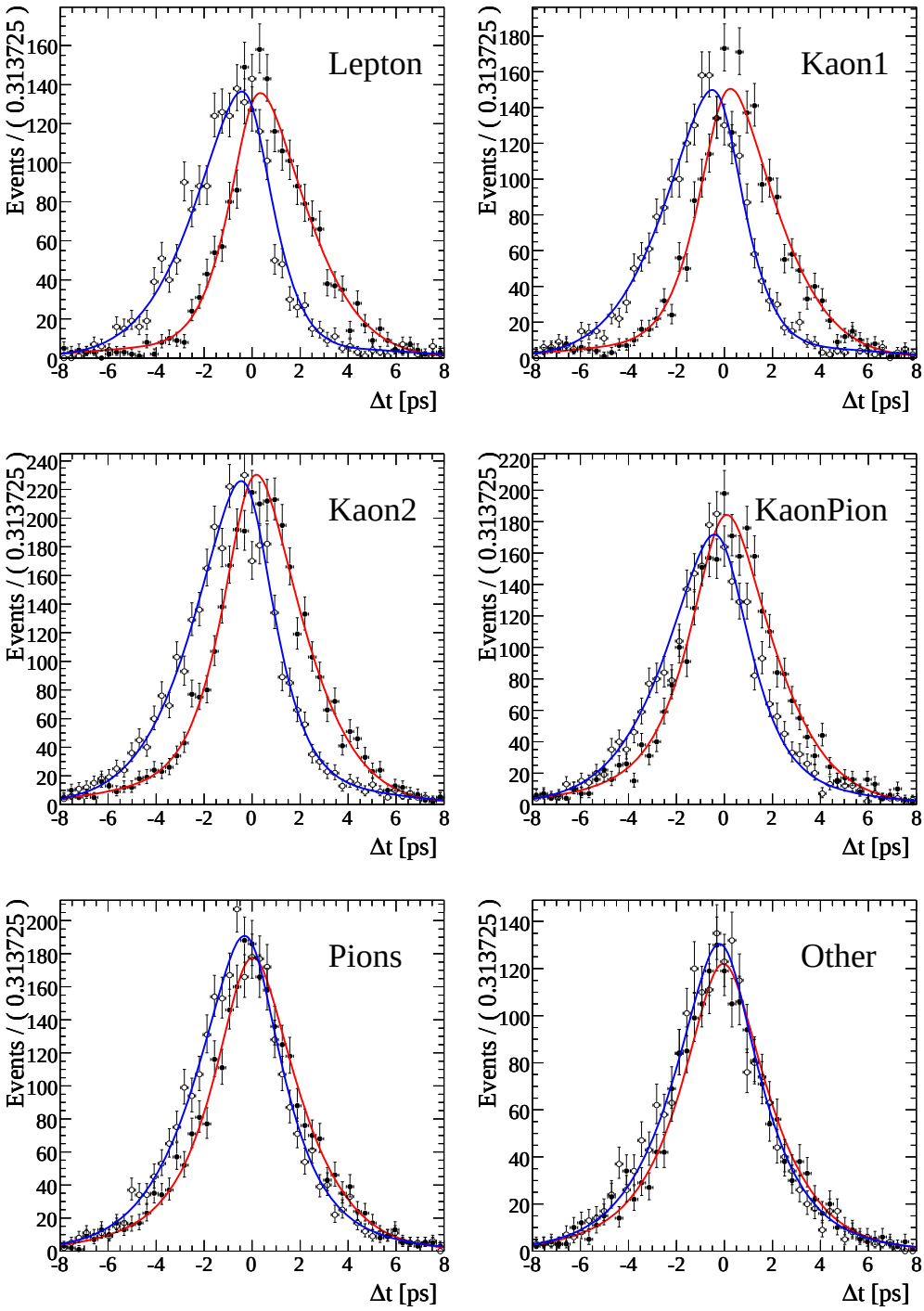

Figure 4.23: Distributions of Δt for $B^0 \to K^0\overline{K}^0$ MC events in the six tagging categories. Closed (open) circles are the $B^0_{\rm tag}$ and $\overline{B}^0_{\rm tag}$ events, respectively. Projections of the likelihood function for $B^0_{\rm tag}$ (red) and $\overline{B}^0_{\rm tag}$ (blue) are overlaid.

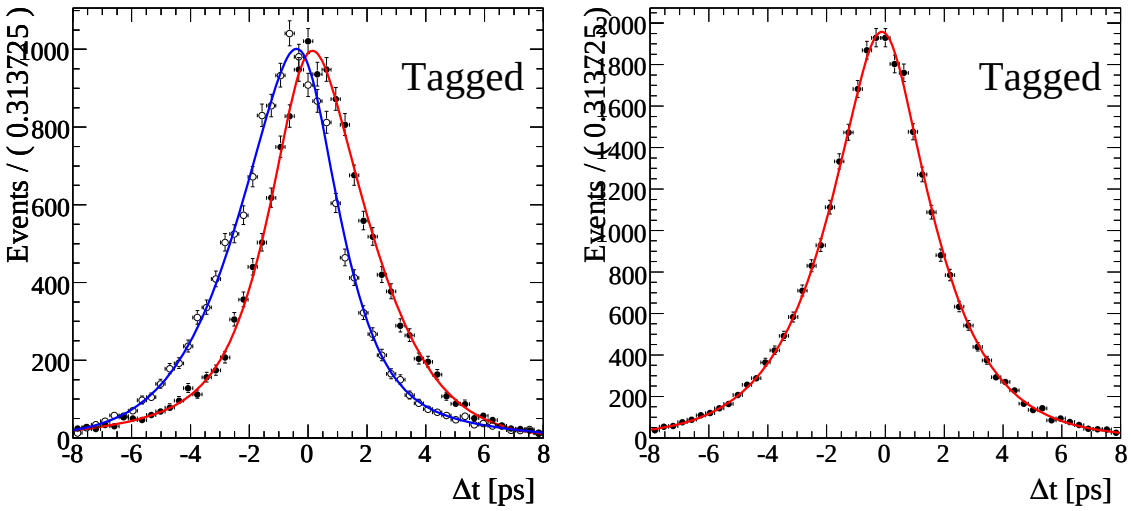

Figure 4.24: Distributions of Δt for $B^0 \to K^0\overline{K}^0$ MC events for all tagged events with the projection of the likelihood function overlaid. The left plot shows the sample divided between $B^0_{\rm tag}$ and $\overline{B}^0_{\rm tag}$ events (red curve on closed circles and blue curve on open circles, respectively), while the right plot shows the sum of both tags.

PDF for *CP*-Good candidates is parameterized as a Delta function convoluted with the same resolution function as in the signal *CP*-Good PDF. The parameters of the resolution function are floated in the fit. Although no *CP*-violating effects exist in continuum processes, tagging asymmetries can still be present from flavor correlations between the two quarks. To account for effects of this kind, the PDF is multiplied by the flavor-dependent efficiency factor,

$$\epsilon = \langle\epsilon\rangle(1 + F\mu), \tag{4.28}$$

where ϵ, $\langle\epsilon\rangle$, and μ are defined as before and F is $+1$ and -1 for B^0 and $\overline{B}^0$ tags, respectively. The PDF is split according to tag category as before, and the efficiencies and efficiency asymmetries are floated in the fit. The *CP*-Bad PDF for background is simply a constant function with the same efficiency factors as in the *CP*-Good PDF. Like in the signal PDF, untagged events have all tagging parameters set to zero in the background PDF.

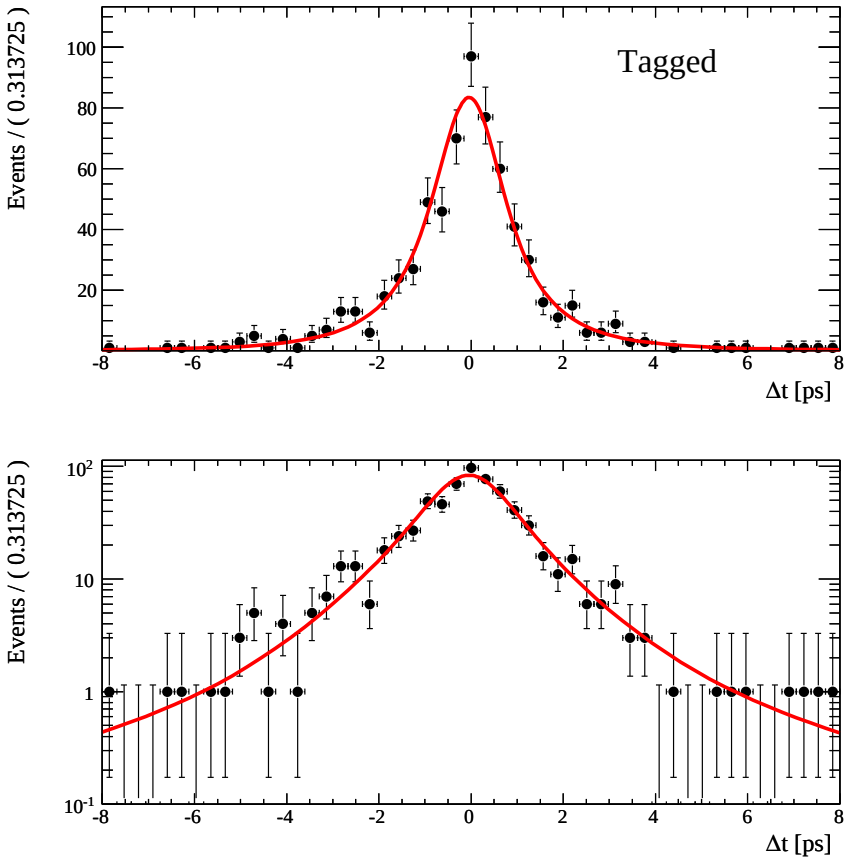

Figure 4.25: Distribution of Δt in the data sample for tagged events with the projection of the likelihood function overlaid (top). The bottom plot shows the same plot on a logarithmic scale to illustrate the good agreement between the PDF model and the tails of the distribution.

Figure 4.25 shows the Δt distributions in the data sample with the results of the final fit overlaid. As the sample is mostly background, the plots demonstrate that the resolution function for background is modeled correctly. It should be noted that even in the absence of CP-violating effects in the signal, the Δt PDF contributes to signal-background discrimination, as the signal PDF is wider than the background PDF due to the 1.5 ps lifetime of the B meson.

4.4.5 Summary

Our parameterization of the non-time-dependent signal and background PDFs is summarized in Table 4.7. Table 4.8 shows all the parameters floated in the final fit.

4.5 Validation of the Fit

Several studies were performed to validate the maximum-likelihood fit. The main technique involves "toy" MC pseudo-experiments, wherein mock datasets are generated by random sampling from the PDFs of the model and then fitted with the full fit. During generation, the PDF parameters, including the signal and background yields and S and C, are set to the values expected in data. The generated value can then be compared with the value determined by the fit to check for intrinsic biases present in the fit model, and to verify the resolutions on the fitted parameters. With many such pseudo-experiments, the distribution of the "pull," or normalized residual, of a parameter x

$$Pull = \frac{x_{\mathrm{Fitted}} - x_{\mathrm{Generated}}}{\sigma_{x_{\mathrm{Fitted}}}} \tag{4.29}$$

should follow a Gaussian distribution with mean zero, indicating no biases, and width one, signifying that the fit returns an error on the parameter consistent with the resolution of the distribution. (A width greater than one would indicate that the fitted errors are underestimated, for instance.)

Variable	PDF	Parameters
$\boldsymbol{m_{\mathrm{ES}}}$		
Signal	Gaussian	$\mu_{\mathrm{core}} = 5.279559 \pm 0.000022\,\mathrm{GeV}/c^2$
		$\mu_{\mathrm{tail}} = 5.27667 \pm 0.00026\,\mathrm{GeV}/c^2$
		$\sigma_{\mathrm{core}} = 2.507 \pm 0.017\,\mathrm{MeV}/c^2$
		$\sigma_{\mathrm{tail}} = 4.170 \pm 0.150\,\mathrm{MeV}/c^2$
		$f_{\mathrm{core}} = 0.9463 \pm 0.0089\,\mathrm{MeV}/c^2$
Background	ARGUS	Floated in the fit
$\boldsymbol{\Delta E}$		
Signal	Double Gaussian	$\mu = 2.6^{+1.5}_{-3.2}\,\mathrm{MeV}$
		$\sigma_{\mathrm{core}} = 18.76 \pm 0.19\,\mathrm{MeV}$
		$\sigma_{\mathrm{tail}} = 44.7 \pm 1.1\,\mathrm{MeV}$
		$f_{\mathrm{core}} = 0.760 \pm 0.012$
Background	Linear	Floated in the fit
$\boldsymbol{\mathcal{F}}$		
Signal	Asymmetric Gaussian	$\mu = 0.001 \pm 0.006$
		$\sigma_{\mathrm{L}} = 0.6875 \pm 0.0042$
		$\sigma_{\mathrm{R}} = 0.3981 \pm 0.0037$
Background	Double Gaussian	Floated in the fit

Table 4.7: Summary of the PDF shapes and parameters used in the maximum likelihood fit.

Signal yield
Background yield
CP Parameter S
CP Parameter C
Background m_{ES} Argus shape
Background ΔE slope
Background Fisher 2G (μ_{core}, μ_{tail}, σ_{core}, σ_{tail}, and f_{core})
Background Δt RF 3G (μ_{core}, σ_{core}, μ_{tail}, f_{tail}, and f_{outlier})
Background tagging flavor asymmetries (six parameters)
Background tagging efficiencies (six parameters)
Signal and background CP-Good fractions

Table 4.8: The 30 parameters floated in the final fit. "RF" stands for "resolution function" and "2G" and "3G" stand for "double Gaussian" and "triple Gaussian," respectively.

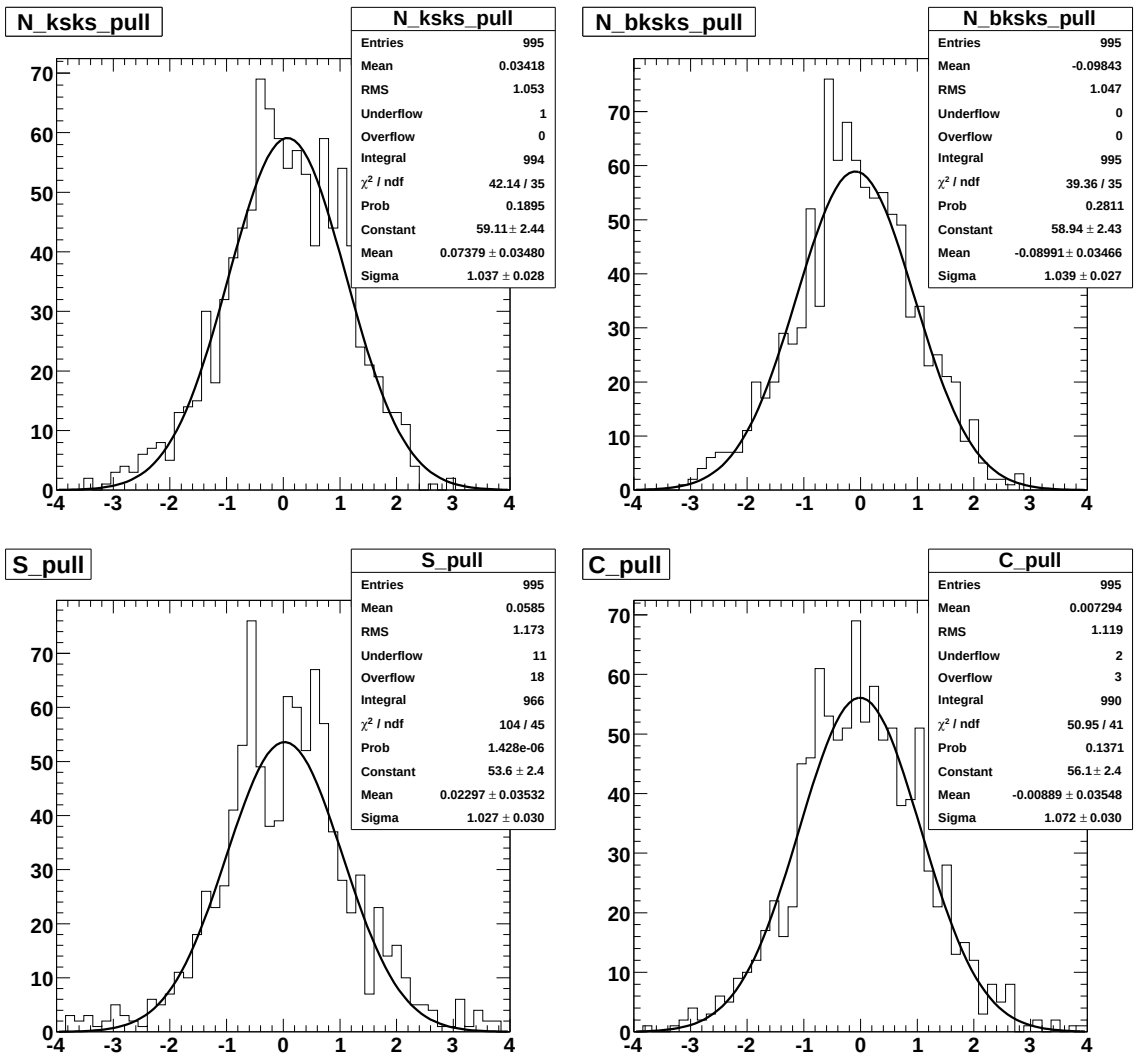

Figure 4.26: The pull distribution of in 1000 toy MC experiments with a generated yield of 42 signal events and 2132 background events and $S = C = 0$. The plots are for signal yield (top left), background yield (top right), S (bottom left), and C (bottom right).

In the previous analysis of this mode published in 2005 [7],[8] *BABAR* reported a signal yield of $23^{+8}_{-7}\pm2$ events, corresponding to 4.5σ evidence for a branching fraction of $(1.19^{+0.40}_{-0.35} \pm 0.13) \times 10^{-6}$. (No time-dependent fit was performed.) Extrapolating this result to a typical integrated luminosity that was expected for this analysis, we generated 1000 toy experiments with 42 signal and 2132 background events.[9] The pull distributions are shown in Figure 4.26. No significant biases are observed.

A similar procedure is applied setting $S = C = 0.5$. The pull distributions are shown in Figure 4.27. No bias is detected in the fitted yields. The biases on the *CP* parameters are 0.15 ± 0.04 on S and 0.06 ± 0.04 on C. This bias can typically be found in time-dependent analyses with limited signal statistics when S and C are close to the physically allowed boundary, $S^2 + C^2 = 1$. The S term in the Δt PDF has a sinusoidal form, and the uncertainty on the amplitude of a sine term is smaller for larger values of the amplitude, since then it can be easily resolved by the fit. Thus, a fluctuation in a dataset towards a large, unphysical value of S, which is possible with $S_{\rm Generated} = 0.5$ due to the small signal size, would result in an underestimated error on S and an overall pull bias towards fitted values of larger magnitudes. This is also what causes the increased widths in the pull distributions of S and C. (C is affected as its error is correlated with the error on S in the fit.)

The $S_{\rm Fitted}$-dependent bias can be studied by generating these experiments with S and C values sampled randomly in the physically allowed region. Plots of the fitted values and the pulls versus the generated values of S and C are shown in Fig. 4.28 for $10,000$ experiments. The amplitude-dependent bias is clearly visible. As this bias is dependent on the fitted values and their errors, its magnitude can be determined only after the final fit to data is performed. If potential bias is likely, the observed slope of the fitted values in Fig. 4.28 can then be used to correct the result. The error distributions in these experiments are shown in Fig. 4.29.

[8] The author of this dissertation was the primary author of the 2005 analysis.

[9] To account for counting statistics, the actual values of the generated yields are sampled from Poisson distributions with means given by these numbers.

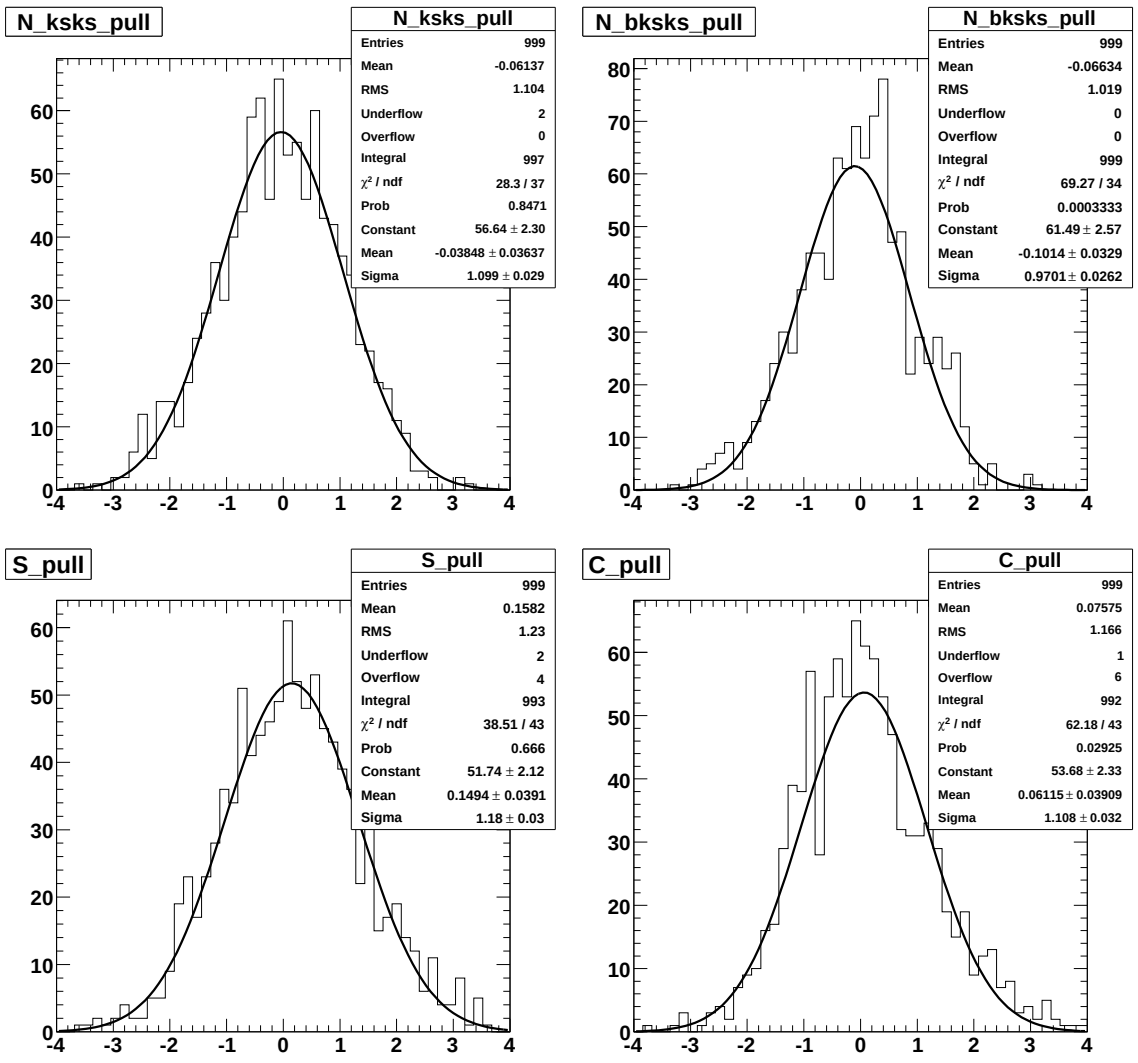

Figure 4.27: The pull distribution of in 1000 toy MC experiments with a generated yield of 42 signal events and 2132 background events and $S = C = 0.5$. The plots are for signal yield (top left), background yield (top right), S (bottom left), and C (bottom right).

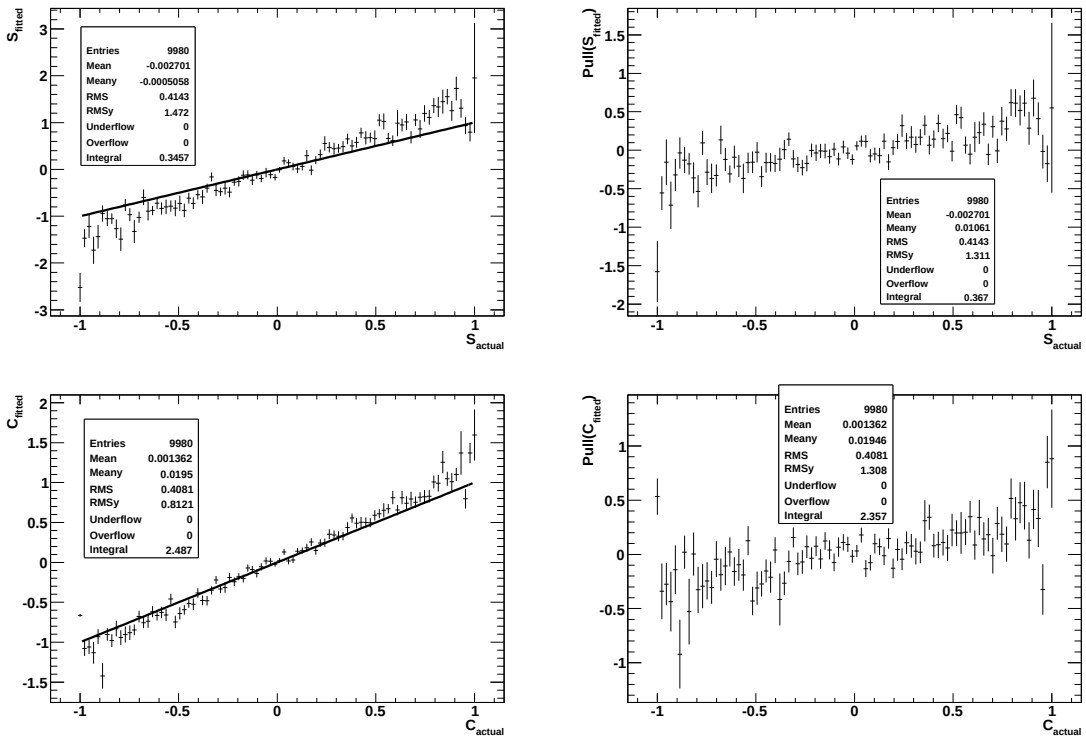

Figure 4.28: Profile histograms in a set of 10000 toy MC experiments of the fitted S versus the generated S (top left), the pull on S versus the generated S (top right), and the corresponding plots for C (bottom left and right). The black line in the left plots corresponds to $S, C_{\text{fitted}} = S, C_{\text{actual}}$.

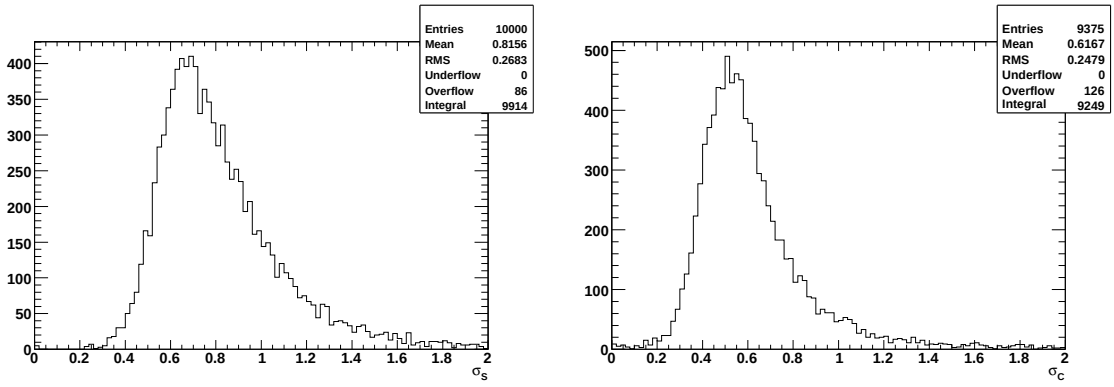

Figure 4.29: The error on S (left) and C (right) in toy experiments where $S^2+C^2 \leq 1$.

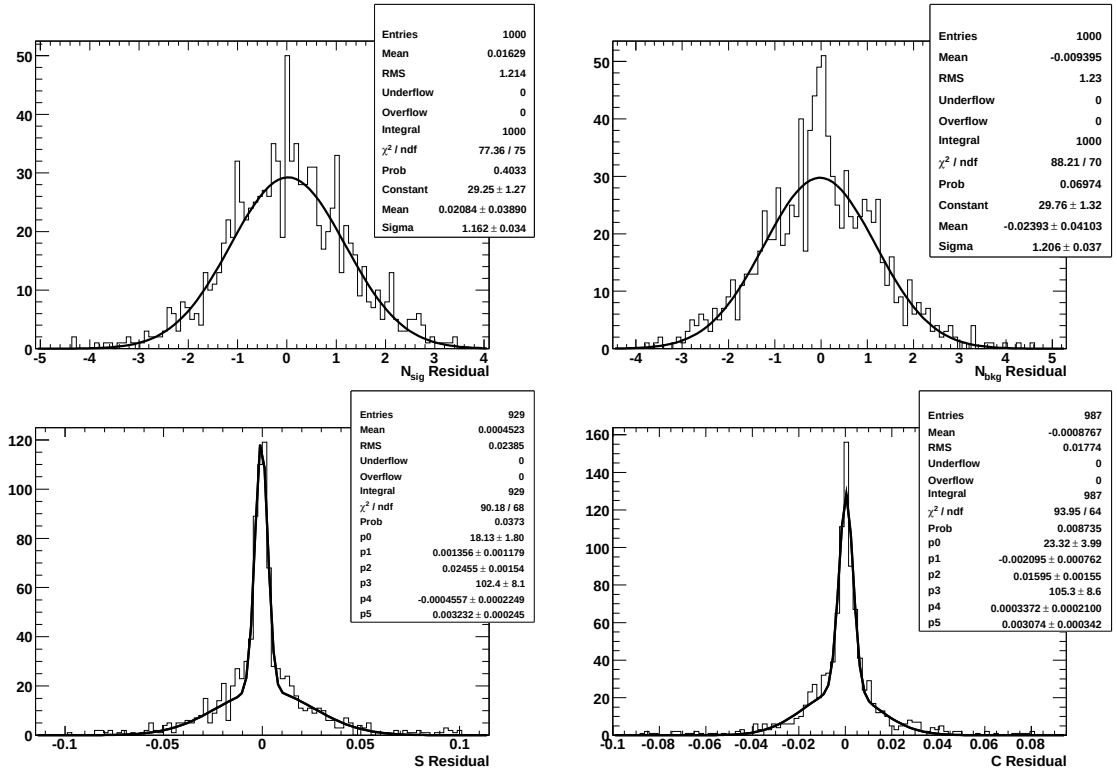

Figure 4.30: Distributions of the experiment-by-experiment residuals in 1000 toy experiments for the fit where the background $m_{\rm ES}$ and ΔE parameters are floated versus the fit where they are fixed to values determined from the ΔE and $m_{\rm ES}$ sidebands, respectively.

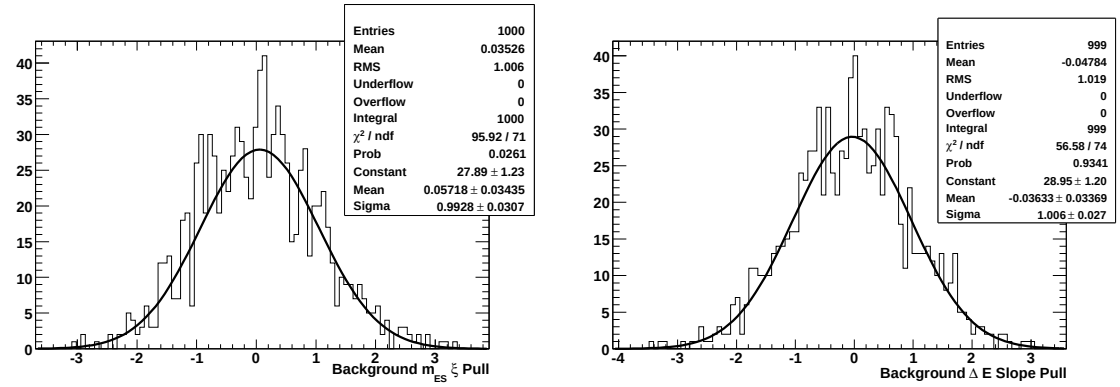

Figure 4.31: Distributions of the experiment-by-experiment pulls in the background $m_{\rm ES}$ and ΔE parameters in 1000 toy experiments where these parameters are floated.

We also ran 1000 toy experiments to determine the effect of floating the background $m_{\rm ES}$ parameter ξ and the background ΔE slope p in the fit. Figure 4.30 shows the distribution of residuals for S and C and the yields, computed as the difference in every experiment between the value with ξ and p floated in the fit and the value with ξ and p fixed. Figure 4.31 shows the pull distributions of ξ and p themselves. No biases are observed and the statistical errors on the physical parameters are negligibly greater in the floating fit than in the fixed fit. The results validate floating ξ and p in the fit, which is desirable as it decreases systematic uncertainties from PDF modeling.

The previous toy studies test for internal imperfections of the fit model, but do not account for differences between the model and the actual behavior of the fit variables. To account for the effect of correlations among the variables or improperly modeled tagging effects, we generate and fit a set of approximately 1000 independent experiments were the signal events are sampled randomly from the signal MC sample, while the background events are generated from the PDFs as before. Figure 4.32 shows the distributions of the residuals, $x_{\rm Fitted} - x_{\rm Generated}$, for the signal and background yields. The signal residual distribution, presented in Fig. 4.32, has a bias of -2.73 ± 0.26 events. We assign this bias as a symmetric systematic uncertainty on the yield, as it is small compared with the expected statistical error (8.7 events, as determined from the width of the residual distribution).

The signal MC sample was generated with $S = 0.9118$ and $C = 0$. Thus, the bias and error underestimation seen in the pull distributions for S and C in Fig. 4.32 are consistent with the toy pseudo-experiments for large values of S. We also fit the entire signal MC sample of $49,370$ $B^0 \to K^0\overline{K}^0$ signal events (with all selection criteria applied), obtaining $N_{\rm sig} = 49364 \pm 222$ events, $N_{\rm bkg} = 6.2 \pm 3.3$ events, $C = -0.010 \pm 0.011$, and $S = 0.879 \pm 0.016$.[10] Figure 4.33 shows the time-dependent flavor-asymmetry for tagged *CP*-Good events in the sample with the fit result superimposed;

[10] As this sample has no background events that can be used to determine the background PDF parameters, we fix them in this fit to values obtained in the sidebands of the data sample.

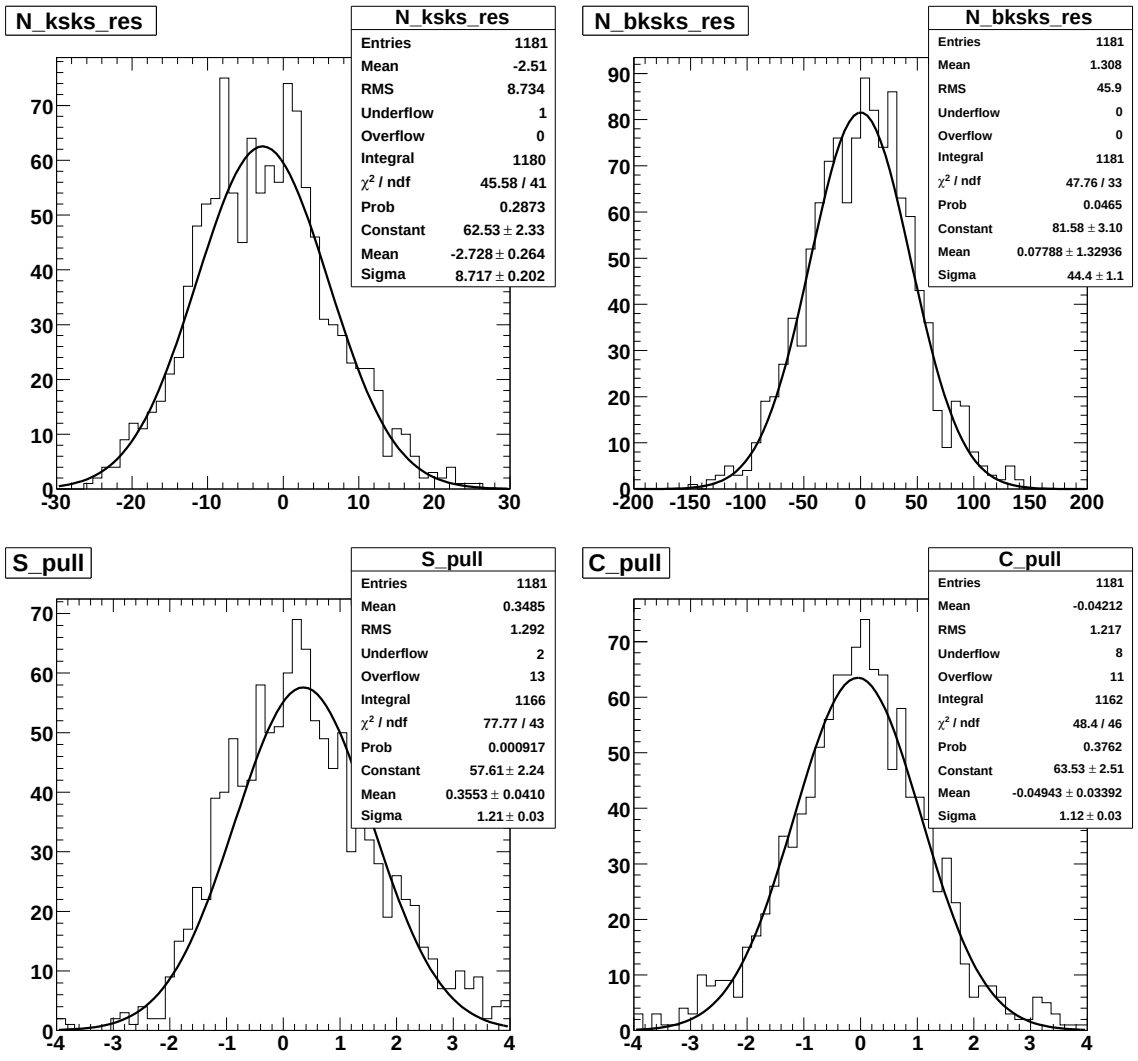

Figure 4.32: Distributions of residuals for the signal yield (upper left) and background yield (upper right) and pull distributions for S (lower left) and C (lower right) in approximately 1000 experiments where the signal events are randomly sampled from the simulated signal MC sample.

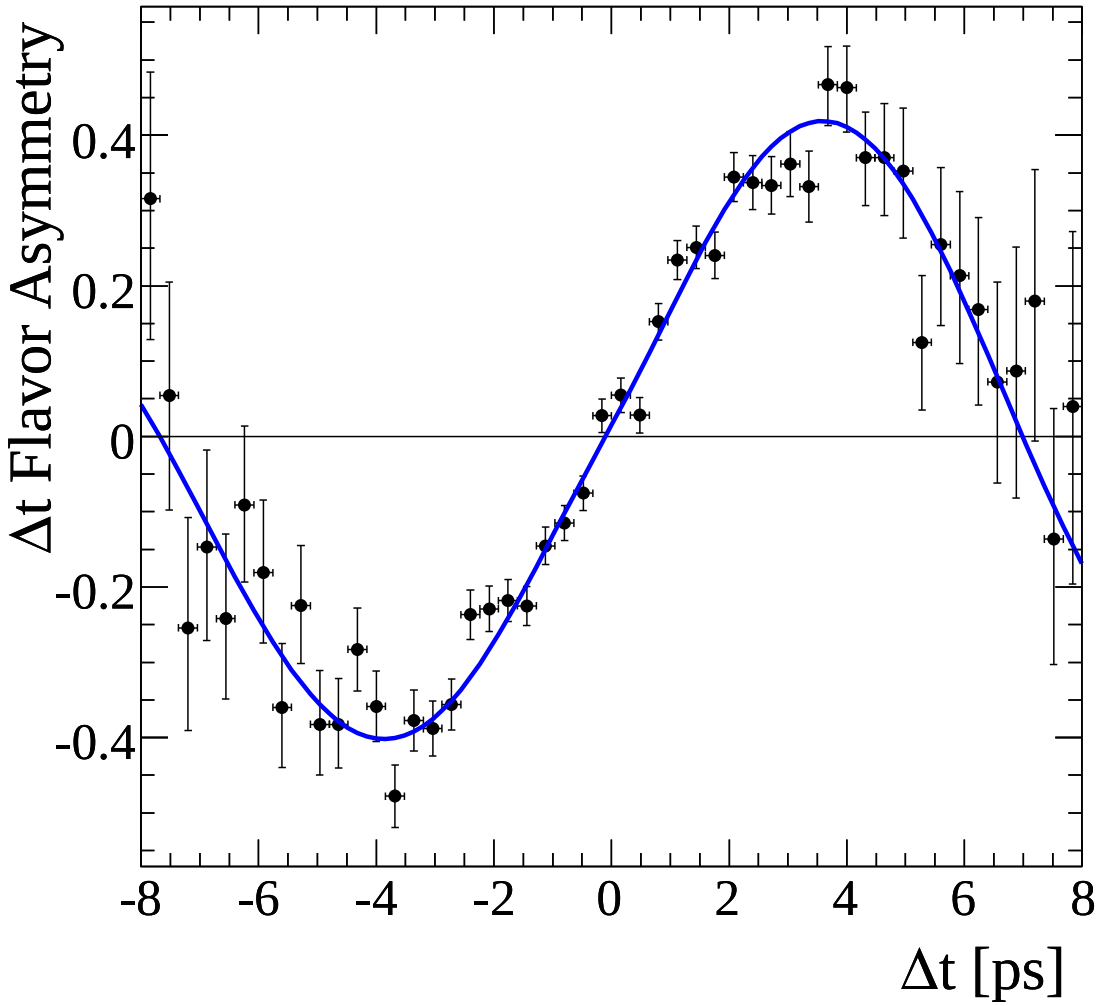

Figure 4.33: Distribution of the flavor asymmetry for the tagged *CP*-Good events in the signal MC sample. The projection of the fitted likelihood function is superimposed.

the large sine term is clearly visible. The result is consistent with the generated values and the Δt PDF is a good fit to the distribution.

Lastly, we also fit the data sample from the 2005 analysis without the Δt PDF and obtain a signal yield consistent with that measurement. We conclude that the fit is sufficiently validated to unblind the data sample.

4.6 Results

The final fit was performed on the sample of 2321 candidates. The results of the fit are the following:

$$\begin{aligned} N_{\rm sig} &= 31.9^{+8.4}_{-7.5} \ \text{events}, \\ N_{\rm bkg} &= 2289 \pm 48 \ \text{events}, \\ S &= -1.28^{+0.80}_{-0.73} \ , \\ C &= -0.40^{+0.41}_{-0.39} \ . \end{aligned}$$

The statistical significance of the signal yield is evaluated by computing the difference in $\ln\mathcal{L}$ between the minimum in the final fit and the minimum in the fit with $N_{\rm sig}$ fixed to zero. Then, $\sqrt{2\Delta\ln\mathcal{L}}$ is a χ^2-like quantity corresponding to the number of standard deviations separating the signal-free hypothesis from the fit result, assuming roughly Gaussian errors. In this fit, the significance is 7.4σ. As this is significantly greater than 5σ, we interpret the result as a clear observation of this decay mode.[11]

Figures 4.34 and 4.35 display the final distributions and fit results of the likelihood variables in the sample. The PDFs track the data well, indicating a good fit. Although the signal is highly significant in the multi-dimensional space of the fit variables, it is difficult to see visually in a one-dimensional projection of any of the variables, as then the discriminating power of the variables not shown is not included. For example, the

[11] 5σ corresponds to the very low probability of 3×10^{-7} that a dataset with no signal would have the distributions of variables in this fit.

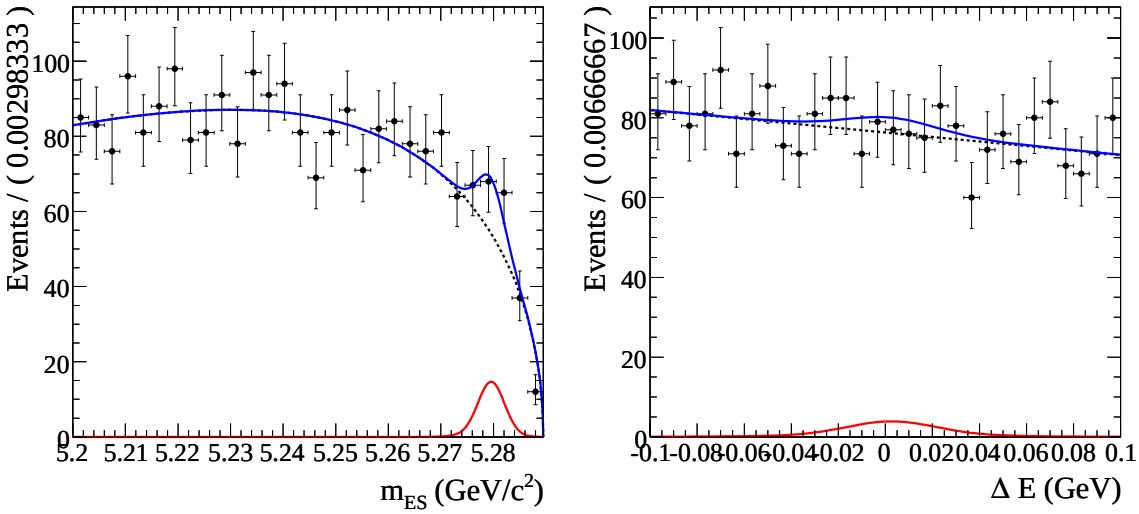

Figure 4.34: Distributions of $m_{\rm ES}$ and ΔE in the data sample (histogram) with the PDF projections overlaid (blue). The signal (red) and background (black dotted) components of the likelihood model are plotted as well.

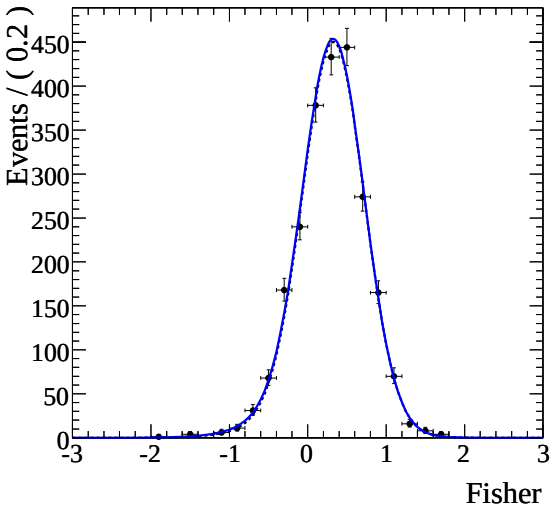

Figure 4.35: The distribution of the Fisher variable in the data sample with the PDF overlaid.

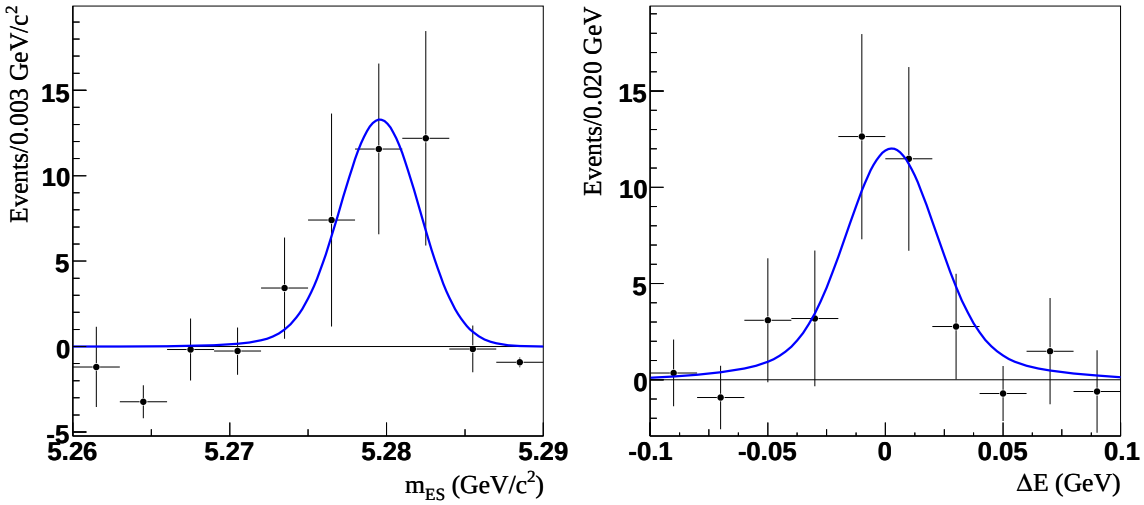

Figure 4.36: Signal sPlots for $m_{\rm ES}$ (top) and ΔE (bottom).

signal peak in $m_{\rm ES}$ is diluted, since that region includes events that are very likely to be background if their value of ΔE and other variables is taken into account.

A simple way to enhance a one-dimensional projection in signal decays is to impose tight selections around the signal region in the variables not shown to suppress background events. We use a more powerful, statistically optimized technique, wherein the PDFs of the variables not shown are used to evaluate the likelihood that each event is signal. The event then receives a fractional weight from zero to one, with one signifying the highest probability of being signal. In this way, the likely background events are suppressed in the one-dimensional histogram using information from all events in the sample, and the resulting distribution, called an sPlot, can be directly compared with the signal PDF. (The histogram is normalized to the signal event yield from the fit. See Ref. [47] for more details.) An analogous procedure can be applied to generate sPlots for the background category, or any other species in the maximum-likelihood fit. Figure 4.36 displays signal sPlots for $m_{\rm ES}$ and ΔE, showing a clear signal peak and a good fit of the PDF to the histogram.

For Δt, we use a simpler method to enhance the projection in signal decays, as it is difficult to construct a $B^0 - \overline{B}^0$ asymmetry sPlot in a statistically consistent

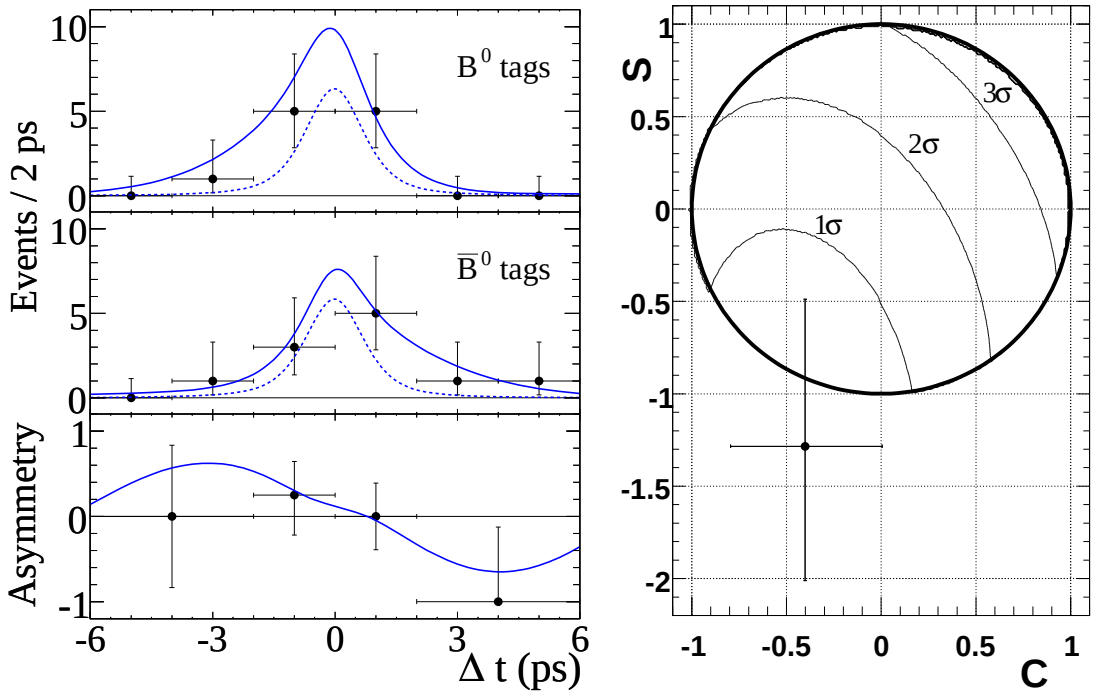

Figure 4.37: Left: distributions of Δt for $B^0 \to K^0_S K^0_S$ decays in data tagged as B^0 (top) or $\overline{B}^0$ (middle), and the asymmetry (bottom). The data is enhanced in signal decays using requirements on probability ratios. The solid curve represents the PDF projection for the sum of signal and background, while the dotted curve shows the contribution from background only. Right: Likelihood contours in the S vs. C plane, where $n\sigma$ corresponds to a change in $-2\ln\mathcal{L}$ of 2.3 for $n = 1$, 6.2 for $n = 2$, and 11.8 for $n = 3$. The circle indicates the physically allowed region, while the point with error bars denotes the result of the fit to data.

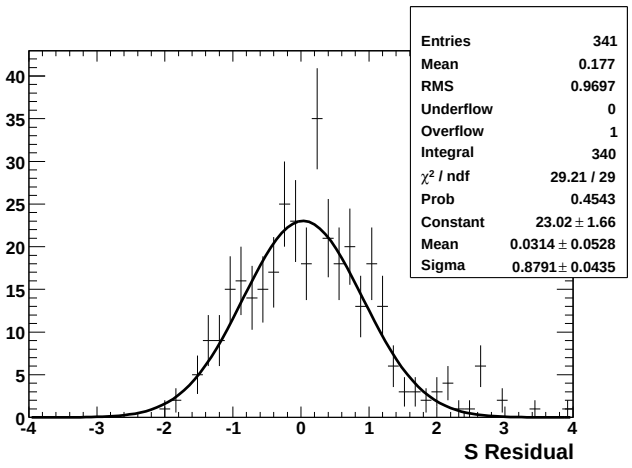

Figure 4.38: The residual of the fitted value of S for events satisfying the requirement $0.7 < \sigma_S < 0.9$ in the toy experiments where S and C are scanned uniformly in the physical region.

manner. Instead of weighting the events, we simply impose a selection on the signal-to-background ratio of PDF values for each event

$$\frac{\mathcal{P}_{\rm sig}}{\mathcal{P}_{\rm sig} + \mathcal{P}_{\rm bkg}}, \tag{4.30}$$

with the selection optimized in toy MC studies to produce the largest signal significance, $N_{\rm sig}/\sqrt{N_{\rm sig} + N_{\rm bkg}}$. The resulting plots include a background component and the overlaid PDF has signal and background yields determined from the toy studies for the PDF-ratio selection. Figure 4.37 shows these projection plots for events with $B_{\rm tag}$ identified as a B^0 and $\overline{B}^0$, as well as the asymmetry. The large negative sine wave responsible for the large value of S is clearly visible, and the PDF projection tracks the data well.

As the fitted value of S is large, we investigate for the presence of a bias, motivated by the previous validation studies. We generate $10,000$ toy experiments with parameters fixed to the values of the data fit and examine the residual distribution of S only in experiments where the fitted error is in the range $0.7 < \sigma_S < 0.9$, which is the range relevant for our fit result. No bias is observed (Fig. 4.38). This is not

surprising, since although the fitted value is unphysical, it still intersects the physical region within one standard deviation. The fit is biased only when the value of S is very unphysical with a very large (though underestimated) error, while the errors on S and C in the fit to data are in the middle of the expected distributions determined in the toy studies (0.8 ± 0.3 for σ_S and 0.6 ± 0.2 for σ_C, see Fig. 4.29). Thus, we observe no evidence of bias and do not correct the fitted value of S.

Figure 4.37 shows the 1σ, 2σ, and 3σ contours of equal likelihood in the physically allowed region of the $S-C$ plane. They are evaluated by calculating changes in $-2\ln\mathcal{L}$ of 2.3, 6.2, and 11.8, respectively, which are two-dimensional analogues of squared one-dimensional standard deviations. As can be seen, areas of the physically-allowed region with large positive values of S are disfavored by this result at a 3σ level. This is a fortuitous result, as the measurement of S is effectively performed with less than 10 signal events, once the fraction of tagged CP-Good signal events and the tagging Q are taken into account.

4.7 Systematic Uncertainties

Although this measurement is completely dominated by statistical uncertainties due to the small size of the signal, several sources of systematic uncertainty are considered. The contributions from all sources are summed in quadrature to determine the final systematic uncertainties on the physical parameters.

4.7.1 PDF Shape and Parameter Values

To evaluate the systematic effect of imperfect PDF modeling two procedures are employed to parameterize the PDFs in alternative ways: different shapes are assumed for some PDFs and the values of the PDF parameters are increased and decreased by their uncertainties. In both cases, the re-parameterized PDF model is used to fit the data sample again and the resulting changes from the nominal fit in the yields,

S, and C are taken to be the systematic uncertainties from that source.

As all the background PDF parameters are floated in the fit, the systematic errors due to their uncertainties are already accounted for in the statistical errors of the fitted yields, S, and C. For the signal $m_{\rm ES}$ PDF we assume an error of 0.4 MeV on the core and tail mean, which is the difference between the data and MC values of the mean in the $K^0_S\pi^+$ analysis. To account for the uncertainty in shape, we parameterize the signal MC distribution with the $m_{\rm ES}$ parameterization used in the $K^0_S\pi^+$ analysis. For the signal ΔE PDF, we vary the parameters by their errors. The errors on the core mean and variance are set to 2.6 MeV and 3 MeV, respectively, which are typical data-MC differences in two-body analyses. For the tail and core fraction we use the difference of their values from the values obtained in the $B^+ \to \overline{K}^0 K^+$ analysis as an estimate of their errors. For the signal Fisher, we use the parameter values obtained in the $B \to K^+\pi^-$ analysis to redo the fit.

For Δt we also vary all signal PDF parameters by their errors. The uncertainties on τ and Δm_d are taken from the PDG [20]. Tables 4.7.1 and 4.7.1 list the systematic contributions of each PDF. The total systematic errors due to PDF parameterization are listed in Table 4.11. In addition, we redo the fit with that combination of the above parameter variations that has the greatest negative effect on the signal yield. With this procedure, we obtain a final signal significance of 7.3σ. As this includes systematic uncertainties, the observation of the signal is highly robust against systematic effects.

4.7.2 Fitter Bias

We assign a symmetric error of 8.6% on the signal yield to account for the effect of the bias detected in the toy MC experiments where the signal was sampled from the signal MC sample. This value corresponds to 2.7 events. As was discussed, no evidence of bias on S and C was found and thus no systematic corrections or uncertainties are assigned.

Source	Value	$\Delta N_{\rm sig}$	ΔS	ΔC
$\boldsymbol{m_{\rm ES}}$				
$\mu_{\rm core}$	5.28 ± 0.0004	$^{0.322}_{-0.54}$	$^{0.0741}_{-0.103}$	$^{0.0228}_{-0.0308}$
$\mu_{\rm tail}$	5.28 ± 0.0004	$^{0.0431}_{-0.103}$	$^{0.00135}_{-0.00241}$	$^{0.000805}_{0}$
$\sigma_{\rm core}$	$0.00251 \pm 1.7e-05$	$^{0.0379}_{-0.104}$	$^{0.00309}_{-0.00408}$	$^{0.000847}_{0}$
$\sigma_{\rm tail}$	0.00417 ± 0.00015	$^{0.00379}_{-0.00604}$	$^{0.00114}_{-0.00104}$	$^{0.00033}_{-0.000317}$
$f_{\rm core}$	0.946 ± 0.0089	$^{0.0694}_{-0.157}$	$^{0.003}_{-0.00505}$	$^{0.00116}_{0}$
Alternate Shape	$B^+ \to K^0\pi^+$	± 0.22	± 0.0129	± 0.0032
$\boldsymbol{\Delta E}$				
μ	$0.0026^{+0.0015}_{-0.0032}$	$^{0.0937}_{-0.127}$	$^{0.0303}_{-0.0202}$	$^{0.0328}_{-0.0162}$
$\sigma_{\rm core}$	0.0188 ± 0.003	$^{0.816}_{-1.02}$	$^{0.0336}_{-0.0856}$	$^{0.0243}_{-0.0487}$
$\sigma_{\rm tail}$	0.0447 ± 0.003	$^{0.105}_{-0.22}$	$^{0.00277}_{-0.00233}$	$^{0.00275}_{-0.00195}$
$f_{\rm core}$	0.76 ± 0.024	$^{0.167}_{-0.275}$	$^{0}_{-0.00222}$	$^{0.000104}_{-0.00114}$
$\boldsymbol{\mathcal{F}}$				
$B^0 \to K^+\pi^-$		± 0.62	± 0.042	± 0.010
Total		$^{+1.12}_{-1.39}$	$^{+0.097}_{-0.142}$	$^{+0.048}_{-0.061}$

Table 4.9: Summary of the absolute systematic uncertainties due to PDF parameterization.

Source	$\Delta N_{\rm sig}$	ΔS	ΔC
Δt	$^{+0.044}_{-0.160}$	$^{+0.031}_{-0.037}$	$^{+0.014}_{-0.0099}$

Table 4.10: Summary of the absolute systematic uncertainties due to Δt PDF parameterization.

Source	$\Delta\ N_{\rm sig}$	$\Delta\ S$	$\Delta\ C$
Total	$^{+1.1}_{-1.4}$	$^{+0.10}_{-0.15}$	$^{+0.050}_{-0.062}$

Table 4.11: Total systematic contribution coming from varying all of the PDF parameters.

4.7.3 Time-Dependent Systematic Effects

Several additional sources of systematic uncertainties on S and C were considered and are discussed in turn.

- SVT alignment – Imperfect alignment of the SVT with respect to the DCH can bias the measurement of the B decay vertices. To account for this effect, the nominal fit is performed on signal MC samples with different generated SVT alignments and the maximum variation in S and C is taken as the systematic error. The errors are 0.0158 on S and 0.0075 on C.

- Tagging – We vary the Δt PDF parameters by their errors and take the resulting changes in S and C as systematic errors.

- Beam-Constrained Vertexing – The systematic effect of the beam-constrained determination of Δt is evaluated by applying this vertexing method to the $B^0 \to J/\psi\, K^0_S$ decay. In that mode, the signal in data is large with little background and Δt is accurately determined by vertexing the B using the two lepton tracks to which the very short-lived J/ψ decays. In this study, the information from the dilepton pair is ignored and the vertex is instead determined from the K^0_S using the same beam-constrained method as in $B^0 \to K^0\overline{K}^0$. Performing this procedure on signal $J/\psi\, K^0_S$ MC and data samples, we extract the scale factor for the core width of the resolution function that corrects for data-MC differences in $\sigma_{\Delta t}$. This scale factor is a measure of the uncertainty of the vertexing method and we refit our $B^0 \to K^0\overline{K}^0$ data sample using the factor to scale the core width in the Δt PDF. The resulting differences in S and C are assigned as symmetric systematic errors. These errors are 0.041 for S and 0.0071 for C.

  We also fit a signal MC sample that was generated with $S = C = 0$ and assign the deviations of the fitted values from zero as additional systematic errors associated with the vertexing procedure. These errors are 0.031 for S and 0.006 for C.

- Tag-side Interference – We account for possible effects of interference with $B_{\rm tag}$ decays that are less suppressed than our signal but share the same quark content. These effects can mimic CP-violating effects without being accounted for by the mistag fractions. Using the method in Ref. [48], the assigned symmetric systematic errors from this source are 0.001 for S and 0.011 for C.

4.7.4 Efficiency

The selection efficiency is determined from the signal MC sample. Systematic uncertainties due to differences in detector acceptance between data and MC must be accounted for in computing the branching fraction.

As the $m_{\rm ES}$ and ΔE selection is assumed to be perfectly efficient, we assign half the difference between unity and its efficiency in the MC sample as a systematic error. The distribution of the sphericity angle is assumed to be uniform in the isotropically distributed signal events. Thus, for our sphericity-angle selection ($|\cos\theta_S| < 0.8$) we expect 80% efficiency. The observed deviation from this value is 4%. Several studies of two-body modes indicate typical data-MC differences of up to 2.5%. We decide to use this value as a systematic error, as it is compatible with 4% and the methods used rely on data.

The efficiency is also corrected for data-MC differences in K^0_S reconstruction and invariant-mass selection. The corrections are calculated by comparing data and MC values of the efficiency of the DCH relative to K^0_S's detected in the SVT that project into the DCH volume. The study is done on a large sample of K^0_S's with momentum and angular distributions similar to this analysis and with the appropriate selections on the invariant mass and decay-time significance.

The total efficiency including all systematic effects and errors is $(8.49 \pm 0.32)\%$.

4.8 Calculation of the Branching Fraction

To extract the $B^0 \to K^0\overline{K}^0$ branching fraction, we relate it to the $K^0_S K^0_S$ yield $N_{\rm sig}$ determined from the fit:

$$\mathcal{B}(B^0 \to K^0\overline{K}^0) = \frac{1}{\mathcal{B}(K^0\overline{K}^0 \to K^0_S K^0_S) \cdot \mathcal{B}(K^0_S \to \pi^+\pi^-)^2} \frac{N_{\rm sig}}{\epsilon \cdot N_{B\overline{B}}}, \tag{4.31}$$

where $N_{B\overline{B}}$ is the number of $B\overline{B}$ pairs in the *BABAR* dataset and ϵ is the nominal $B^0 \to K^0\overline{K}^0$ efficiency. The $\pi^+\pi^-$ decay branching fraction is 0.6895 (PDG value [20]), and $\mathcal{B}(K^0\overline{K}^0 \to K^0_S K^0_S) = 0.5$. These two branching fractions are already included in the total efficiency, $(8.49 \pm 0.32)\%$. This formula has factors of two that cancel out: each of the B mesons in the pair can decay to the $K^0_S K^0_S$ final state, which doubles the denominator, but only half of the $B\overline{B}$ pairs are $B^0\overline{B}^0$ pairs rather than B^+B^- pairs, which cannot produce this final state. The assumption of equal branching fractions is a good approximation [36], as is the assumption of $\mathcal{B}(\Upsilon(4S) \to B\overline{B}) = 1$ [20].

The number of $B\overline{B}$ pairs is estimated by comparing the number of events containing hadrons in on-resonance versus off-resonance data samples relative to the number of dimuon events. As off-resonance data does not contain any $B\overline{B}$ events while the small change in CM energy has a small effect on continuum production, the difference is assumed to come from hadronic $B\overline{B}$ decays. The number of $B\overline{B}$ pairs is computed according to

$$N_{B\overline{B}} = \frac{1}{\epsilon_{B\overline{B}}} \left(N_h^{\rm on} - \frac{N_{\mu\mu}^{\rm on}}{N_{\mu\mu}^{\rm off}} \kappa N_h^{\rm off} \right), \tag{4.32}$$

where $N_h^{\rm on}$ and $N_h^{\rm off}$ are the numbers of hadronic events in each sample; $\epsilon_{B\overline{B}}$ is the efficiency of the hadronic selection on $B\overline{B}$ events ($\approx 96\%$); κ (≈ 1) is a correction factor accounting for the small differences in continuum cross-section and efficiencies at the two energies; and the ratio $N_{\mu\mu}^{\rm on}/N_{\mu\mu}^{\rm off}$ is a normalization relating the difference in integrated luminosity between the two samples. The efficiencies of the hadronic selection have been determined in carefully tuned simulated MC samples. The estimated

$N_{\rm sig}$	Signif.	$\mathcal{B}\,(10^{-6})$	S	C
$31.9\ ^{+8.4}_{-7.5} \pm 3.0$	7.3σ	$1.08\ ^{+0.28}_{-0.25} \pm 0.11$	$-1.28\ ^{+0.80}_{-0.73}\ ^{+0.11}_{-0.16}$	$-0.40\ ^{+0.41}_{-0.39}\ ^{+0.052}_{-0.064}$

Table 4.12: Summary of results for $B^0 \to K^0\overline{K}^0$. We show the central fit values for the signal yield $N_{\rm sig}$ and CP-violating parameters S and C, the signal-yield significance (including systematic uncertainties), and the measured branching fraction $\mathcal{B}$. The first errors are statistical and the second are systematic.

number is $(347.5 \pm 3.8 \pm 0.1) \times 10^6$ $B\overline{B}$ pairs.

The final result is $\mathcal{B}(B^0 \to K^0\overline{K}^0) = (1.08\ ^{+0.28}_{-0.25} \pm 0.11) \times 10^{-6}$.

4.9 Summary of $B^0 \to K^0\overline{K}^0$

Our final results are summarized in Table 4.12. We have observed the $B^0 \to K^0\overline{K}^0$ decay at greater than 7σ significance, which constitutes a clear observation of a gluonic $b \to d$ penguin-dominated mode. The branching fraction is at the level predicted by theory [27, 49]. In addition, we have performed the first time-dependent CP-violation measurement in a $b \to d$ penguin-dominated mode and have excluded large positive values of S at greater than 3σ significance. More data is needed to verify this exclusion with greater confidence and to make more meaningful comparisons with theoretical predictions. Increased datasets will also allow a more precise comparison with theory on the branching fraction result. This result has been published in the journal Physical Review Letters [50]. The Belle collaboration recently reported a similar observation of this mode that is consistent with this result, although no time-dependent CP-violation measurement was performed [51].

Chapter 5

Analysis of $B^+ \to \overline{K}^0 K^+$ and $B^+ \to K^0 \pi^+$

5.1 Overview

The $B^+ \to \overline{K}^0 K^+$ decay is similar to the $B^0 \to K^0 \overline{K}^0$ decay discussed in the previous chapter. It proceeds through the same $b \to d$ penguin diagram, except that the spectator quark is a u quark from a B^+ meson rather than a d quark from a B^0 meson. Thus, although the annihilation amplitude discussed earlier could have an effect, we expect the branching fraction to be roughly at the same level. Charged B mesons do not mix, as electric charge is a quantum number conserved by all known interactions. Hence, there is no interference effect in the time evolution of the B^+B^- system. However, this mode is self-tagged: the charge of the kaon unambiguously identifies the flavor of the parent B meson. Thus, a direct CP asymmetry between B^+ and B^- decays is measured.

The topology of the decay is also similar to $B^0 \to K^0 \overline{K}^0$: the final state contains two high-energy particles with the same momentum and angular distributions. The K^0 is detected through the $K^0 \to K^0_S \to \pi^+\pi^-$ mode in a manner and for reasons identical to the previous analysis. However, the high-energy kaon is detected as a

charged track in the detector, making this decay very similar to the $B^+ \to K^0\pi^+$ process where the high-energy track is a pion. For this reason, both of these decays are analyzed together, using the DIRC to separate pion and kaon candidates.

$B^+ \to K^0\pi^+$ proceeds mainly through a $b \to s$ penguin diagram and its branching fraction and direct CP asymmetry are useful for comparison with other $B \to K\pi$ modes. Its branching fraction is a factor of ten larger than $\mathcal{B}(B^+ \to \overline{K}^0 K^+)$, making it difficult to extract the latter, rare signal. However, with the larger signal size it is possible to extract the shapes of the distributions of discriminating variables directly from data. As the modes have similar distributions, constraining the $B^+ \to \overline{K}^0 K^+$ signal to $B^+ \to K^0\pi^+$ PDFs decreases our reliance on MC simulation.

5.1.1 Analysis Strategy

The analysis is almost the same as the $B^0 \to K^0\overline{K}^0$ analysis. Selection of K^0_S candidates is exactly the same, while additional requirements are imposed on the high-energy kaon and pion candidates. As no time-dependent measurement is performed, the vertex of the B candidates is not computed. Using the same variables, an unbinned maximum likelihood fit is performed to separate the $K^0_S K^+$ and $K^0_S\pi^+$ signals from the continuum background and to measure charge asymmetries. $B\overline{B}$ backgrounds are negligible. The analysis is done in a blind manner.

5.1.2 Separating Pions from Kaons

Separating $B^+ \to K^0\pi^+$ from $B^+ \to \overline{K}^0 K^+$ decays involves distinguishing pions from kaons, which is difficult for high-energy two-body tracks. The main source of pion-kaon separation is the measured Cherenkov angle θ_C in the DIRC, which is distributed differently for kaons and pions due to their different masses (Fig. 3.13).

For each track, we define a pull for this quantity

$$Pull(\theta_C) = \frac{\theta_C - \theta_C^{\rm Exp}}{\sigma_{\theta_C}}, \tag{5.1}$$

where $\theta_C^{\rm Exp}$ is the expected Cherenkov angle based on the momentum of the track and σ_{θ_C} is the uncertainty on the measured value of θ_C. As $\theta_C^{\rm Exp}$ is different for pions and kaons, we define separate PDFs of the pull for the positive and negative pions and kaons and use them in the maximum-likelihood fit to separate the species. (The PDFs are split by charge as the DIRC has a slightly different response to positively and negatively charged particles.) The PDFs are calibrated using a control sample of fully reconstructed $D^{*+} \to D^0\pi^+(D^0 \to K^-\pi^+)$ decays [52], as in this final state the two tracks with the same charge can be unambiguously identified as pions while the other track with the opposite charge is definitely a kaon.

Additional separation is provided by the ΔE variable. As PID information is not used until the fit is performed, each track is initially assigned the pion mass for the computation of energy-like variables from the measured momentum. Since $E^2 = p^2 + m^2$, this leads to a momentum-dependent shift in the ΔE value for final states that include charged kaons. As a result, the $B^+ \to \overline{K}^0K^+$ ΔE PDF is shifted by about 45 MeV toward negative values with respect to the $B^+ \to K^0\pi^+$ PDF, providing additional PID discrimination in the maximum likelihood fit.

5.2 Dataset

This analysis uses the same *BABAR* dataset as $B^0 \to K^0\overline{K}^0$: 347 million $B\overline{B}$ pairs. In addition, 288,000 simulated $B^+ \to \overline{K}^0K^+$ events and 288,000 simulated $B^+ \to K^0\pi^+$ events are used for MC studies.

5.3 Reconstruction and Selection

The analysis uses the same K^0_S selection as in the previous chapter. B candidates are reconstructed from a K^0_S candidate and a track satisfying the following criteria:

- The track must be within the DIRC acceptance and must have a well measured θ_C;
- The DIRC signal must contain more than five photons;
- θ_C must be within four standard deviations from either the pion or kaon expected value at the track's momentum.

These assure that the PID information is accurate, while the 4σ outlier selection rejects proton tracks. Contributions from electron or muon tracks are negligible in this decay mode. The B meson is not vertexed and its four-momentum is determined by simply adding the four-momenta of the K^0_S candidate and the track. The following selections are imposed to reject backgrounds:

- At least three charged tracks must be found in the event;
- $R_2 < 0.95$ and sphericity > 0.01;
- $|\cos\theta_S| < 0.8$;
- $5.2 < m_{\rm ES} < 5.2895\,{\rm GeV}/c^2$;
- $-0.115 < \Delta E < 0.075\,{\rm GeV}$.

The criteria are the same as in $B^0 \to K^0\overline{K}^0$ except that the ΔE selection is asymmetrical and extended to negative values to account for the shift of 45 MeV in $B^+ \to \overline{K}^0 K^+$ events due to the pion-mass hypothesis.

We use signal Monte Carlo samples to estimate the efficiency of each selection. A summary of relative efficiencies for both decay channels is given in Table 5.1. Systematic uncertainties and corrections due to imperfect modeling of K^0_S and track

Cut	Efficiency $K^0_S\pi^+$	Efficiency $K^0_S K^+$
Reconstruction, three tracks,		
R_2, Sphericity	$64.11 \pm 0.08\%$	$62.46 \pm 0.08\%$
$\lvert\cos\theta_S\rvert < 0.8$	$76.24 \pm 0.09\%$	$76.72 \pm 0.09\%$
$(M - M^0_K) < 11.2\,\mathrm{MeV}/c^2$	$94.54 \pm 0.05\%$	$94.44 \pm 0.06\%$
Decay-Time Significance > 5	$97.218 \pm 0.039\%$	$97.263 \pm 0.041\%$
0.1 rad $< \theta_c <$ 1 rad	$90.55 \pm 0.07\%$	$90.56 \pm 0.07\%$
$n_\gamma > 5$	$97.987 \pm 0.036\%$	$97.513 \pm 0.042\%$
DIRC outliers	$98.784 \pm 0.028\%$	$98.681 \pm 0.031\%$
ΔE and $m_{\rm ES}$	$96.362 \pm 0.048\%$	$96.278 \pm 0.052\%$
all previous cuts	$37.94 \pm 0.08\%$	$36.93 \pm 0.08\%$

Table 5.1: Efficiencies of selection criteria for $B^+ \to \overline{K}^0 K^+$ and $B^+ \to K^0\pi^+$ events as determined from the signal MC samples.

Nominal Value (from MC)	$37.94 \pm 0.08\%$	$36.93 \pm 0.08\%$
correction factor	$K^0_S\pi$	$K^0_S K$
$\lvert cos(\theta_S)\rvert$	$1.00 \pm 0 \pm 0.025$	$1.00 \pm 0 \pm 0.025$
track reconstruction	$1.000 \pm 0 \pm 0.007$	$1.00 \pm 0 \pm 0.007$
K^0_S reconstruction	0.995 ± 0.006	0.994 ± 0.006
K^0_S invariant mass cut	$0.994 \pm 0 \pm 0.006$	$0.9941 \pm 0 \pm 0.006$
$\mathcal{B}(K^0 \to K^0_S)$	50	50
$\mathcal{B}(K^0_S \to \pi\pi)$	$68.95 \pm 0 \pm 0.14$	$68.95 \pm 0 \pm 0.14$
Corrected Value	$12.93 \pm 0.09 \pm 0.35\%$	$12.58 \pm 0.09 \pm 0.34\%$

Table 5.2: Corrections applied to the efficiencies.

reconstruction are performed in an analogous manner to the $B^0 \to K^0\overline{K}^0$ analysis and are shown in Table 5.2. The final efficiencies are $12.93 \pm 0.36\%$ for the $K^0_S\pi^+$ channel and $12.58 \pm 0.35\%$ for the $K^0_S K^+$ channel.

We studied exclusive MC samples to determine the contamination from the $K^*\pi$, K^*K, $K^0_S\rho$, $K^0_S f$, $K^0_S\pi^0$, $K^0_S K\pi$, $K^0_S KK$, and $K^0_S\pi\pi$ modes. We expect 11 events in the signal region from these sources (Table 5.3), with less than 1 event contributing to the $K^0_S K$ background due to the presence of a charged kaon in the final state. Additional studies of charmless MC samples and the ΔE sideband also indicate contamination of less than 20 events. Thus, we neglect $B\overline{B}$ backgrounds in this analysis.

Mode	Efficiency	$\mathcal{B}(B \to$Final State)	Expected Yield
$K^0_S\pi^0$	9.137×10^{-5}	3.83×10^{-6}	1.40×10^{-1}
$K^0_S\rho^+$ $(\rho^+ \to \pi^+\pi^0)$	1.168×10^{-3}	1.61×10^{-5}	7.47
$K^{*+}\pi^-$ $(K^{*+} \to K^0_S\pi^+)$	1.209×10^{-3}	1.44×10^{-6}	1.05
$K^{*0}\pi^-$ $(K^{*0} \to K^0_S\pi^0)$	1.209×10^{-3}	2.18×10^{-6}	5.73×10^{-1}
$K^{*+}K^-$ $(K^{*+} \to K^0_S\pi^+)$	3.427×10^{-4}	2.23×10^{-7}	3.05×10^{-2}
$K^{*0}K^-$ $(K^{*0} \to K^0_S\pi^0)$	3.427×10^{-4}	3.87×10^{-7}	8.05×10^{-2}
$K^{*0}K^0_S$ $(K^{*0} \to K^+\pi^-)$	3.427×10^{-4}	5.86×10^{-7}	5.79×10^{-2}
$K^{*+}K^0_S$ $(K^{*+} \to K^+\pi^0)$	3.427×10^{-4}	5.86×10^{-7}	8.05×10^{-2}
$K^0_SK^+\pi^-$	1.399×10^{-5}	6.00×10^{-6}	3.36×10^{-2}
$K^0_SK^+\pi^0$	1.399×10^{-5}	8.00×10^{-6}	4.47×10^{-2}
$K^0_SK^+K^-$	1.399×10^{-5}	8.23×10^{-6}	4.47×10^{-2}
$K^0_S\pi^+\pi^0$	1.399×10^{-5}	2.20×10^{-5}	1.23×10^{-1}
$K^0_S\pi^+\pi^-$	1.399×10^{-5}	1.49×10^{-5}	8.36×10^{-2}
$K^0_S\rho^0$ $(\rho^0 \to \pi^+\pi^-)$	1.811×10^{-3}	1.86×10^{-6}	1.35
$K^0_Sf_0$ $(f_0 \to \pi^+\pi^-)$	6.045×10^{-4}	1.02×10^{-6}	2.47×10^{-1}
		Total Yield	11.4 events

Table 5.3: Expected yields of exclusive $B\overline{B}$ background in $350\,\mathrm{fb}^{-1}$.

After all selection criteria, the data sample contains $30,159$ candidate decays.

5.4 The Fit and PDF Parameterization

The unbinned maximum likelihood fit has four signal categories: $K^0_S\pi^+$, $K^0_S\pi^-$, $K^0_SK^+$, and $K^0_SK^-$; and four corresponding background categories. The likelihood for a single event is given by

$$\begin{aligned}
\mathcal{L} &= N_{K^0_S\pi}\left(1-\mathcal{A}_{K^0_S\pi}\right)\mathcal{P}^{K^0_S\pi^+} + N_{\mathrm{b}K^0_S\pi}\left(1-\mathcal{A}_{bK^0_S\pi}\right)\mathcal{P}^{bK^0_S\pi^+} \\
&+ N_{K^0_S\pi}\left(1+\mathcal{A}_{K^0_S\pi}\right)\mathcal{P}^{K^0_S\pi^-} + N_{\mathrm{b}K^0_S\pi}\left(1+\mathcal{A}_{bK^0_S\pi}\right)\mathcal{P}^{bK^0_S\pi^-} \\
&+ N_{K^0_SK}\left(1-\mathcal{A}_{K^0_SK}\right)\mathcal{P}^{K^0_SK^+} + N_{\mathrm{b}K^0_SK}\left(1-\mathcal{A}_{bK^0_SK}\right)\mathcal{P}^{bK^0_SK^+} \\
&+ N_{K^0_SK}\left(1+\mathcal{A}_{K^0_SK}\right)\mathcal{P}^{K^0_SK^-} + N_{\mathrm{b}K^0_SK}\left(1+\mathcal{A}_{bK^0_SK}\right)\mathcal{P}^{bK^0_SK^-},
\end{aligned} \tag{5.2}$$

where the event yields for the eight categories have been parameterized in terms of the charge-summed event yields

$$N_{K^0_S h} \equiv N_{K^0_S h^+} + N_{K^0_S h^-}$$

and the direct CP asymmetries

$$\mathcal{A}_{K^0_S h} \equiv \frac{N_{K^0_S h^-} - N_{K^0_S h^+}}{N_{K^0_S h^-} + N_{K^0_S h^+}}, \tag{5.4}$$

where $h = K,\ \pi$. The corresponding background parameters are indicated with a "b". For a category k, the PDF is given by

$$\mathcal{P}^k = \mathcal{P}^k(m_{\rm ES})\mathcal{P}^k(\Delta E)\mathcal{P}^k(\mathcal{F})\mathcal{P}^k(\theta_C, |\mathbf{p}_h|), \tag{5.5}$$

where $\mathbf{p}_h$ is the momentum of the high-energy track. To determine the asymmetries, the fit essentially counts the number of positively and negatively charged final states, taking into account any correlations with other parameters. The physical parameters determined by the fit are the four charge-summed event yields and the four corresponding direct CP asymmetries. The PDFs are parameterized from MC samples and data whenever possible.

5.4.1 $m_{\rm ES}$

We parameterize the signal $m_{\rm ES}$ PDF in the $K^0_S\pi^+$ and $K^0_S K^+$ channels with an asymmetric Gaussian modified to include longer tails:

$$\begin{aligned}
\mathcal{P}(m_{\rm ES}) &= \exp\left(-\frac{(m_{\rm ES}-\mu)^2}{2\sigma_L^2 + \alpha_L(m_{\rm ES}-\mu)^2}\right) \quad m_{\rm ES} \le \mu \\
\mathcal{P}(m_{\rm ES}) &= \exp\left(-\frac{(m_{\rm ES}-\mu)^2}{2\sigma_R^2 + \alpha_R(m_{\rm ES}-\mu)^2}\right) \quad m_{\rm ES} > \mu,
\end{aligned} \tag{5.6}$$

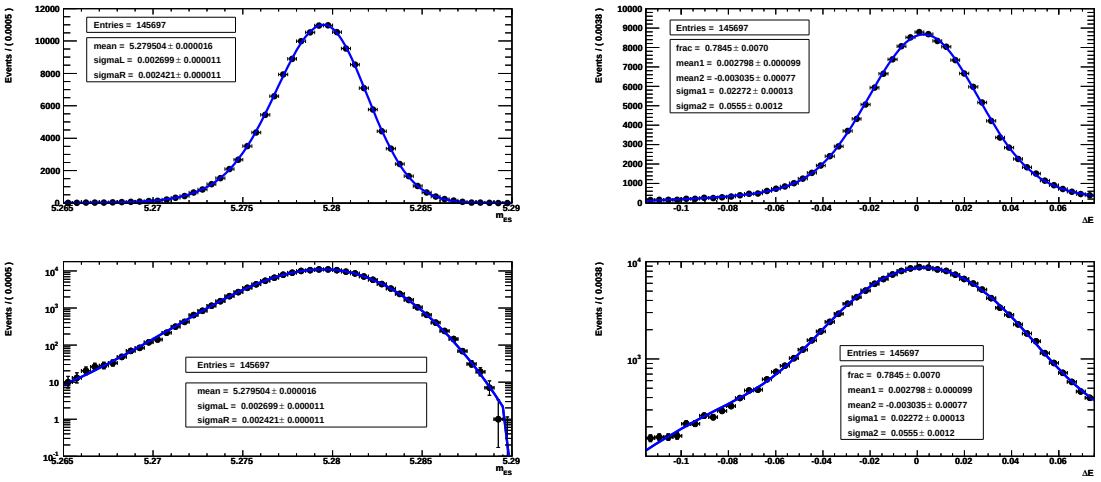

Figure 5.1: m_{ES} (left) and ΔE (right) distributions for $B^{\pm} \to K^0_S\pi^{\pm}$ Monte Carlo events with the fitted PDFs overlaid (blue lines). Bottom plots are on a logarithmic scale to show agreement in the tails.

where $\alpha_{L,R}$ determine the size of the left and right tails, respectively. Studying the $K^0_S\pi^+$ MC sample, we obtain the best fit to the distribution by fixing α_L to 0.07, while α_R is fixed to 0 since there is no tail toward higher values of $m_{\rm ES}$ close to the kinematic cut-off. The left plots in Figs. 5.1 and 5.2 show how the tails are well described by this functional form for both modes. As there are no significant differences in the $m_{\rm ES}$ PDFs between the two modes, we use the same PDF for both. We float the mean μ in the fit to data, as we have enough $K^0_S\pi^+$ signal events (~ 1000) to determine the peak position from data. We conservatively fix the other parameters to the values obtained from the $K^0_S\pi$ signal MC sample. For later systematic studies, we assign an error of $\pm 0.2\,{\rm MeV}/c^2$ to the widths, which is a typical difference between data and MC in two-body analyses for this functional form.

The $m_{\rm ES}$ PDF for the continuum background is parameterized with the same ARGUS threshold function as in $B^0 \to K^0\overline{K}^0$ (left plot in Fig. 5.3). The shape parameter ξ is floated in the fit to data.

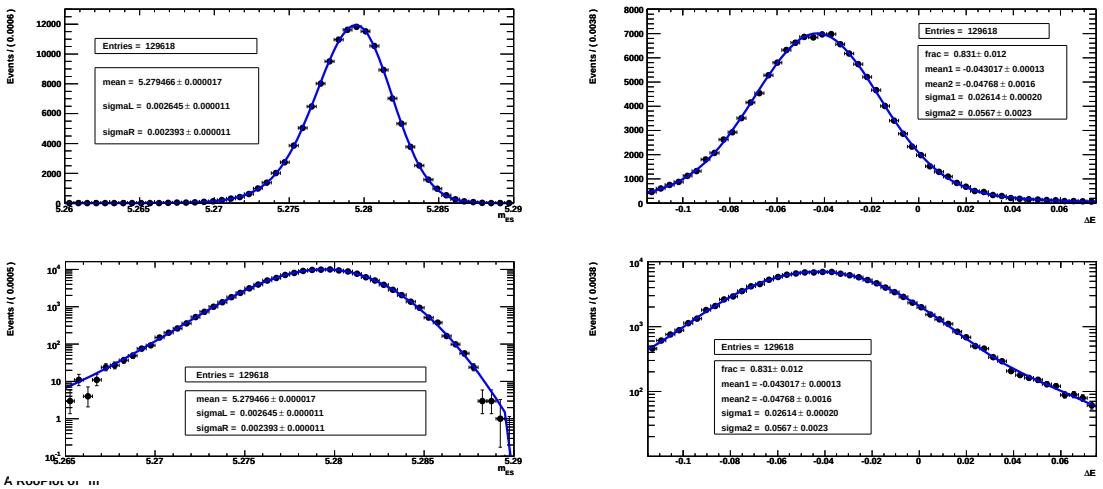

Figure 5.2: m_{ES} (left) and ΔE (right) distributions for $B^{\pm} \to K^0_S K^{\pm}$ Monte Carlo events with the fitted PDFs overlaid (blue lines). Bottom plots are on a logarithmic scale to show agreement in the tails.

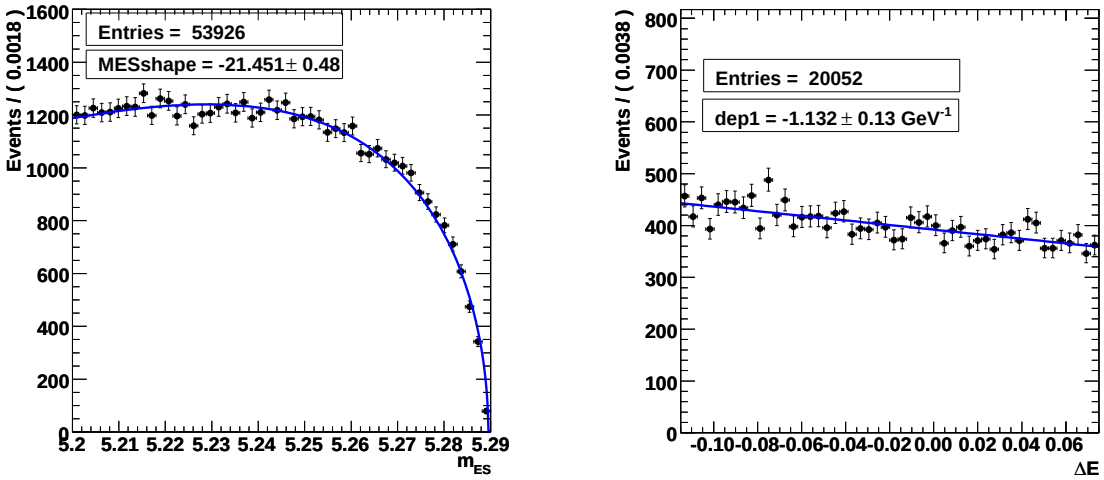

Figure 5.3: m_{ES} (left) and ΔE (right) distributions for continuum background. The m_{ES} plot is made in the ΔE sidebands in the data sample, whereas the ΔE plot is made in the m_{ES} sideband. The blue curves are the fitted PDFs.

5.4.2 ΔE

We model the signal PDF as a double-Gaussian shape (right plots in Figs. 5.1 and 5.2). The wider Gaussian describes the radiative tail on the negative side of the distribution, which is due to the energy that is lost by the high-energy track through final-state radiation. The fraction of the tail Gaussian is about 22% and all the

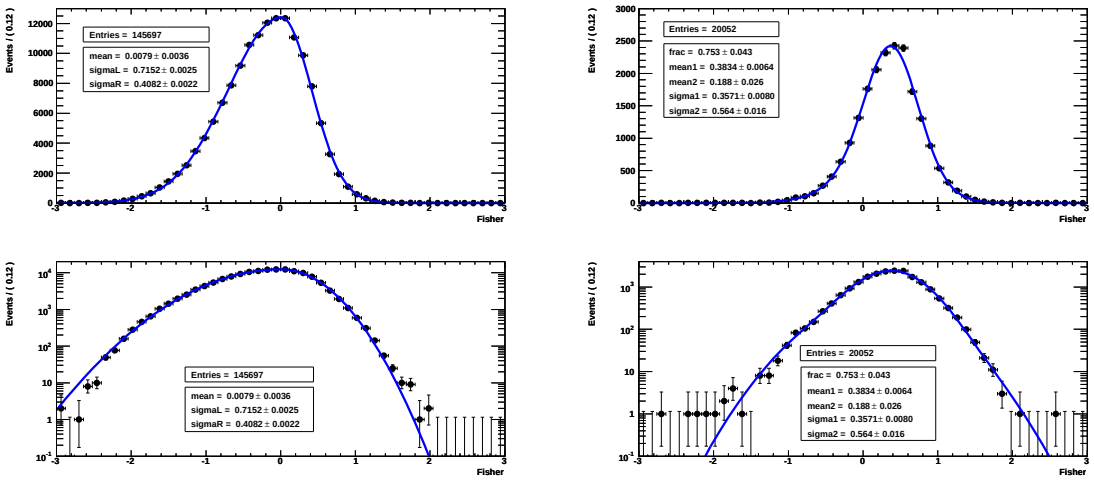

Figure 5.4: Distributions of the Fisher variable for signal $B^+ \to K^0\pi^+$ Monte Carlo events (left) and for background in the m_{ES} sideband of the data sample (right). The blue curves are the fitted PDFs. Bottom plots are on a logarithmic scale to show agreement in the tails.

parameters of the distribution, except the mean of the core Gaussian are taken from the $K^0_S\pi^+$ signal Monte Carlo sample. The core mean has a positive shift in the MC sample of about 3.4 MeV as discussed in the previous chapter. As there is no evidence of such a positive shift in data, we float the mean in the fit, since we have enough statistics to constrain this parameter. The tail mean is fixed to be $(\mu_{\rm core} - 5.8)$ MeV, where the -5.8 MeV offset is taken from the signal MC sample. The ΔE distribution in $K^0_S K$ is the same as in $K^0_S\pi$ except for the momentum-dependent shift due to the pion-mass hypothesis that offsets the distribution by about 45 MeV in the negative direction.

The background PDF is parameterized as a first-order polynomial and the slope is floated in the fit (right plot in Fig. 5.3).

5.4.3 $\mathcal{F}$

The signal Fisher PDF is parameterized using an asymmetrical Gaussian function (Fig. 5.4). We use the same PDF for both modes, as the two distributions have the same shape. The background PDF is modeled with a double Gaussian function (right

Parameter	π^+	π^-	K^+	K^-
μ_1	0.000	0.001	-0.010	-0.012
μ_2	-0.303	-0.359	0.299	0.314
σ_1	0.966	0.966	0.950	0.946
σ_2	2.415	2.372	2.178	2.246
f_1	0.974	0.972	0.962	0.961

Table 5.4: Summary of the double Gaussian parameters in the θ_C PDFs.

m_{ES} $K^0_S\pi^+$ Gaussian with tails	μ floated	$\sigma_R = 2.421 \pm 0.011\,\text{MeV}$
	$\sigma_{\text{L}} = 2.699 \pm 0.011\,\text{MeV}$	$\alpha_{\text{L}} = 0.0700 \pm 0.0011$
	$\alpha_R = 0$	
m_{ES} $K^0_S K^+$	same as $K^0_S\pi^+$	
ΔE $K^0_S\pi^+$ Double Gaussian	μ_{core} floated	$\Delta\mu_{\text{tail}} = -5.8 \pm 0.8\,\text{MeV}$
	$\sigma_{\text{core}} = 22.72 \pm 0.13\,\text{MeV}$	$\sigma_{\text{tail}} = 55.5 \pm 1.2\,\text{MeV}$
	$f_{\text{core}} = 0.784 \pm 0.007$	
ΔE $K^0_S K^+$	same as $K^0_S\pi^+$ with μ_{core} and μ_{tail} dependent on p_{K^+}	
$\mathcal{F}$ $K^0_S\pi^+$ Asymmetric Gaussian	Parameters floated in the fit	
$\mathcal{F}$ $K^0_S K^+$	same as $K^0_S\pi^+$	

Table 5.5: Parameter values for signal PDFs.

m_{ES}, ARGUS	ξ floated in the fit
ΔE, 1^{st} Order Polynomial	Slope floated in the fit
$\mathcal{F}$ Double Gaussian	Floated in the fit

Table 5.6: Parameter values for background PDFs.

plot in Fig. 5.4). The parameters of both distributions are floated in the fit.

5.4.4 DIRC

The Cherenkov-angle pull PDFs, which are momentum-dependent, are parameterized as double Gaussians separately for positive and negative pions and kaons. The parameters are determined from the D^* control sample and are shown in Table 5.4.4 [52].

Signal $K^0_S\pi$ yield
Signal $K^0_S K$ yield
Signal $A_{K^0_S\pi}$
Signal $A_{K^0_S K}$
Background $K^0_S\pi$ yield
Background $K^0_S K$ yield
Background $A_{K^0_S\pi}$
Background $A_{K^0_S K}$
Signal $m_{\rm ES}$ mean μ
Signal ΔE 2G Gaussian $\mu_{\rm core}$
Signal Fisher bifurcated Gaussian (μ, $\sigma_{\rm L}$, $\sigma_{\rm R}$)
Background $m_{\rm ES}$ Argus shape
Background ΔE slope
Background Fisher 2G ($\mu_{\rm core}$, $\mu_{\rm tail}$, $\sigma_{\rm core}$, $\sigma_{\rm tail}$, and $f_{\rm core}$)

Table 5.7: The 20 parameters floated in the final fit. "2G" stands for "double Gaussian".

Sample	$N_{K^0_S\pi}$	$N_{K^0_S K}$	$N_{{\rm b}K^0_S\pi}$	$N_{{\rm b}K^0_S K}$
$K^0_S\pi^+$ MC	$119,350 \pm 346$	375 ± 27	208 ± 20	16 ± 7
$K^0_S K^+$ MC	128 ± 19	$129,434 \pm 360$	23 ± 6	34 ± 9
lower sideband	171 ± 29	25 ± 20	$19,333 \pm 145$	13091 ± 121
upper sideband	-54 ± 12	3 ± 140	$12,053 \pm 89$	9304 ± 115

Table 5.8: Event yields determined by fits to signal Monte Carlo samples and sideband events in data.

5.4.5 PDF Summary

The PDF shapes and parameters used in the likelihood fit are summarized in Tables 5.4.4-5.6, while Table 5.4.4 lists all the parameters floated in the final fit.

5.5 Validation of the Fit

The validation of the fit is done with the procedures introduced in the previous chapter. We fit the $B^+ \to K^0\pi^+$ and $B^+ \to \overline{K}^0 K^+$ signal MC samples, which contain $119,948$ and $129,619$ events, respectively, after all selection criteria have been applied, and are generated with no direct CP asymmetries. In these fits, the background

Sample	$\mathcal{A}_{K^0_S\pi}$ (%)	$\mathcal{A}_{K^0_SK}$ (%)	$\mathcal{A}_{bK^0_S\pi}$ (%)	$\mathcal{A}_{bK^0_SK}$ (%)
$K^0_S\pi$	0.39 ± 0.29	-	-	-
K^0_SK	-	-0.76 ± 0.28	-	-
lower sideband	-	-	0.46 ± 0.75	0.42 ± 0.92
upper sideband	-	-	1.2 ± 0.7	-0.36 ± 1.7

Table 5.9: Direct CP asymmetries determined by fits to signal Monte Carlo samples and sideband events in data.

PDF parameters are fixed to the sideband values in data. We also fit the lower and upper ΔE sidebands, which contain only background events. The lower sideband is $-0.3 < \Delta E < -0.115\,\text{GeV}$ and the upper sideband is $0.075 < \Delta E < 0.260\,\text{GeV}$. In the lower sideband, we expect a small $B\overline{B}$ contribution from multi-body final states where one or more particles was not included in the reconstruction of the signal B, leading to a lower B-candidate energy relative to the beam energy. Thus, these fits determine the level at which these backgrounds are misidentified as signal. As the ΔE shape is different in the sidebands, we do not use ΔE in these fits. Table 5.8 demonstrates that the fitter is able to find signal events with less than 1% of "crossfeed" where $K^0_S\pi^+$ is misidentified as $K^0_SK^+$ or vice versa. In the sidebands, background is misidentified as signal at a level of only 0.1%. Table 5.9 shows the fitted values of the direct CP asymmetries, indicating small deviations from zero that will be discussed later in the discussion of systematic effects.

We also use toy Monte Carlo pseudo-experiments to test the fit. The 2005 *BABAR* analysis reported 744 $B^+ \to K^0\pi^+$ and 41 $B^+ \to \overline{K}^0K^+$ events. Scaling these results to the accumulated luminosity for this analysis, we generate on average 1270 $K^0_S\pi$ and 70 K^0_SK signal events, 19,134 $K^0_S\pi$ and 14,427 K^0_SK background events, and $A_{K^0_S\pi} = -0.09$ and $A_{K^0_SK} = -0.15$. (The asymmetry values are also taken from the 2005 analysis.) As the DIRC PDFs depend on the momentum of the track, we take care to accurately generate the momentum distributions of the charged kaons and pions according to two-body kinematics, where the angles and momenta of the two particles are highly correlated in the boosted lab frame.

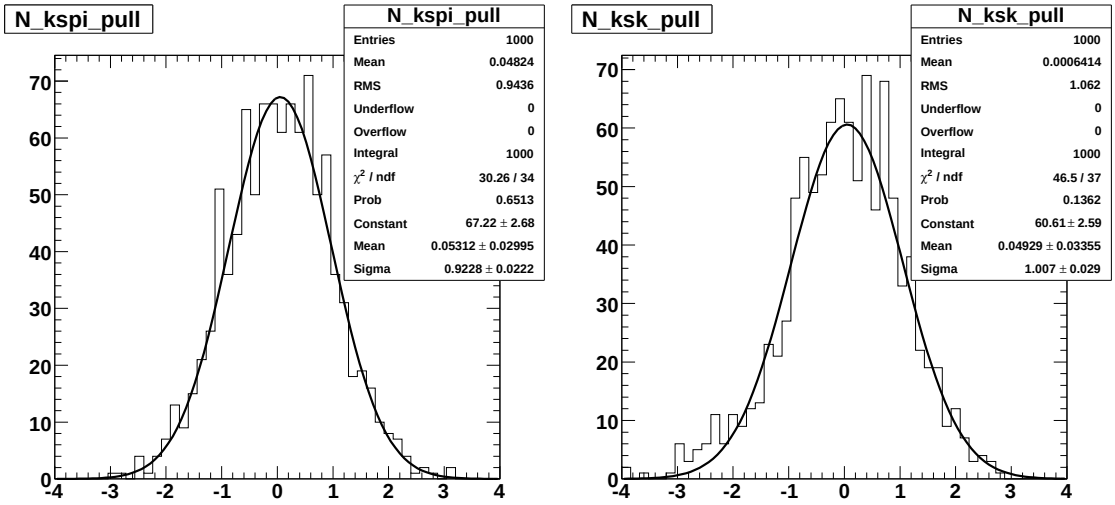

Figure 5.5: Pull plots for the $B^+ \to K^0\pi^+$ (left) and $B^+ \to \overline{K}^0 K^+$ (right) signal yields in 1000 toy experiments.

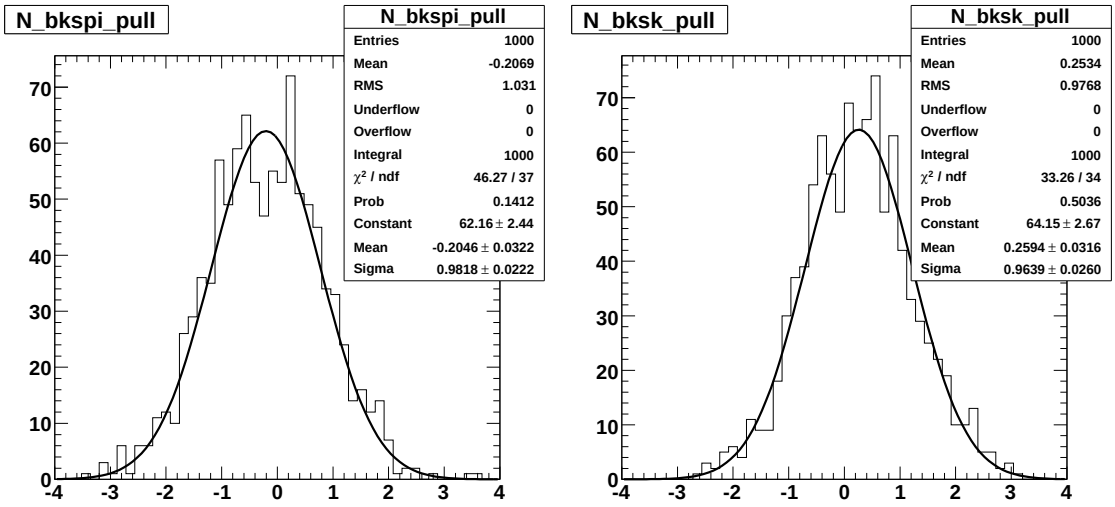

Figure 5.6: Pull plots for the $K^0_S\pi^+$ (left) and $K^0_S K^+$ (right) continuum background yields in 1000 toy experiments.

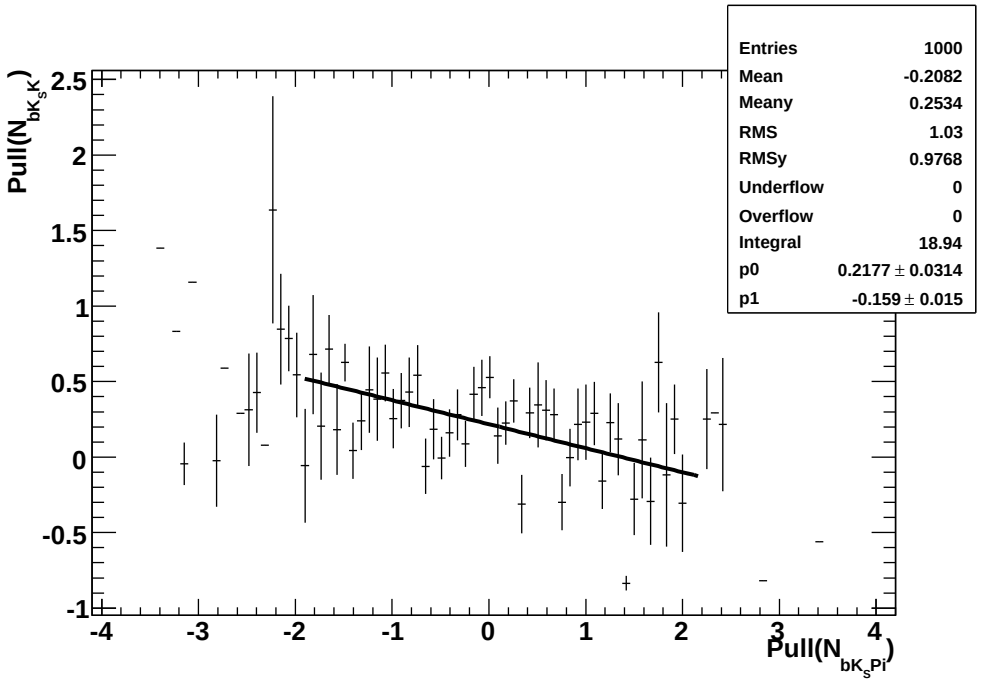

Figure 5.7: The $K^0_S K$ background-yield pull plotted versus the $K^0_S \pi$ background-yield pull in 1000 toy experiments.

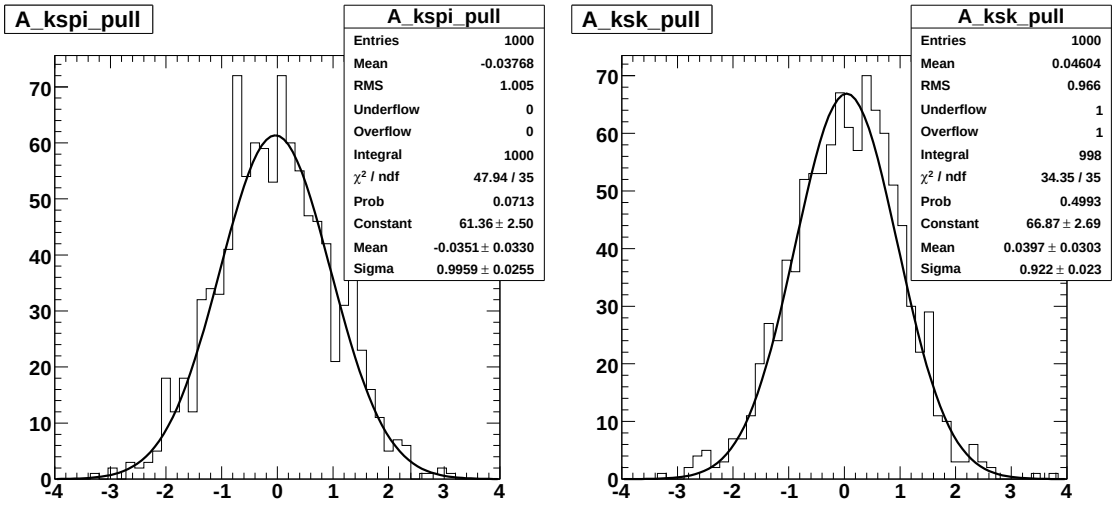

Figure 5.8: Pull plots for the $K^0_S \pi^+$ (left) and $K^0_S K^+$ (right) signal asymmetries in 1000 toy experiments.

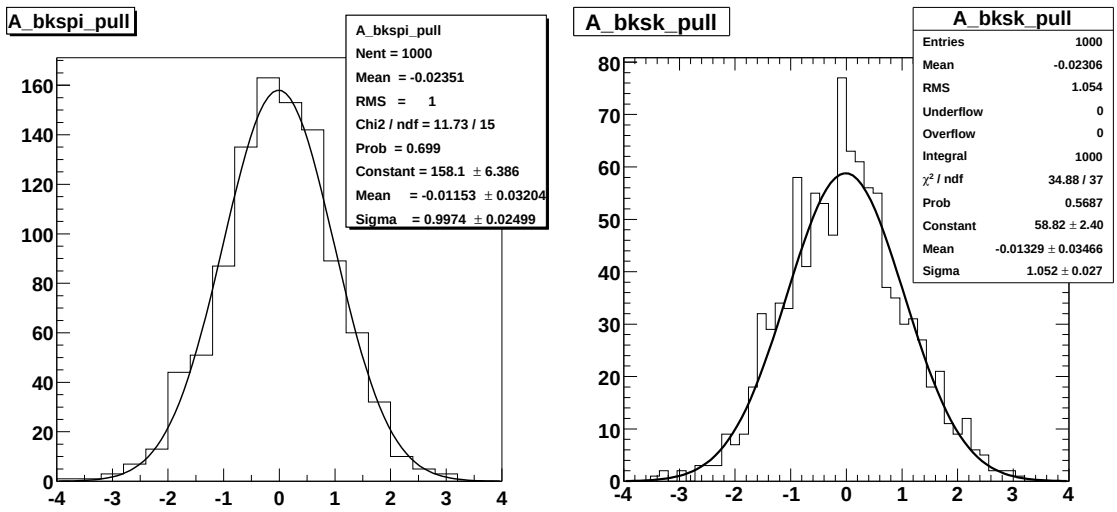

Figure 5.9: Pull plots for the $K^0_S\pi^+$ (left) and $K^0_SK^+$ (right) background asymmetries in 1000 toy experiments.

In Figs. 5.5, 5.6, 5.8, and 5.9 we show the pull plots of the fitted parameters. We observe no significant bias on any of the signal pulls and observe a bias in the background yields due to cross-feed correlation between the $K^0_S\pi$ and K^0_SK background yields, which is illustrated in Fig. 5.7. Figures 5.10 and 5.11 illustrate the pull plots of the fitted ξ parameter and the signal ΔE and $m_{\rm ES}$ means, with no evidence of bias.

In addition, we perform toy MC studies where $K^0_S\pi^+$ and $K^0_SK^+$ signal events are sampled from the simulated signal MC samples. Figure 5.12 shows the signal yield residual distributions. We observe a bias of 21.3 events on the $K^0_S\pi^+$ yield, which we include as a systematic uncertainty. No evidence of bias is observed on the $K^0_SK^+$ yield. We also fit the data sample from the 2005 analysis and find consistent results.

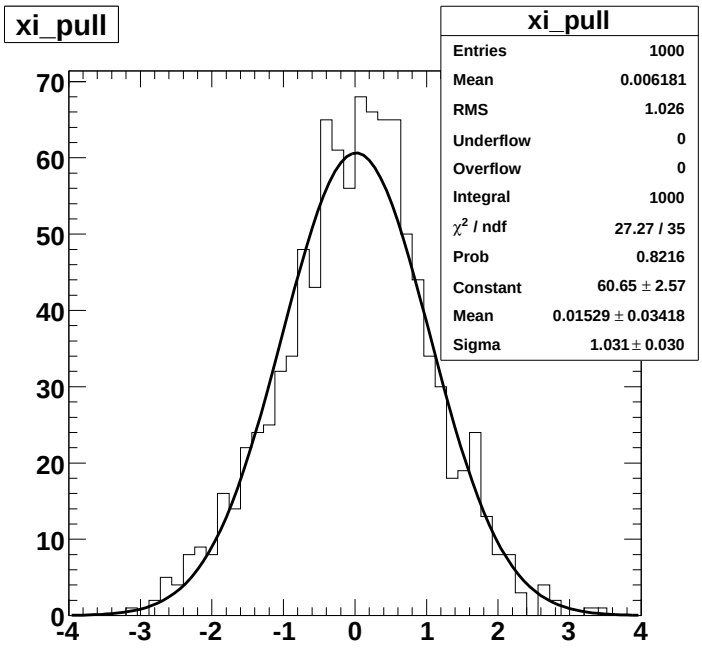

Figure 5.10: Pull plot for the background $m_{\rm ES}$ PDF parameter in 1000 toy experiments.

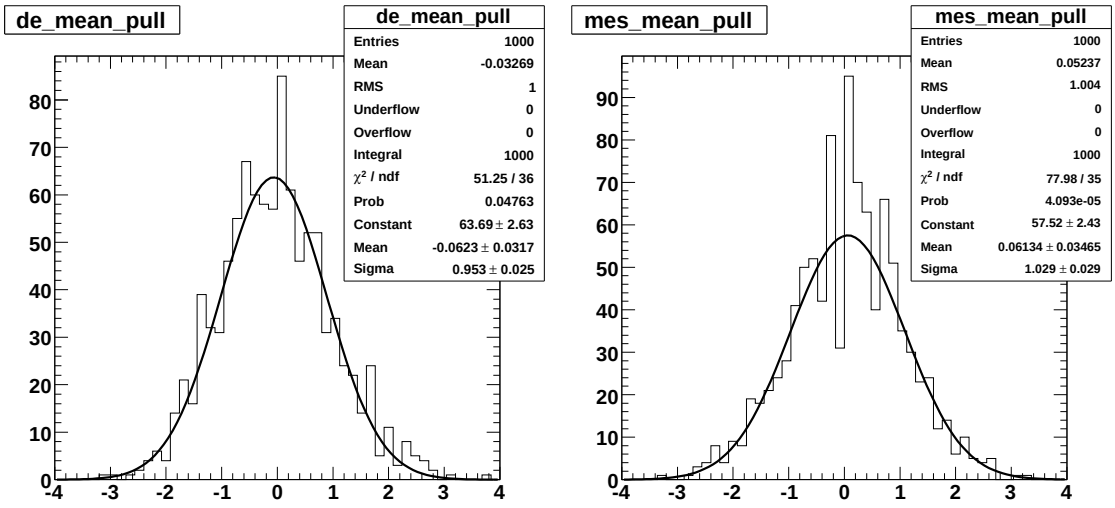

Figure 5.11: Pull plots for the signal ΔE mean and $m_{\rm ES}$ in 1000 toy experiments.

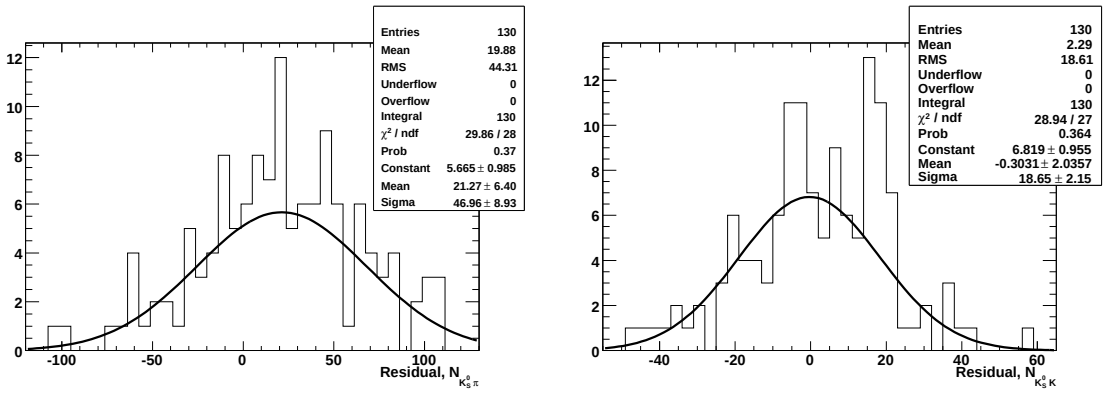

Figure 5.12: Residual plots for the $K^0_S\pi^+$ (left) and $K^0_SK^+$ (right) signal yields in toy experiments where the signal is randomly sampled from the simulated signal MC samples.

5.6 Results

The final fit was performed on the data sample of $30,159$ candidates. The fit determined the following physical parameters:

$$
\begin{aligned}
N_{K^0_S\pi} &= 1072^{+46}_{-45} \text{ events}, \\
N_{K^0_SK} &= 71^{+19}_{-18} \text{ events}, \\
\mathcal{A}_{K^0_S\pi} &= -0.029 \pm 0.039, \\
\mathcal{A}_{K^0_SK} &= 0.10^{+0.25}_{-0.26}\ , \\
N_{\mathrm{b}K^0_S\pi} &= 16,633 \pm 136 \text{ events}, \\
N_{\mathrm{b}K^0_SK} &= 12,384 \pm 117 \text{ events}, \\
\mathcal{A}_{bK^0_S\pi} &= -0.010 \pm 0.008, \\
\mathcal{A}_{bK^0_SK} &= -0.005 \pm 0.009.
\end{aligned}
$$

The statistical significance of the signal K^0_SK yield is 5.4σ.

Fig. 5.13 shows the $m_{\rm ES}$ and ΔE distributions with the fitted PDFs superimposed. Figures 5.14 and 5.15 show signal $m_{\rm ES}$ and ΔE sPlots, respectively, for the $K^0_S\pi$ and K^0_SK modes, with the results of the fit superimposed.

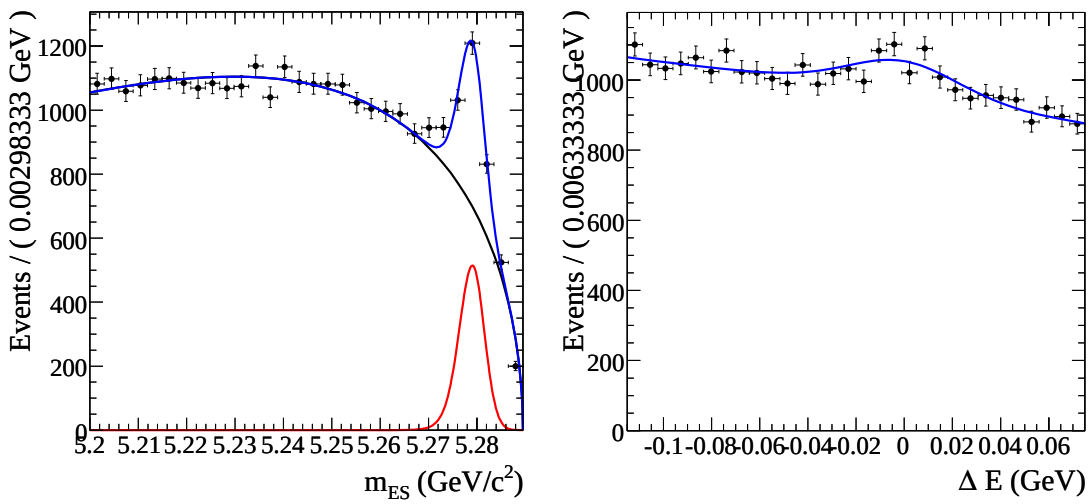

Figure 5.13: Distribution of $m_{\rm ES}$ and ΔE in the final data sample with the fitted PDFs superimposed. The $m_{\rm ES}$ plot shows the separate contributions from the signal (red) and continuum (black) components.

5.7 Systematic Uncertainties

We account for systematic effects due to PDF modeling by varying fixed parameters by their uncertainties and recording the change in the fit results. As all the background PDF parameters are floated in the fit, the systematic errors due to their uncertainties are already accounted for in the statistical errors of the fitted yields and asymmetries. Similarly, systematic effects due to the value of the signal $m_{\rm ES}$ and ΔE PDFs and all the signal Fisher parameters are included in the statistical errors. An uncertainty of $\pm 0.2\,{\rm MeV}/c^2$ is assigned to the widths of the signal $m_{\rm ES}$ PDF, as determined by typical differences between data and MC in two-body analyses. Similarly, an uncertainty of $\pm 3\,{\rm MeV}$ is assigned to the signal ΔE core width. In addition, a fit is performed setting the fraction of the tail Gaussian to zero to estimate the effect of imperfect modeling of the tails of the distribution. The parameters of the θ_C PDFs are also varied by their uncertainties. Table 5.10 summarizes the systematic uncertainties due to imperfect modeling of the PDFs.

From the signal $K^0_S\pi^+$ signal sPlot in Fig. 5.15, we notice that the core width of the PDF, which was fixed in the fit, is slightly overestimated. We repeat the fit floating

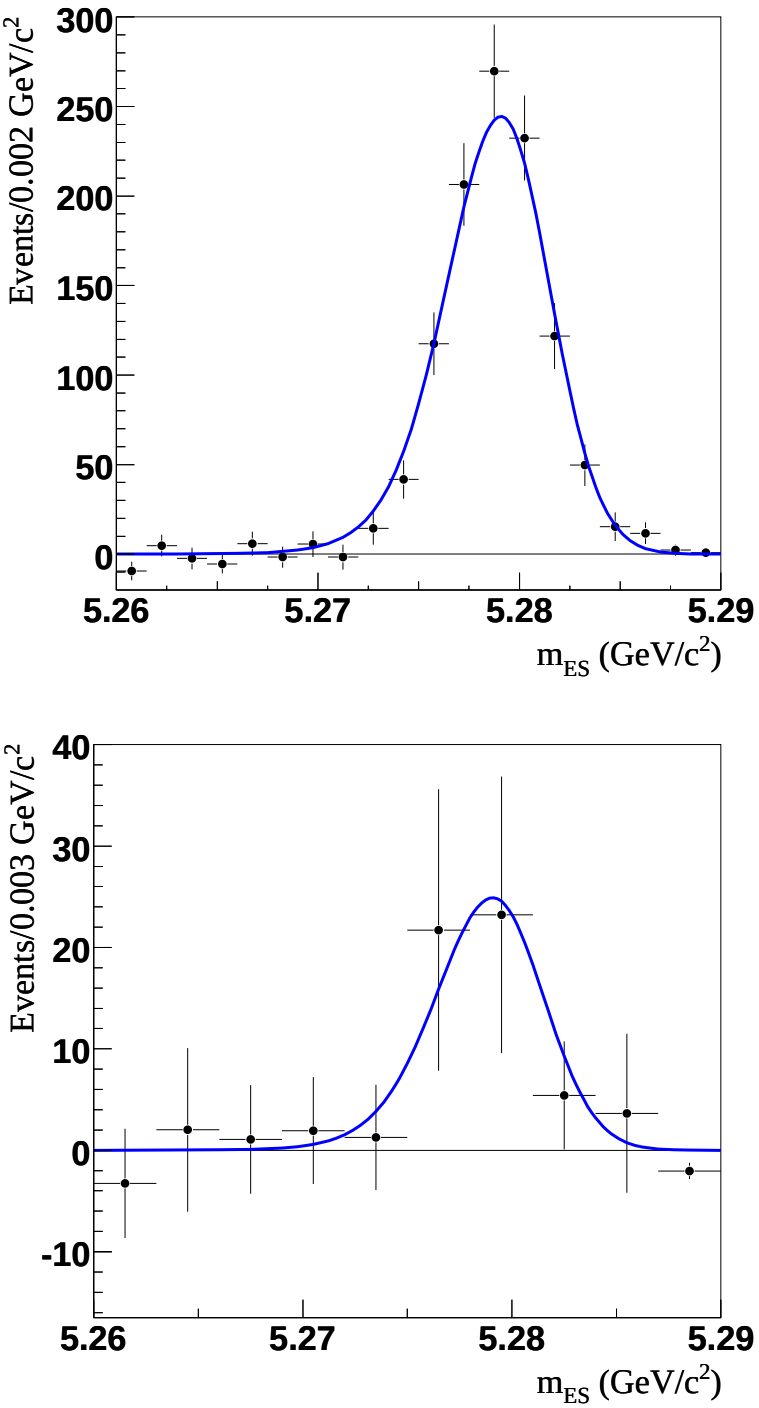

Figure 5.14: Signal $m_{\rm ES}$ sPlots for $K^0_S\pi$ (top) and $K^0_S K$ (bottom).

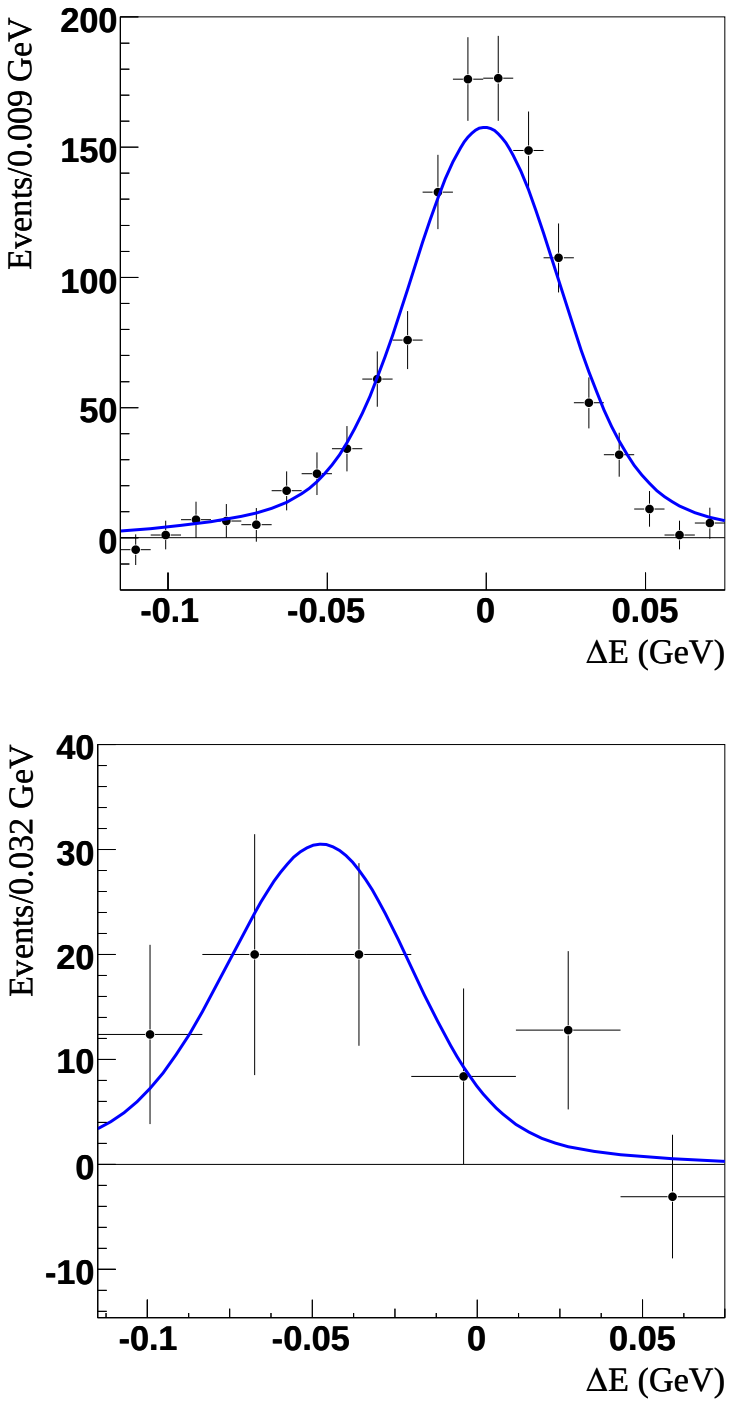

Figure 5.15: Signal ΔE sPlots for $K^0_S\pi$ (top) and $K^0_S K$ (bottom).

	$\Delta\ N_{K^0_S\pi}$	$\Delta\ N_{K^0_SK}$	$\Delta\ \mathcal{A}_{K^0_S\pi}$	$\Delta\ \mathcal{A}_{K^0_SK}$
Total	$^{+22.6}_{-29.1}$	$^{+2.8}_{-2.6}$	$^{+0.0024}_{-0.0023}$	± 0.027

Table 5.10: Total systematic contributions from PDF modeling.

$N_{K^0_S\pi}$	$N_{K^0_SK}$	$\mathcal{A}_{K^0_S\pi}$ (%)	$\mathcal{A}_{K^0_SK}$ (%)	$N_{\mathrm{b}K^0_S\pi}$	$N_{\mathrm{b}K^0_SK}$
$145,254 \pm 384$	9879 ± 110	0.45 ± 0.26	0.8 ± 1.1	139 ± 16	1.7 ± 2.0

Table 5.11: Results of a fit to a signal MC sample containing $145,703$ $K^0_S\pi$ and 9584 K^0_SK events

this parameter and find that the resulting change in the signal yields is within the systematic uncertainty for this parameter determined from the above procedure. We also redo the fit with that combination of the above parameter variations that has the greatest negative effect on the K^0_SK signal yield to determine the final $B^+ \to \overline{K}^0K^+$ signal significance, obtaining 5.3σ. We thus interpret our result as an observation of this mode.

In addition, we fit a large sample of $145,703$ $K^0_S\pi^+$ and 9584 $K^0_SK^+$ simulated signal events, where the ratio is taken from the yields in the fit to data (Table 5.11). We observe a cross-feed bias at the level of 0.3% in the $K^0_S\pi$ yield and 3.1% in the K^0_SK yield. Such cross-feed is a result of imperfect DIRC separation between kaons and pions and is accurately modeled in the MC simulation of the detector. The bias in the previous toy study where the signal events were sampled from the MC samples already includes any such effects of incorrect PID. Its value for the $K^0_S\pi^+$ signal was 21.3 events, while it was negligible for the $K^0_SK^+$ events. To be conservative, we take the bigger of the biases in the two studies for both modes and add the bias in quadrature with its error to determine the symmetric systematic uncertainty due to crossfeed and other imperfections in the fitting method. The values are 22.2 events for $K^0_S\pi^+$ and 2.3 events for $K^0_SK^+$. Additional sources of systematic errors for the branching fraction measurements are from efficiencies and the number of $B\overline{B}$ decays

$(347.5 \pm 3.8 \pm 0.1) \times 10^6$. The relative systematic errors from efficiencies are 2.7%, determined as in the $B^0 \to K^0\overline{K}^0$ analysis.

Although no physical direct CP asymmetry is present in the background, slight differences in the detector's response to positively versus negatively charged tracks could bias the asymmetry results [52]. These effects can be due to slightly different cross-sections for interactions of positive and negative kaons with detector material, as it is made out of matter, not antimatter. Also, geometric effects can produce slightly different acceptance for positively and negatively charged tracks, as they are bent in opposite directions by the magnetic field of the solenoid.

To account for these effects, we examine the fitted asymmetry values in the previously conducted validation tests. We do not observe any bias in the toy studies. The signal MC samples were generated with an asymmetry of zero, which is also the expectation for the physically underlying processes of the continuum background in the final fit to data. Looking for deviations from the zero hypothesis in these samples, we see that the largest deviation is in the asymmetry value for $K^0_S\pi^+$ background in the fit to data, at -0.010 ± 0.008. Although this result is consistent with no bias, we conservatively assign a 1% systematic uncertainty on $\mathcal{A}_{K^0_S\pi}$ and $\mathcal{A}_{K^0_S K}$ from potential charge asymmetries in the detector response. Our final asymmetry results are thus

$$\begin{aligned} \mathcal{A}_{K^0_S\pi} &= -0.029 \pm 0.039 \pm 0.010, \\ \mathcal{A}_{K^0_S K} &= 0.10^{+0.25}_{-0.26} \pm 0.03, \end{aligned}$$

where the first errors are statistical and the second are systematic.

5.8 Calculation of the Branching Fractions

To extract the $B^+ \to \overline{K}^0 K^+$ and $B^+ \to K^0\pi^+$ branching fractions, we relate them to the signal yields $N_{K^0_S h}$ determined from the fit in a way analogous to the $B^0 \to K^0\overline{K}^0$

Mode	$N_{K^0_S h}$	Significance	$\mathcal{B}\,(10^{-6})$	$\mathcal{A}_{K^0_S h}$
$K^0\pi^+$	$1072\ ^{+46\ +32}_{-45\ -37}$	$-$	$23.9^{+1.1}_{-1.0}\pm1.0$	$-0.029\pm0.039\pm0.010$
$\overline{K}^0K^+$	$71\ ^{+19\ +3.6}_{-18\ -3.5}$	5.3σ	$1.61^{+0.44}_{-0.41}\pm0.09$	$0.10^{+0.25}_{-0.26}\pm0.03$

Table 5.12: Summary of results for $B^+\to\overline{K}^0K^+$ and $B^+\to K^0\pi^+$. Shown are the fitted signal yields $N_{K^0_S h}$, signal-yield significances (including systematic uncertainties), measured branching fractions $\mathcal{B}$, and the direct CP asymmetries $\mathcal{A}_{K^0_S h}$. The first errors are statistical and the second are systematic.

analysis:

$$\mathcal{B}(B\to K^0h)=\frac{1}{\mathcal{B}(K^0\to K^0_S)\cdot\mathcal{B}(K^0_S\to\pi^+\pi^-)}\frac{N_{\mathrm{K^0_S h}}}{\epsilon\cdot N_{B\overline{B}}}, \tag{5.7}$$

where $N_{B\overline{B}}$ is the number of $B\overline{B}$ pairs in the *BABAR* dataset and ϵ is the nominal $B\to K^0h$ efficiency. The $\pi^+\pi^-$ decay branching fraction is 0.6895 (PDG value [20]), and $\mathcal{B}(K^0K^0_S)=0.5$. These two branching fractions are already included in the total efficiencies. The final results are

$$\begin{aligned}\mathcal{B}(B^+\to K^0\pi^+) &= (23.9^{+1.1}_{-1.0}\pm1.0)\times10^{-6},\\ \mathcal{B}(B^+\to\overline{K}^0K^+) &= (1.61^{+0.44}_{-0.41}\pm0.09)\times10^{-6}.\end{aligned}$$

5.9 Summary of $B^+\to\overline{K}^0K^+$ and $B^+\to K^0\pi^+$

Our final results are summarized in Table 5.12. We have observed the $B^+\to\overline{K}^0K^+$ decay at greater than 5σ significance. This constitutes another clear observation of a mode dominated by the gluonic $b\to d$ penguin transition, complementing the observation of $B^0\to K^0\overline{K}^0$. The branching fraction is at the level predicted by theory and is slightly larger than for the neutral mode, although more data is needed for the comparison. A larger value would indicate a sizeable contribution from the annihilation amplitude to the $b\to d$ penguin [32]. We do not observe any evidence for a sizeable direct CP asymmetry, but the uncertainties are still large.

The CP asymmetry in $B^+\to K^0\pi^+$ is consistent with zero at 4% absolute preci-

sion, which is expected from theoretical comparisons with other $B \to K\pi$ decays. The branching fraction is consistent with theoretical predictions at 6% relative precision, indicating no deviations from Standard Model expectations.

These results have been published in the journal Physical Review Letters [50]. The Belle collaboration reported a similar observation of $B^+ \to \overline{K}^0 K^+$ and obtained results on $B^+ \to K^0\pi^+$ that are consistent with this measurement [51].

Chapter 6

Conclusions

This dissertation presents the first observation at *BABAR* of $B \to K\overline{K}$ decays dominated by the $b \to d$ transition proceeding through a virtual loop with a gluon. The results along with the analogous measurements from Belle are summarized in Table 6.1. The measurements of the two experiments are consistent, introducing this class of flavor-changing neutral current processes as yet another avenue for testing the Standard Model and searching for CP-violating effects of new physical contributions.

The time-dependent CP measurement is the first step in this direction and establishes the feasibility of the beam-constrained vertexing method in these rare decays. The 3σ exclusions in the physically allowed region of the S-C plane are the first constraint of CP violation in the interference between mixing and decay in any process dominated by the $b \to d$ transition (gluonic or radiative). The uncertainties are still large, but the values can already be used as inputs in theoretical methods relating the CP asymmetries to the measured branching fraction [29].

The observation of $B \to K\overline{K}$ decays at the B factories is a significant milestone in the search for two-body B decays without charm quarks in the final state. Figure 6.1 shows the current status of branching-fraction measurements in two-body decays with only kaons and pions in the final state, illustrating clearly the descending hierarchy from $B \to K\pi$, through $B \to \pi\pi$, to $B \to K\overline{K}$ processes. The $B^+ \to K^0\pi^+$

	BABAR	Belle
$\mathcal{B}(B^0 \to K^0\overline{K}^0)$	$(1.08 \pm 0.28 \pm 0.11) \times 10^{-6}$	$(0.87^{+0.25}_{-0.20} \pm 0.09) \times 10^{-6}$
$\mathcal{B}(B^+ \to \overline{K}^0 K^+)$	$(1.61 \pm 0.44 \pm 0.09) \times 10^{-6}$	$(1.22^{+0.32+0.13}_{-0.28-0.16}) \times 10^{-6}$
$\mathcal{B}(B^+ \to K^0\pi^+)$	$(23.9 \pm 1.1 \pm 1.0) \times 10^{-6}$	$(22.8^{+0.8}_{-0.7} \pm 1.3) \times 10^{-6}$
$S(K^0_S K^0_S)$	$-1.28^{+0.80+0.11}_{-0.73-0.16}$	–
$C(K^0_S K^0_S)$	$-0.40 \pm 0.41 \pm 0.06$	$0.58^{+0.73}_{-0.66} \pm 0.04$
$\mathcal{A}(K^0_S K^+)$	$0.10 \pm 0.26 \pm 0.03$	$0.13^{+0.23}_{-0.24} \pm 0.02$
$\mathcal{A}(K^0_S \pi^+)$	$-0.029 \pm 0.039 \pm 0.010$	$0.03 \pm 0.03 \pm 0.01$

Table 6.1: Summary of results from *BABAR* [50] and Belle [51]. Belle reported $\mathcal{A}(K^0_S K^0_S) = -C(K^0_S K^0_S)$. The first errors are statistical and the second are systematic.

decay analyzed in this dissertation has the largest branching fraction in this group of modes, while $B^0 \to K^0\overline{K}^0$ has the smallest. The one mode that is still unobserved is $B^0 \to K^+K^-$, which proceeds through the highly suppressed W-exchange diagram in the SM and is not expected to be seen at the B factories if no NP effects are present. (The branching fraction is predicted to be in the 10^{-8}-10^{-7} range [49].) Overall, the branching fractions of these modes are at levels expected from Standard Model predictions.

No direct CP asymmetries are observed in either charged B decay mode. This is expected in the $B^+ \to K^0\pi^+$ mode, as it is dominated by the single $b \to s$ penguin amplitude that is much larger than the annihilation amplitude. On the other hand, the annihilation contribution could be comparable in magnitude to the $b \to d$ penguin amplitude in $B^+ \to \overline{K}^0 K^+$, possibly causing a large direct CP asymmetry in their interference [32]. The present results do not exclude a direct CP asymmetry at the 20-30% level. There is also a hint of deviation between the branching fraction of $B^0 \to K^0\overline{K}^0$ and $B^+ \to \overline{K}^0 K^+$, indicating the potential significance of the annihilation contribution, although more data is needed to constrain its effect.

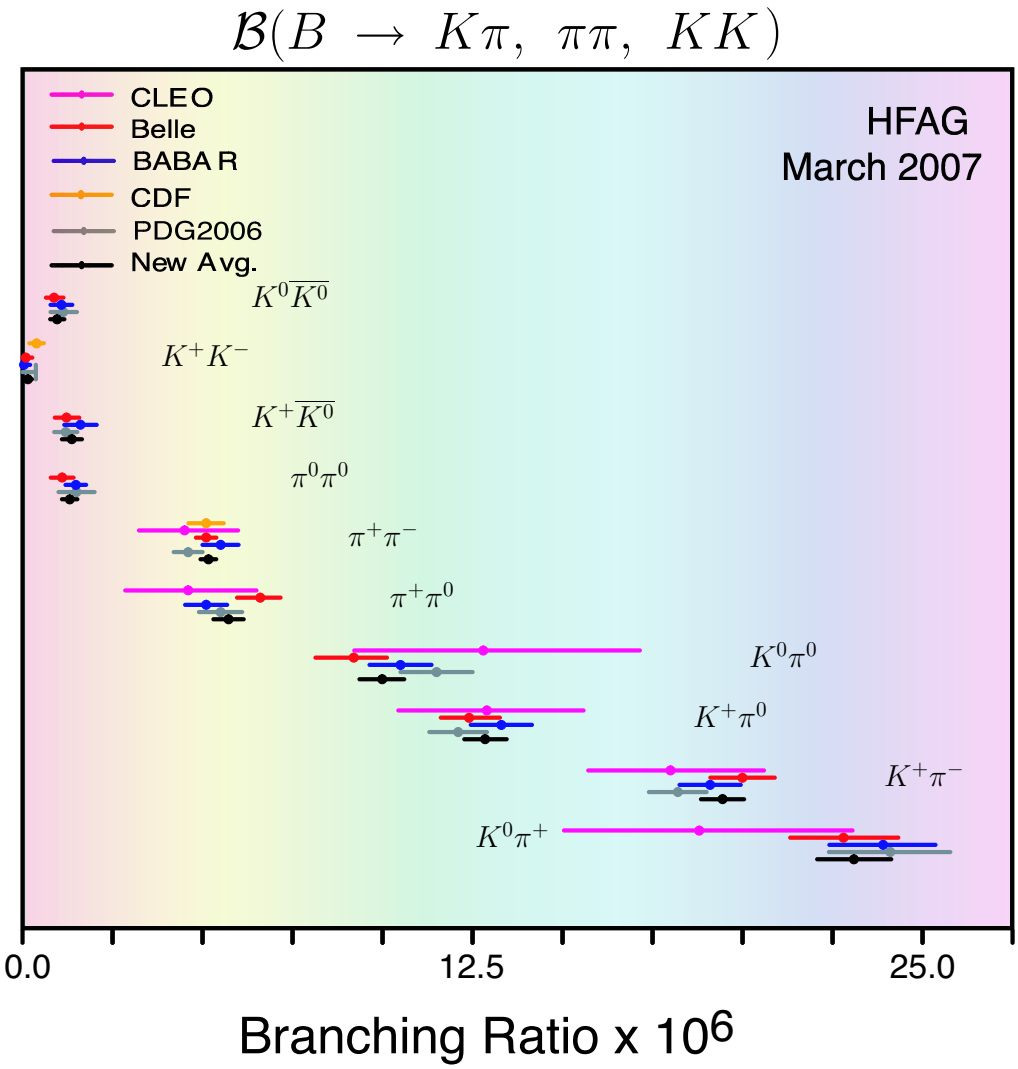

Figure 6.1: Branching-fraction measurements for two-body charmless B decays [21].

Future Outlook

The current measurement at *BABAR* was made with about 350 million $B\overline{B}$ pairs. The final dataset through 2008 is expected to be 2.5 times larger. Scaling the present errors, this corresponds to a 15% measurement of the two $B \to K\overline{K}$ branching fractions and errors of ~ 0.4 on S and ~ 0.25 on C. Belle should have similar performance. These rare modes will be statistically limited for the remainder of B factory operations, while the branching fraction for $B^+ \to K^0\pi^+$ will be limited by systematic uncertainties. However, larger datasets will allow floating more PDF parameters in the fit, decreasing the systematic error from PDF modeling, while further study of the selection criteria will decrease the efficiency uncertainties. With these improvements, a 2% measurement of $\mathcal{B}(B^+ \to K^0\pi^+)$ should be possible.

If the C value in $B^0 \to K^0\overline{K}^0$ remains negative, the measurement would exclude $C \geq 0$, which would disfavor the approach of Ref. [31]. Similarly, if the magnitude of S remains large, the result would indicate either the presence of NP contributions or the incorrect modeling of strong-interaction effects in the QCD Factorization and Perturbative QCD treatments of Refs. [27] and [29]. As QCD effects at low energies are difficult to estimate, this would serve as an important quide to these approximate approaches. Similarly, a measurement of $\mathcal{A}(K^0_S K^+)$ with 15% precision will constrain the direct CP effects due to the annihilation contribution. Comparisons of the two branching fractions at the 15% level will provide an additional estimate of the magnitude of this amplitude.

Investigation of these modes at a potential future Super-B factory with $100\,\mathrm{ab}^{-1}$ of e^+e^- collision data would extend this exciting $b \to d$ program into the realm of precision measurements. Searching for new physical effects in precision low-energy measurements of virtual-loop processes would be complementary to the direct high-energy searches at the Large Hadron Collider.

Bibliography

[1] C. S. Wu *et al.*, Phys. Rev. **105**, 1413 (1957).

[2] J. H. Christenson, J. W. Cronin, V. L. Fitch, and R. Turlay, Phys. Rev. Lett. **105**, 1415 (1957).

[3] A. Sakharov, JETP **5**, 24 (1967).

[4] *BABAR* Collaboration, B. Aubert *et al.*, Phys. Rev. Lett. **87**, 091801 (2001); Belle Collaboration, K. Abe *et al.*, Phys. Rev. Lett. **87**, 091802 (2001).

[5] Belle Collaboration, K. Abe *et al.*, Phys. Rev. Lett. **91**, 261602 (2003); *BABAR* Collaboration, B. Aubert *et al.*, Phys. Rev. D **71**, 091102 (2005).

[6] Belle Collaboration, K. Abe *et al.*, Phys. Rev. Lett. **96**, 221601 (2006); *BABAR* Collaboration, B. Aubert *et al.*, arXiv:hep-ex/0612017.

[7] *BABAR* Collaboration, B. Aubert *et al.*, Phys. Rev. Lett. **95**, 221801 (2005).

[8] Belle Collaboration, K. Abe *et al.*, Phys. Rev. Lett. **95**, 231802 (2005).

[9] S. Weinberg, Phys. Rev. Lett. **19**, 1264 (1967); A. Salam, in: Elementary Particle Physics, ed. N. Svartholm (Almquist and Wiksell, Stockholm, 1968), p. 367; S.L. Glashow, J. Iliopoulos, and L. Maiani, Phys. Rev. D **2**, 1285 (1970).

[10] P. W. Higgs, Phys. Lett. **12**, 132 (1964); Phys. Rev. Lett. **23**, 508 (1964); Phys. Rev. **245**, 1156 (1966).

[11] T. S. Virdee, Phys. Rep. **403-404**, 401 (2004).

[12] N. Cabibbo, Phys. Rev. Lett. **10**, 531 (1963); M. Kobayashi and T. Maskawa, Prog. Theor. Phys. **49**, 652 (1973).

[13] WMAP Collaboration, D. N. Spergel *et al.*, Astro. Phys. J. Suppl. **148**, 175 (2003).

[14] J. Kuckei *et al.*, Phys. Atom. Nuclei **70**, 349 (2007).

[15] H. Banerjee, D. Chatterjee, and P. Mitra, Phys. Lett. B **573**, 109 (2003).

[16] L. Wolfenstein, Phys. Rev. Lett. **51**, 1945 (1983).

[17] M. Bander, D. Silverman, and A. Soni, Phys. Rev. Lett. **43**, 242 (1979); A. Carter and A. I. Sanda, Phys. Rev. Lett. **45**, 952 (1980); I. I. Bigi and A. I. Sanda, Nucl. Phys. B **193**, 85 (1981); I. I. Bigi and A. I. Sanda, Nucl. Phys. B **281**, 41 (1987).

[18] NA48 Collaboration, V. Fanti *et al.*, Phys. Lett. B **465**, 335 (1999); KTeV Collaboration, A. Alavi-Harati *et al.*, Phys. Rev. Lett. **83**, 22 (1999).

[19] *BABAR* Collaboration, B. Aubert *et al.*, Phys. Rev. Lett. **93**, 131801 (2004); *BABAR* Collaboration, B. Aubert *et al.*, arXiv:hep-ex/0703016; Belle Collaboration, Y. Chao *et al.*, Phys. Rev. Lett. **93**, 191802 (2004); Belle Collaboration, K. Ishino *et al.*, arXiv:hep-ex/0608035.

[20] Particle Data Group, S. Eidelman *et al.*, Phys. Lett. B **592**, 1 (2004).

[21] Heavy Flavor Averaging Group, E. Barberio *et al.*, arXiv:hep-ex/0603003 (2006), http://www.slac.stanford.edu/xorg/hfag/ .

[22] *BABAR* Collaboration, B. Aubert *et al.*, arXiv:hep-ex/0703021; Belle Collaboration, K. F. Chen *et al.*, Phys. Rev. Lett. **98**, 031802 (2007).

[23] CKMFitter Collaboration, J. Charles *et al.*, Eur. Phys. Jour. C **41**, 1-131 (2005), http://ckmfitter.in2p3.fr .

[24] D. London and R. D. Peccei, Phys. Lett. B **223**, 257 (1989); H. R. Quinn, Nucl. Phys. B Proc. Suppl. **37A**, 21 (1994).

[25] M. Ciuchini and L. Silvestrini, Phys. Rev. Lett. **97**, 021803 (2006); M. Ciuchini *et al.*, PoS **HEP2005**, 221 (2006) [arXiv:hep-ph/0512141].

[26] R. Fleischer, Phys. Lett. B **341**, 205 (1994).

[27] R. Fleischer and S. Recksiegel, Eur. Phys. Jour. C **38**, 251 (2004).

[28] A. K. Giri and R. Mohanta, JHEP **11**, 084 (2004).

[29] A. Datta *et al.*, arXiv:hep-ph/0611280.

[30] A. Soni and D. A. Suprun, Phys. Rev. D **75** 054006 (2007).

[31] S. Descotes-Genon, J. Matias, and J. Virto, Phys. Rev. Lett. **97**, 061801 (2006).

[32] X. Q. Hao, X. G. He and X. Q. Li, Phys. Rev. D **75**, 037501 (2007).

[33] PEP-II Conceptual Design Report, SLAC-R-418 (1993).

[34] *BABAR* Collaboration, B. Aubert *et al.*, Nucl. Instrum. Methods Phys. Res., Sect. A**479**, 1 (2002).

[35] Belle Collaboration, A. Abashian *et al.*, Nucl. Instrum. Methods Phys. Res., Sect. A**479**, 117 (2002).

[36] *BABAR* Collaboration, B. Aubert *et al.*, Phys. Rev. D **69**, 071101 (2004); Belle Collaboration, N. C. Hastings *et al.*, Phys. Rev. D **67**, 052004 (2003).

[37] EvtGen, http://hep.ucsb.edu/people/lange/EvtGen .

[38] JetSet, http://www.thep.lu.se/torbjorn/Pythia.html .

[39] GEANT 4, S. Agostini *et al.*, Nucl. Instrum. Methods Phys. Res., Sect. A**506**, 250 (2003).

[40] For a review, see D. Kirkby and Y. Nir in Ref. [20].

[41] G. Hanson *et al.*, Phys. Rev. Lett. **35**, 1609 (1975).

[42] G. C. Fox and S. Wolfram, Nucl. Phys. B **149**, 413 (1979).

[43] R. A. Fisher, Annals of Eugenics **7** (1936).

[44] *BABAR* Collaboration, B. Aubert *et al.*, Phys. Rev. Lett. **89**, 281802 (2002).

[45] *BABAR* Collaboration, B. Aubert *et al.*, Phys. Rev. Lett. **93**, 131805 (2004); Phys. Rev. D **71**, 111102 (2005).

[46] *BABAR* Collaboration, B. Aubert *et al.*, Phys. Rev. D **66**, 032003 (2002); Phys. Rev. Lett. **94**, 161803 (2005).

[47] M. Pivk and F. R. Le Diberder, Nucl. Instrum. Methods Phys. Res., Sect. A **555**, 356 (2005).

[48] O. Long *et al.*, Phys. Rev. D **68**, 03010 (2003).

[49] M. Beneke and M. Neubert, Nucl. Phys. B **675**, 333 (2003); Y.-Y. Keum, Pramana **63**, 1151 (2004); R. Fleischer and S. Recksiegel, Phys. Rev. D **71**, 051501 (2005).

[50] *BABAR* Collaboration, B. Aubert *et al.*, Phys. Rev. Lett. **97**, 171805 (2006).

[51] Belle Collaboration, S.-W. Lin *et al.*, Phys. Rev. Lett. **98**, 181804 (2007).

[52] *BABAR* Collaboration, B. Aubert *et al.*, Phys. Rev. Lett. **93**, 131801 (2004).